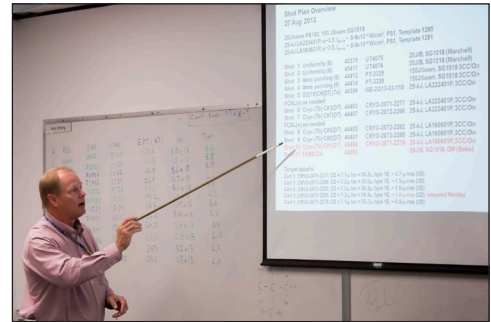# LLE Review

Quarterly Report

UR
LLE

About the Cover:

The cover photo presents C. Sangster, T. Kosc, V. Versteeg, and V. Goncharov who led the cryogenic target implosion experiments on LLE's 60-beam OMEGA Laser System. Over 270 layered fuel capsules [using pure deuterium (D_2) and deuterium–tritium (DT)] are imploded to demonstrate hydrodynamic performance equivalent to direct-drive target design and laser energy available at the National Ignition Facility (NIF). This demonstration is an important scientific prerequisite for the polar-drive–ignition campaign on the NIF. In the background is the Moving Cryostat Transfer Cart (MCTC) during the preparation for the shot.

The photo on the right shows OMEGA Experiments Group Leader C. Sangster during the morning pre-watch briefing, describing details of the cryogenic shots scheduled on that day. The photo below highlights six MCTC's, including one at the lower pylon (second from the right). M. Maslyn and D. Whitaker are working on the cryogenic capsule inception into the OMEGA target chamber.

LLE Review

Quarterly Report

UR ⬙
LLE

Contents

In Brief

This volume of the LLE Review, covering April–June 2013, features "Improving Cryogenic DT Implosion Performance on OMEGA" by T. C. Sangster, V. N. Goncharov, P. B. Radha, T. R. Boehly, T. J. B. Collins, R. S. Craxton, J. A. Delettrez, D. H. Edgell, R. Epstein, C. J. Forrest, D. H. Froula, Y. Yu. Glebov, D. R. Harding, M. Hohenberger, S. X. Hu, I. V. Igumenshchev, R. Janezic, J. H. Kelly, T. J. Kessler, C. Kingsley, T. Z. Kosc, J. P. Knauer, S. J. Loucks, J. A. Marozas, F. J. Marshall, A. V. Maximov, P. W. McKenty, D. T. Michel, J. F. Myatt, S. P. Regan, W. Seka, W. T. Shmayda, R. W. Short, A. Shvydky, S. Skupsky, J. M. Soures, C. Stoeckl, W. Theobald, V. Versteeg, B. Yaakobi, and J. D. Zuegel (LLE); R. Betti, R. L. McCrory, and D. D. Meyerhofer (LLE, Department of Physics and Astronomy, and Department of Mechanical Engineering); and D. T. Casey, J. A. Frenje, M. Gatu-Johnson, and R. D. Petrasso (MIT). In this article (p. 145), the results from a series of cryogenic DT implosions are presented. A flexible direct-drive target platform was used to implode cryogenic deuterium–tritium (DT) capsules on the OMEGA Laser System. The goal of these experiments was to demonstrate ignition hydrodynamically equivalent performance where the laser drive intensity, the implosion velocity, the fuel adiabat, and the in-flight aspect ratio (IFAR) were the same as those for a 1.5-MJ target designed to ignite on the National Ignition Facility. The implosions spanned a broad region of design space to study target performance as a function of shell stability (adiabat) and implosion velocity. Ablation-front perturbation growth appears to limit target performance at high implosion velocities. A trend in the value of the Lawson criterion for each of the implosions in adiabat–IFAR space suggests the existence of a stability boundary that leads to ablator mixing into the hot spot for the most-ignition-equivalent designs.

Additional highlights of research presented in this issue include the following:

- F. J. Marshall, P. B. Radha, M. J. Bonino, J. A. Delettrez, D. R. Harding, and R. Epstein (LLE), and E. Giraldez (General Atomics) report the results of polar-driven direct-drive experiments recently performed on the OMEGA Laser System (p. 156). These experiments have demonstrated the efficacy of using a shimmed target (one with a contoured shell thickness) to improve implosion symmetry.

- W. Seka, J. F. Myatt, R. W. Short, D. H. Froula, and J. Katz have demonstrated that $\omega/2$ spectra and images provide a powerful direct-drive, coronal plasma diagnostic for inertial confinement fusion (p. 161). Spatially and temporally resolved half-harmonic spectra and images of laser-driven implosions show evidence of local, multibeam-driven two-plasmon–decay (TPD) instability. This instability always starts with the multibeam absolute instability that rapidly evolves into the convective regime extending between $n_c/4 \leq n_e \leq n_e/5$. The lower density is determined by Landau damping. Judging from the $\omega/2$ spectra, this instability is never observed in its linear stage, consistent with expectations. When the target view included the target normal and the TPD threshold was exceeded, a sharp, red-shifted $\omega/2$ spectral feature was observed that can serve as a convenient local electron temperature diagnostic. Time-resolved electron temperatures revealed locally increased electron temperatures in areas of enhanced overlapped irradiation intensities. Corroborating information was obtained from spatial images taken in the blue portion of the $\omega/2$ spectrum.

- B. Yaakobi, A. A. Solodov, J. F. Myatt, J. A. Delettrez, C. Stoeckl, and D. H. Froula report the results of measuring the divergence of fast electrons in laser-irradiated spherical targets (p. 167). In recent experiments using directly driven spherical targets on the OMEGA Laser System, the energy in fast electrons was found to reach ~1% of the laser energy at an irradiance of ~1.1×10^{15} W/cm^2. The fraction of the fast electrons absorbed in the compressed fuel shell depends on their angular divergence. This divergence is deduced from a series of shots where Mo-coated shells of increasing diameter D were embedded within an outer CH shell. The intensity of the Mo-K$_\alpha$ line and the hard x-ray radiation were found to increase approximately as ~D^2, indicating wide divergence of the fast electrons. Alternative interpretations of these results (electron scattering, radiation excitation of K$_\alpha$, and an electric field caused by the return current) are shown to be unimportant.

- J. R. Davies, R. Betti, P. M. Nilson, and A. A. Solodov (Fusion Science Center and LLE) review the published measurements and models of the cross section for electrons causing K$_\alpha$ emission from copper to find a suitable expression for analyzing K$_\alpha$ emission measurements in laser–solid experiments at peak intensities above 10^{18} W/cm^2 (p. 173). There exist few measurements in the electron energy range currently of interest, 0.1 to 10 MeV, leaving a number of models that could be suitable. These models are summarized with a number of typing errors corrected. Two different limiting forms for the cross section at relativistic energies are used and existing measurements do not give a clear indication as to which is correct. Comparison with the limiting form of electron stopping power indicates an alternative relativistic form and indicates that the density effect correction will be important in copper above 10 MeV. For data analysis relying on relative K$_\alpha$ emission caused by electrons with energy much greater than the K-shell binding energy, the existing uncertainty in cross sections is unimportant, but it will be a source of uncertainty when using absolute values and for electron energies up to about 6× the binding energy. K$_\alpha$ emission caused by photons and protons is also briefly reviewed.

- H. P. Howard, K. Mehrotra, J. C. Lambropoulos, and S. D. Jacobs (LLE) investigate the fracture mechanics of delamination defects in multilayer dielectric coatings (p. 187). During the fabrication of multilayer-dielectric (MLD) thin-film coated optics, such as the diffraction gratings used in OMEGA EP's pulse compressors, acid piranha cleaning can lead to the formation of chemically induced delamination defects. The causes of these defects are investigated and a mechanism for the deformation and failure of the MLD coating in response to hydrogen peroxide in the cleaning solution is described. A fracture mechanics model was developed and used to calculate the crack path that maximizes the energy release rate, which was found to be consistent with the characteristic fracture pattern observed in MLD coating delamination defects.

Alexei Kozlov
Editor

iv

Improving Cryogenic DT Implosion Performance on OMEGA

Introduction

Layered cryogenic deuterium–tritium (DT) capsules are being imploded on LLE's 60-beam OMEGA Laser System[1] to demonstrate hydrodynamic performance equivalent to that of a symmetric direct-drive target designed to ignite with the laser energy available at the National Ignition Facility (NIF).[2] Hydrodynamic equivalence implies that the shell velocity at the end of acceleration (typically referred to as the implosion velocity or V_{imp}), the in-flight aspect ratio (IFAR, defined as the ratio of the shell radius and the shell thickness evaluated after the shell has imploded to 2/3 of its initial radius), and the peak laser drive intensity (I_L) are the same as those of a symmetric ignition design[3] for the NIF. The demonstration of direct-drive hydrodynamic equivalence is viewed as an important scientific prerequisite for a polar-drive (PD)–ignition campaign on the NIF later in this decade.[4]

The polar-drive concept[5] was developed in 2004 to provide a platform for directly driven implosions on the NIF while the facility is configured for x-ray drive. A preliminary assessment of PD hot-spot target designs has shown that direct-drive ignition might be achieved on the NIF with a laser energy as low as 1 MJ_{UV} (Ref. 6). The experimental plan to support the PD-ignition campaign is based on the validation of symmetric direct-drive performance modeling (laser coupling,[7–10] shock timing[11] and thermal transport,[12,13] hot-electron generation,[14] and adiabat control[15]) using cryogenic layered DT implosions on OMEGA. Additionally, select 40-beam, ambient gas-filled PD implosions are being used to confirm drive symmetry modeling.[16] Therefore, PD-ignition designs for the NIF will be based on physics models embedded in the radiation–hydrodynamic design codes that have been validated against symmetric direct-drive–implosion data.

The cryogenic implosion database at the Omega Laser Facility includes over 270 layered fuel implosions [roughly half using pure deuterium (D_2) fuel and half using DT]. The first cryogenic D_2 capsule implosions[17] were performed in 2000 and cryogenic DT implosions[18] began in late 2006. Among the highlights of these experiments was the demonstration of areal densities in D_2 fuel in excess of 200 mg/cm^2 (Refs. 12 and 19), the demonstration of areal densities in DT fuel of 300 mg/cm^2 (Refs. 3 and 20) (nominally the minimum areal density needed to sustain a thermonuclear burn wave), and the demonstration of yields relative to 1-D predictions in excess of 15% (Ref. 21).

This article describes recent progress toward demonstrating ignition hydrodynamically equivalent implosion performance on OMEGA. The following sections (1) discuss the concept of hydrodynamic similarity and the requirements for OMEGA target design; (2) present and discuss the data from a series of cryogenic DT implosions spanning a design space that includes ignition, concluding that target performance on OMEGA is impacted by capsule surface perturbations leading to ablator mixing into the hot spot; (3) discuss the origin and hydrodynamic modeling of these capsule surface perturbations; and (4) plot all of the cryogenic DT data using the experimental ignition threshold factor (ITFx) formalism described in Ref. 22 scaled appropriately for the target mass and laser-energy differences between OMEGA and the NIF. The ITFx formalism is a convenient metric for comparing relative target performance across a broad design space and is related to the generalized Lawson criterion applied to inertial confinement fusion (ICF) derived by Betti *et al.*[23] Final concluding remarks are given in the last section.

Hydrodynamic Similarity and Experimental Design

Hydrodynamic similarity can be used to extrapolate implosion performance from the 26-kJ_{UV} OMEGA to the 1.8-MJ_{UV} NIF laser. In this way, implosions can be performed on OMEGA to probe the design space for targets on the NIF. In Ref. 24, Betti *et al.* showed explicitly that an ignition design for the NIF based on a specific adiabat (α, defined as the ratio of the shell pressure to the Fermi-degenerate pressure), implosion velocity, and laser intensity can be reproduced on OMEGA with the same adiabat, implosion velocity, and laser intensity. While this scaling should lead to the same peak stagnation pressure and density in the OMEGA and NIF cores, the resulting yields and fuel areal density will necessarily be lower on OMEGA because of the smaller fuel mass and laser energy. Indeed, for

hydrodynamic similarity, the target mass must scale as the laser energy E_L, the target radius as $E_L^{1/3}$, the laser power as $E_L^{2/3}$, and the laser pulse length as $E_L^{1/3}$.

The assumption implicit in the hydro scaling argument is that the ablation pressure and preheat sources are independent of target scale (and facility). This is unlikely to be the case, however, since the coronal plasma scale length on the NIF relative to OMEGA will scale as the radius of the capsule (approximately 4× longer) for hydrodynamically similar implosions. The longer plasma scale lengths will reduce the ablation pressure via light-scattering losses and increased cross-beam energy transfer (CBET)[8] and increase the production of hot electrons (and potentially fuel preheating) from the two-plasmon–decay (TPD) instability.[14,25] Although these laser–plasma instabilities do not *a priori* restrict the design space available on OMEGA for ignition-relevant implosions, they may limit the penultimate performance that can be achieved.

The cryogenic target design for the experiments discussed here is shown in Fig. 135.1. This design is scaled from the 1.5-MJ symmetric direct-drive–ignition design published by Goncharov *et al.* in 2010 (Ref. 3). The capsule ablator material [Fig. 135.1(a)] is pure CD (deuterated plastic) or CD doped with a few atom percent of silicon (the dopant tailors the adiabat at the ablation surface to reduce the imprint growth rate[7]). The peak intensity of the triple-picket drive pulse [Fig. 135.1(b)] is 9×10^{14} W/cm^2; the total drive energy is designed to be 26 kJ. The capsule radius is nominally 430 μm, which is (1.5 MJ/0.026 MJ)$^{1/3}$ ∼ 3.9× smaller than the 1.5-MJ ignition design (1700 μm).

Based on the hydrodynamic similarity argument above, this target platform can be used to access a broad region of design space that includes the 1.5-MJ ignition design. With constant drive intensity and laser energy, the V_{imp} and IFAR are varied by changing the thickness of the ablator and DT ice layer and adjusting the picket energies and temporal spacing to achieve the desired adiabat at the inner fuel surface (the picket adjustments are used to ensure the correct shock timing and radial convergence). Figure 135.2 is a scatter plot in IFAR and adiabat space of recent cryogenic DT capsule implosions on OMEGA (i.e., each point represents an implosion on OMEGA with the indicated adiabat and IFAR). These implosions were selected from a set of over 60 experiments (performed over the past 18 months) based on a set of "physics quality" criteria that include target alignment at shot time (within 15 μm of target chamber center), ice-layer quality [less than 2-μm root mean square (rms) over all modes], and pulse-shape quality (typically picket energies within 10% of the design specification). The shaded region for

E21735JR
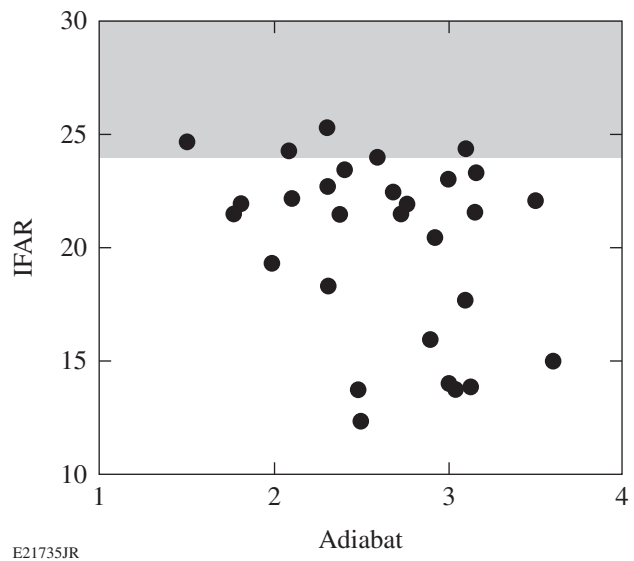
Figure 135.2
A scatter plot in IFAR–adiabat design space of 29 cryogenic DT implosions on OMEGA. Each black circle represents an implosion with the specific post-shot calculated values of IFAR and adiabat. The shaded region represents the ignition-relevant region of this design space. IFAR: in-flight aspect ratio.

E21736JR
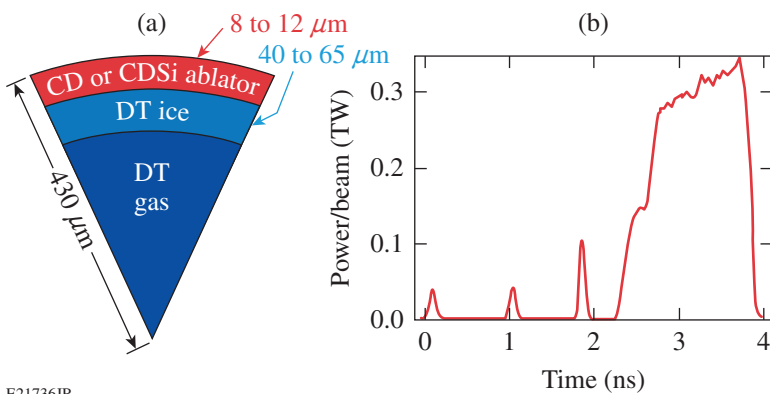
Figure 135.1
(a) The standard cryogenic DT capsule imploded on OMEGA consists of a thin CD or doped-CD ablator fill with several hundred atm of DT gas to create a 40- to 60-μm-thick ice layer. (b) The standard 25-kJ drive pulse consists of a series of three pickets used to establish the shell adiabat and control shock coalescence and a high-intensity main drive.

IFAR > 23 shows the approximate design space for ignition with implosion velocities between 350 and 400 km/s.

Figure 135.1(a) shows the range of ablator and ice thickness used for the points shown in Fig. 135.2. The implosion velocities range from 250 km/s to 380 km/s (e.g., a 9.2-μm CD ablator with an ice layer of 48 μm is predicted to achieve a V_{imp} of 350 km/s). Although the adiabat, IFAR, and V_{imp} are calculated quantities [based on the one-dimensional (1-D) design code *LILAC*[26]], the V_{imp} is confirmed experimentally by measuring the implosion burn history using the neutron temporal diagnostic (NTD).[27] *LILAC* incorporates nonlocal thermal transport[12] and a stimulated Brillouin scattering (SBS) model[8] to account for cross-beam energy transfer. A 10% change in the predicted velocity is a timing shift of 150 ps in the NTD. The absolute temporal accuracy of the NTD is 25 ps, so the implosion velocity is known to within a few percent.

Measurements and Discussion

The ICF Lawson criterion[23] can be used to connect the design parameters V_{imp}, adiabat, and IFAR to the experimentally measured observables. These observables include the primary neutron yield Y_n, the compressed fuel areal density ρR, the hot-spot ion temperature T_{ion}, the absorbed laser energy, and the neutron burn history. The Lawson criterion is defined as $\chi = P\tau/P\tau(T)_{ign} > 1$ (Ref. 28), where P is the plasma pressure and τ is the energy confinement time. In Ref. 28, Betti *et al.* derived an approximate 1-D ignition parameter based on the generalized Lawson criterion

$$\chi(1\text{-}D) \sim \left(\rho R^{no\,\alpha}\right)^{0.8} \times \left(T_{ion}^{no\,\alpha}/4.4\right)^{1.8} > 1, \qquad (1)$$

where T_{ion} is given in keV and ρR in g/cm^2. The superscript "no α" indicates that alpha-particle energy deposition is turned off in the 1-D simulations used to validate the analytic scaling. Recognizing that implosion nonuniformities significantly degrade 1-D performance, the authors used a simple three-dimensional (3-D) burn model to derive a generalized Lawson criterion

$$\chi(3\text{-}D) \sim \left(\rho R^{no\,\alpha}\right)^{0.8} \times \left(T_{ion}^{no\,\alpha}/4.4\right)^{1.8} \times \text{YOC}_{3\text{-}D}^m. \qquad (2)$$

YOC$_{3\text{-}D}$ is the ratio of the estimated 3-D yield to the predicted 1-D yield and m is analytically given as 0.64 but is between 0.4 and 0.5 based on fitting simulation yields with an ignition criterion of $\chi \sim 1$. It is difficult to use this form of χ to evaluate absolute implosion performance given the dependence on simulations and the measured T_{ion}, which is sensitive to fuel motion. Therefore, Betti *et al.*[24] modified Eq. (2) to remove the

explicit dependence on the YOC and replace the T_{ion} with the absolute yield Y_n. This version of the "measurable" generalized Lawson criterion for ICF is given by

$$\chi \sim \left(\rho R^{no\,\alpha}\right)^{0.61} \times \left(0.24\,Y_n/M_{fuel}\right)^{0.34}, \qquad (3)$$

where ρR is in g/cm^2, Y_n is in units of 10^{16}, and the fuel mass M_{fuel} is in mg. This form of χ depends only on the measured fuel ρR and the neutron yield and is roughly equivalent to the cube root of the experimental ignition threshold factor (ITFx) derived by Haan *et al.*[22]

It has been shown[24] that ignition hydrodynamically equivalent implosions on OMEGA occur for values of $\chi \gtrsim 0.16$. This can be satisfied for a range of areal densities and yields. Given that a ρR of ~300 mg/cm^2 has already been demonstrated on OMEGA,[3,20] a $\chi \sim 0.16$ corresponds to a yield of 4×10^{13}. These values of Y_n and ρR provide a convenient metric for demonstrating ignition hydrodynamically equivalent implosion performance with symmetric direct drive on OMEGA and are consistent with an earlier analysis discussed in Ref. 20.

Figure 135.3 shows the dependence of the 1-D fractional measured ρR ($\rho R/\rho R_{1\text{-}D}$) as a function of the calculated fuel adiabat [Fig. 135.3(a)] and IFAR [Fig. 135.3(b)] for the database shown in Fig. 135.2. As expected, the fraction of the 1-D ρR produced in the implosions is lower for higher-convergence, lower-adiabat implosions. The trend of lower ρR with decreasing shell stability is also clear as a function of IFAR. The measured fraction of the 1-D ρR approaches 80% for values of the adiabat above ~2.5 and values of IFAR below ~20 (note that

E21738JR

Figure 135.3
(a) The correlation between the ratio of the measured and 1-D–predicted areal density and the calculated adiabat for the implosions in Fig. 135.2 shows a drop in the measured ρR for adiabats generally less than 2.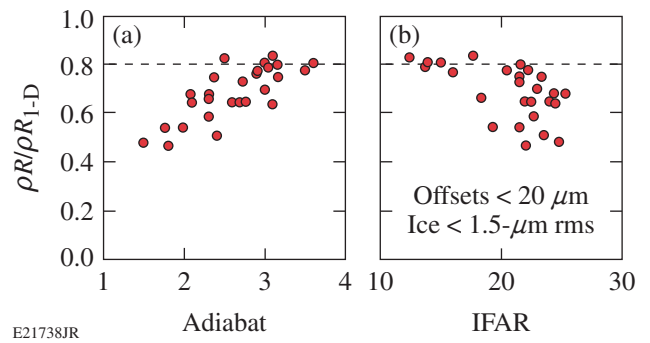5. (b) The correlation between the ratio of the measured and 1-D–predicted areal density and the calculated IFAR for the implosions in Fig. 135.2 shows a drop in the measured ρR for IFAR's generally greater than 17.

the velocities for the implosions at these lower adiabats range from 280 to 320 km/s). Burn truncation[29] and ^{3}He buildup in the capsule caused by tritium β-decay can account for much of the degradation relative to the prediction. Estimates of the void pressure resulting from the buildup of ^{3}He are sufficient to cause a degradation of the predicted ρR of 10% to 15%. The 1-D prediction for the points in Fig. 135.3 does not take into account the increased pressure in the capsule related to ^{3}He buildup as the target ages.

The ρR measurements in Fig. 135.3 were obtained with two independent instruments: the magnetic recoil spectrometer (MRS)[30] and a highly collimated neutron time-of-flight (nTOF) detector.[31] The areal density inferred from the nTOF is based on a different part of the (n,T/D) scattering cross section[32] than that used in the reduction of the MRS data. While the MRS measures the fraction of the primary yield forward scattered by the compressed DT, the nTOF measures the (n,T) backscatter edge at 3.5 MeV to infer the triton density in the compressed fuel. The systematic error on the ρR inferred from the nTOF is somewhat higher (estimated to be <15%) than that from the MRS (6%). However, where both measurements are available (a small number of the experiments did not have the nTOF available), the value of the ρR used in Fig. 135.3 (and subsequent analyses) is the average of the two measurements.

Figure 135.4 is a duplicate of Fig. 135.2 with contours of constant $\rho R/\rho R_{1\text{-}D}$ based on the same database of shots. In this two-dimensional (2-D) design space, a stability boundary sug-

gested by Figs. 135.3(a) and 135.3(b) is clearly evident. For this set of experiments, the edge of the boundary can be roughly defined as IFAR = $20(\alpha/3)^{0.8}$. While Fig. 135.3(b) suggests that the measured ρR begins to deviate from the 1-D prediction for values of IFAR > 17, the 2-D contour plot clearly shows that the 1-D ρR is recovered for larger IFAR as long as the adiabat is suitably large. This further confirms that the stability of these targets is sensitive to design details that can be fully accessed based on the flexibility of the target platform.

Figure 135.5 shows the measured (red circles) and 1-D–predicted (black circles) Y_n [Fig. 135.5(a)] and T_{ion} [Fig. 135.5(b)]

Figure 135.4
Contours of the measured areal-density fraction relative to 1-D prediction ($\rho R/\rho R_{1\text{-}D}$) show a steep drop for values of the IFAR above the line defined by $20(\alpha/3)^{0.8}$.

Figure 135.5
(a) The predicted 1-D and measured yields increase with increasing implosion velocity. The adiabat was increased to reach implosion velocities above 330 km/s. (b) While the 1-D ion temperature increases linearly with the implosion velocity, the measured temperature is fairly constant until the implosion velocity exceeds 330 km/s. The shaded regions indicate ignition-relevant implosion velocities.

as functions of the calculated implosion velocity. The measured yield increases uniformly with implosion velocity from 250 km/s to 380 km/s. The larger spread in the experimental yields for $V_{imp} \sim 300$ to 320 km/s suggests that the shell is becoming increasingly unstable as the implosion velocity is increased. The data points at higher V_{imp} were therefore acquired using a higher fuel adiabat to stabilize perturbation growth at the ablation surface and the ice–gas interface. This additional stabilization is clearly evident in Fig. 135.5(b), where there is little variation in the measured T_{ion} with increasing V_{imp} until the fuel adiabat is raised to access V_{imp} above ~320 km/s. With the higher-adiabat implosions, T_{ion} increases rapidly with V_{imp} reaching 90% to 95% of the prediction at 380 km/s.

Figure 135.6 is a duplicate of Fig. 135.2 with contours of constant $Y_n / Y_{n1\text{-D}}$ [this is the ratio of the measured and simulated yields from Fig. 135.5(a), commonly referred to as YOC]. The vertical contours indicate that the measured yield depends primarily on the adiabat for values of IFAR < 20 to 22. Only at the highest adiabat does the yield appear to be independent of IFAR for ignition-relevant values (a target is unlikely to ignite at these adiabats with the energy available on the NIF). The YOC for these few data points is >20%. The YOC for ignition-relevant values of the adiabat and IFAR is generally less than 10%.
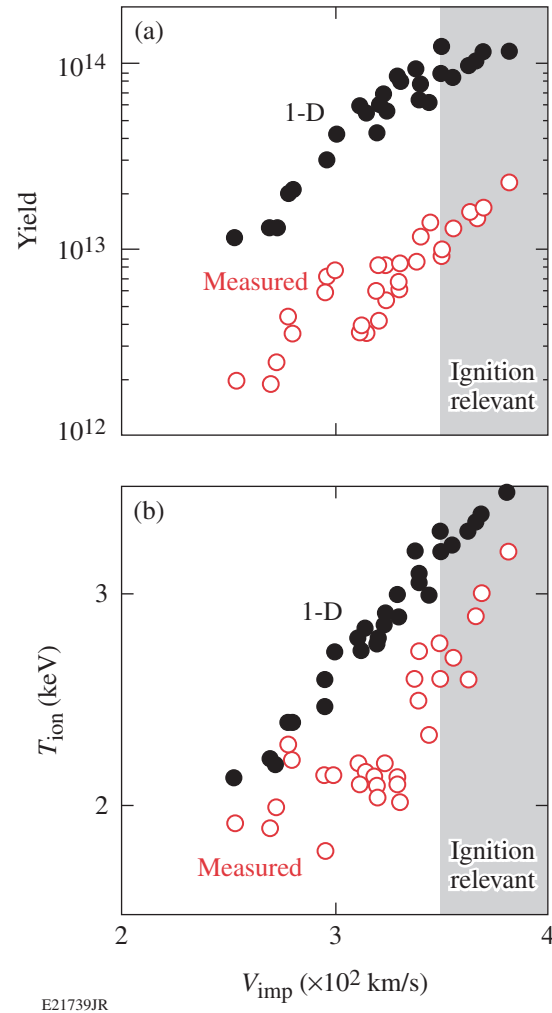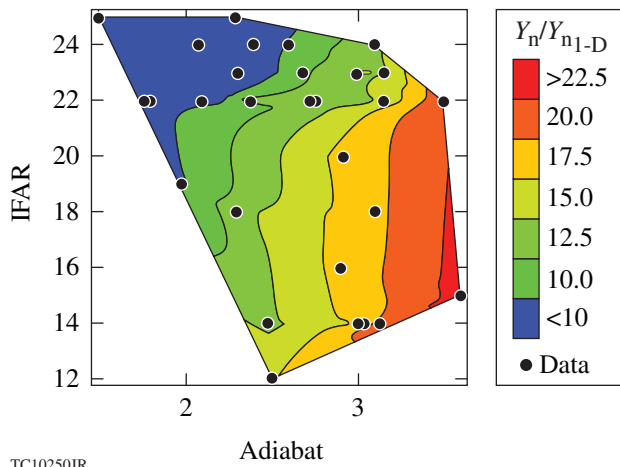

TC10250JR

Figure 135.6
Contours of the measured yield fraction relative to 1-D predictions [yield-over-clean (YOC)] show that the yield depends primarily on the adiabat for IFAR's generally less than 20.

The largest value of χ [Eq. (3)] in this data set is 0.09. For this shot (and several others in the 0.08 range), the values of the measured ρR and Y_n are approximately half of the values needed to demonstrate ignition hydrodynamically equivalent

implosion performance. These highest-performing implosions are not associated with ignition-relevant values of IFAR and adiabat. This is seen in Fig. 135.7, where contours of constant $\chi/\chi_{1\text{-D}}$ are plotted in the IFAR–adiabat space of Fig. 135.2. The contours clearly show that relative to 1-D prediction, target performance decreases with increasing IFAR and decreasing adiabat. Not surprisingly, this is consistent with the stability boundary identified in Fig. 135.4.

E21740JR
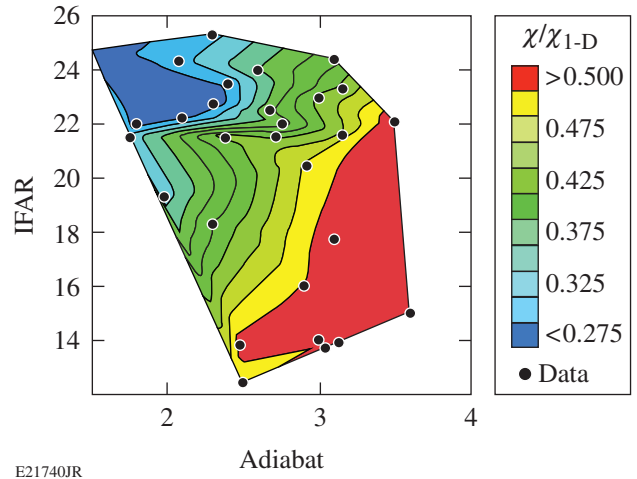
Figure 135.7
Contours of the measured χ fraction relative to the 1-D–predicted χ show a steep drop with increasing IFAR for ignition-relevant adiabats (<2.5).

Together, these data suggest that as the design approaches ignition hydrodynamic equivalence, the fuel shell breaks apart during acceleration, leading to a drop in the burn-averaged fuel areal density. The subsequent loss in the hot-spot pressure and temperature leads to a drop in the primary yield. The shell breakup during acceleration suggests Rayleigh–Taylor (RT) perturbation growth from the ablation surface (as opposed to deceleration-driven growth at the ice–gas interface). Such growth would be expected to mix ablator material into the core. This mixing is confirmed in Fig. 135.8, where the yield-normalized x-ray emission from the core is plotted as a function of the adiabat. The yield normalization factor comes from a fit of the 1-D–predicted x-ray emission. When normalized to $Y_{1\text{-D}}^{0.57}$, simulated core x-ray emission is approximately constant for all of the experiments. This is shown by the black circles in Fig. 135.8. If carbon mixing enhances the core emission, this should be evident when the experimental x-ray emission is normalized to $Y_{meas}^{0.57}$. These values are plotted as the red squares. The data clearly show that when the adiabat is less than 2.5, the core x-ray emission is strongly enhanced relative to the high-adiabat experiments, whereas Figs. 135.4 and 135.6 show that the shell is likely integral through acceleration. The
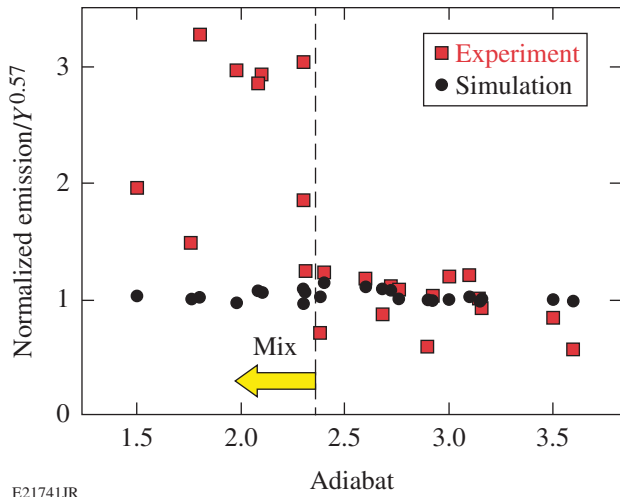
E21741JR

Figure 135.8
The yield-normalized x-ray emission from 1-D simulations (black circles) and cryogenic DT implosions (red squares) is plotted as a function of the implosion adiabat. The experimental points show a pronounced increase in the x-ray emission relative to 1-D prediction for adiabats generally less than 2.5, indicating that this emission may be due to higher-Z carbon mixing into the core.

normalization of the experimental and simulated points at high adiabats is arbitrary, as are the units of the normalized emission. The simulated x-ray emission used to establish the yield normalization is restricted to the sensitivity range of the gated x-ray imager used for the measurement (roughly 4 to 7 keV).

Capsule Surface Quality and 2-D Simulations

As discussed in **Measurements and Discussion** (p. 147), the accumulated data suggest a high level of ablator mixing into the hot spot at peak burn. This level of mix would require a significant source of perturbations on the capsule surface to drive CD into the core before stagnation. The shadowgraphy-based imaging system used to characterize the ice-layer quality was refocused to image the capsule surface. Figure 135.9 shows a stitched image in pixel space of five capsule surface images acquired at the same focal depth as the target was rotated. The stitched image contains about 2/3 of the capsule surface and
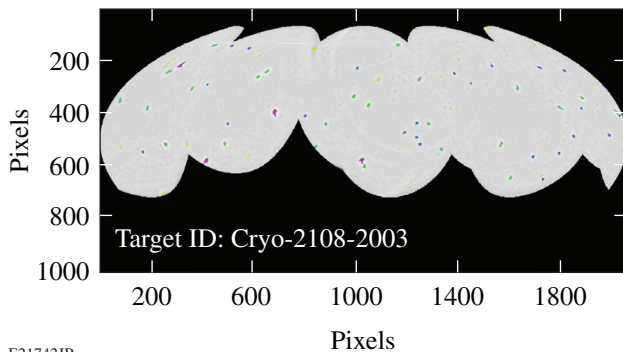
shows dozens of surface "defects" distributed randomly (there is no discernible pattern from one target to another) across the surface.

A detailed optical analysis of these defects confirms that most of the features reside on the outer capsule surface and originate during the high-pressure fill and cooling cycle (Ref. 18 describes the permeation filling process and the DT layering/characterization in detail), i.e., the features do not correspond with fabrication defects identified prior to the fill. A subset of the filled capsules has a small number of dendritic defects on the inner surface of the CD shell. An analysis of one of these inner surface dendritic defects following a controlled depressurization of a filled capsule showed that the radial depth is of the order of 0.1 μm or less, within the smoothness specification for the capsule.

Every target imploded on OMEGA since January 2012 has had the surface defects analyzed based on images such as the one shown in Fig. 135.9. The analysis identifies the type of defect (outer surface or inner surface) and the defect area. Figure 135.10(a) is a plot of the defect-size distribution for the targets filled in 2012 (48 total). The average defect size is ~140 μm^2; the imaging system is capable of resolving features with an area as small as 20 μm^2. Figure 135.10(b) shows a histogram of the target defect frequency distribution (bin size is ten defects). The defect count can exceed 100 on a single target. The total defect area for the targets discussed in this article ranged from a few thousand up to 15,000 μm^2 (nearly 1% of the total capsule surface area). The variation in defect count and total area from target to target and fill to fill is not understood.

Two-dimensional simulations of a single isolated surface defect suggest that the defects account for much of the observed target performance degradation relative to 1-D prediction. The implosion performance of several targets was simulated by assuming a uniform distribution of constant-size defects

E21742JR

Figure 135.9
A stitched set of images of a cryogenic DT capsule surface during characterization. The image shows dozens of surface defects associated with the high-pressure DT permeation fill. The defects are likely frozen gas contaminants in the DT fuel.
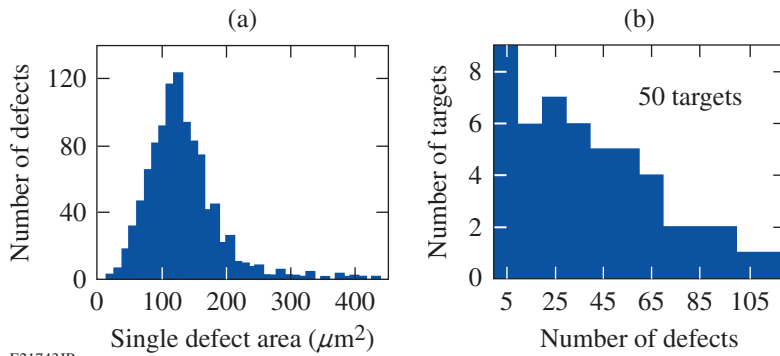
(a)

(b)

50 targets

Figure 135.10
(a) The defect-size distribution for the targets characterized in 2012 show that the average defect size is about 140 μm^2.
(b) The frequency distribution of the defects on 50 targets filled and characterized in 2012. Most targets have several dozen individual defects.

E21743JR

(80 μm^2) with a thickness of 1 μm. The thickness of the defects cannot be measured with the optical imaging system used to characterize the DT ice layer (limited spatial resolution and contrast) unless they can be resolved on the limb of the images. In some cases this has been possible; however, most of the defects cannot be identified on the limb of the capsule images. A thickness of 1 μm was used in the simulations as a compromise: some will be larger while most are smaller. A 2-D simulation with a single defect and reflecting boundary conditions was performed using a sector defined as $4\pi/N$, where N is the number of defects on the target. The reflecting boundaries mimic the presence of neighboring defects in this simplified 2-D simulation. Assuming that the defects are identical and uniformly distributed around a target, the predicted yield is then N times the results of the simulation. The simulated ion temperature and neutron-averaged ρR are taken as the average for the target. Table 135.I shows the results for shot 66999 (August 2012). The first row is the 1-D prediction using *LILAC* with nonlocal (NL) thermal transport and an SBS model to account for CBET in the absorbed energy.[8] The second row is the 2-D simulation described above including single-beam laser imprint[33] but no isolated defects. The third row is the 2-D simulation including the average isolated defect with $N =$ 150. The fourth row is the experimentally measured values. The isolated defect simulation reproduces the experimental

measurements reasonably well, while the imprint-only simulations cannot explain the observed implosion performance. The other simulated implosions show a quantitatively similar behavior with respect to measured target performance. While the number of defects simulated was larger than the average number shown in Fig. 135.10(b) and the area of each defect was less than the average shown in Fig. 135.10(a), the total defect area was similar to the average of most targets in the 2012 database. The key point is that injecting the proper amount of ablator material into the core via ablation-front RT growth reproduces the experimental performance observables.

Further progress toward the demonstration of ignition hydrodynamically equivalent implosion performance requires that these isolated defects be eliminated from the capsules. Few, if any, of these defects are particulate in nature. Steps taken in 2011 eliminated the identified sources for particulate debris. The defects are condensed non-hydrogenic gases entrained in the closed DT-fuel supply; analysis confirms that the fuel supply contains nearly 0.5% organics and hundreds of ppm of nitrogen, water, and CO_2. The organics are likely generated by the energetic tritium β-decay electrons that liberate carbon atoms from the CD capsule and the cryogenic epoxies used in the target mounts (the target and support structures are immersed in DT gas during the diffusion fill and the pressure is ramped up to hundreds of atmospheres at room temperature over a 24-h period). Since the DT fuel supply is operated as a closed loop, organics formed during a fill remain entrained in the fuel for subsequent fills.

The gases condense on the outer surface of the capsule as it is being cooled under pressure. As the temperature of the DT approaches the triple point, the DT liquefies, immersing the capsule and effectively stopping further contaminant gas condensation from the vapor phase on the outer surface. The contaminant gases are presumably on the inside of the capsule as well since the shell is quite permeable at room temperature. The gases likely form monolayers on the inner surface as the

Table 135.I: For shot 66999, the results of 1-D simulations including nonlocal thermal transport and cross-beam energy transfer, 2-D simulations with imprint, and 2-D simulations based on an isolated surface defect are compared with the measured yield, areal density, and ion temperature.

Shot 66999	Y_n ($\times 10^{13}$)	ρR (mg/cm^2)	T_{ion} (keV)
1-D (NL + SBS)	7.9	238	3.1
2-D imprint	4.5	242	3.4
2-D defect	1.8	151	2.7
Measured	1.2	175	2.5

temperature falls below the various triple points. Based on the characterization possible to date, there is no visible evidence of crystalline or condensation-related features on the inner surface of the CD shell. Any features on the inner surface would need to first feed out to the ablation surface (where the amplitudes would be quite reduced) to be associated with carbon mixing in the core (recall Fig. 135.8).

Two facility projects are underway to eliminate these "trace" gases in the fuel supply. The first is a PdAg filter[34] that passes only hydrogen into the high-pressure permeation cell with the capsules. This filter will be implemented in early 2013. The second project is an isotope separation unit that will remove all contaminants from the DT-fuel supply including protium (^{1}H). Protium forms HD, HT, and HH molecules that lower the effective triple point of the fuel, impacting layer formation and the density of the void. This system is expected to become operational in late 2013.

Experimental Ignition Threshold Factor

The goal of the National Ignition Campaign (NIC) was to demonstrate alpha heating and ignition using indirectly driven (ID) cryogenic DT implosions on the NIF.[35] Using multidimensional hydrodynamic simulations, Haan *et al.*[22] derived a convenient metric (ITFx) for tracking the relative implosion performance as capsule and drive parameters were tuned to achieve the required implosion symmetry, fuel adiabat, and implosion velocity. The ITFx is given by

$$\text{ITFx (ID)} = \left(Y_n \big/ 3.2 \times 10^{15}\right) \times \left(\text{DSR}/0.07\right)^{2.3}, \qquad (4)$$

where DSR is the "down-scatter ratio"[36] in percent and related[37] to the total fuel areal density by ρR (g/cm^2) = 21 × DSR(%), i.e., the normalization factor of 0.07 is effectively a fuel areal density of 1.5 g/cm^2. The normalization factors on the yield and areal density are set so that an ITFx of unity implies a 50% probability that the target will ignite (given the spectrum of tolerances used in the simulations). Symmetric direct-drive (DD) implosions on OMEGA can be plotted using the ITFx(ID) on an equivalent performance basis by using the standard hydrodynamic relations[24] $\rho R \sim E_L^{1/3}$, $Y \sim T_i^{4.7} \times \rho R^{0.56} \times M_{\text{fuel}}$, and $T \sim E^{0.07}$. The ignition Y_n and ρR in Eq. (4) can be replaced by laser energy and mass-scaled quantities from OMEGA cryogenic DT implosions. The OMEGA ignition-equivalent ITFx is then

$$\text{ITFx (NIF DD)} = \text{ITFx (ID }\Omega) \times \left(E_{\text{NIF}} \big/ E_\Omega\right)^{1.28}$$
$$\times \left(M_{\text{NIF}} \big/ M_\Omega\right) \times \left(\text{YOC}_{\text{NIF}} \big/ \text{YOC}_\Omega\right), \qquad (5)$$

where ITFx (ID Ω) is Eq. (4) with the OMEGA (Ω) measured quantities, E is the laser energy, M is the fuel mass, and YOC is based on an equivalent perturbation spectrum for each facility.[24] The assumption is that the YOC on the NIF will be higher than on OMEGA for an equivalent perturbation spectrum, given the larger capsule and consequent smaller perturbation wavelengths. For E_{NIF} = 1.8 MJ, E_Ω = 25 kJ, M_{NIF} = 0.17 mg, M_Ω = 0.02 mg, and YOC$_{\text{NIF}}$ = 50% and YOC$_\Omega$ = 25% (best YOC$_\Omega$ for an adiabat of ~3 and V_{imp} of ~350 km/s),

$$\text{ITFx (NIF DD)} = 3505 \times \text{ITFx (ID }\Omega). \qquad (6)$$

Figure 135.11 shows the distribution of the implosions discussed above in a plot of measured yield and ρR (as in Fig. 135.2 each point represents an experiment). The blue squares are implosions using pure-CD ablators while the orange diamonds are Si-doped ablators (typically a few atom percent of silicon in the outer few microns of the shell). The red circles are from a high-areal-density series of experiments performed in 2009 (Refs. 3 and 20). There is no discernible difference between the doped and undoped ablators, confirming the conclusion from Table 135.I that imprint alone cannot explain the current target performance. Curves of constant ITFx (NIF DD) from Eq. (6) are superimposed. The best-performing implosions on OMEGA have achieved an equivalent NIF direct-drive ITFx
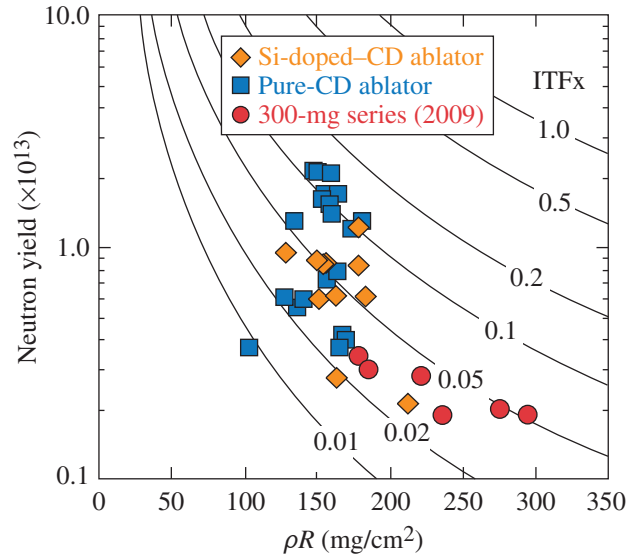
TC10124JR

Figure 135.11
The implosions represented in Fig. 135.2 are plotted according to the measured yield and areal density. Curves of constant NIF-equivalent direct-drive ITFx [Eq. (6)] are also plotted. The blue squares are pure-CD ablators while the orange diamonds are Si-doped–CD ablators. The red circles are from a high-areal-density series of experiments performed in 2009 (Refs. 3 and 20).

of nearly 0.2 (this includes the $2\times$ multiplier from the YOC scaling). The highest ρR to date in an OMEGA DT implosion ($\sim$295 mg/cm^2) produced an ITFx (NIF DD) nearly $3\times$ less as a result of the low yield. An ITFx (NIF DD) of unity is satisfied for an areal density of 300 mg/cm^2 and a yield of 4×10^{13}, very similar to the values derived by Betti *et al.*[24] from the generalized Lawson criterion for ICF and discussed above.

It is apparent from Fig. 135.11 that recent experiments have not produced areal densities above 200 mg/cm^2 regardless of the design adiabat and the implosion velocity. All attempts to reduce the adiabat to increase the areal density led to a decrease in both the yield and areal densities; at an adiabat of 3, the measured yields and areal densities drop to below 10% and 50% of 1-D predictions, respectively (with ITFx values well below 0.1). This suggests that ablation-front hydrodynamic instabilities remain the leading cause of the breakup of the fuel shell in-flight.

Conclusion

The goal of the cryogenic DT implosion experiments at LLE is to demonstrate ignition hydrodynamic similarity. Recent cryogenic DT implosions on OMEGA have probed a broad region of design space that includes fuel adiabats from <2 to 4, IFAR's from <15 to more than 25, and implosion velocities from 250 to 380 km/s. Several of the targets would have demonstrated ignition hydrodynamic equivalence had the measured performance agreed with the 1-D prediction. The key to this rapid progress is the flexible symmetric direct-drive target platform on the OMEGA laser. With the peak drive intensity defined by the hydro scaling discussed in **Hydrodynamic Similarity and Experimental Design** (p. 145), the adiabat of any layered DT target can be easily changed by adjusting the laser-drive picket energies and relative timings, while the implosion velocity and IFAR are set by the mass of the ablator and ice.

The conclusion from the data and 2-D simulations is that the stability of the imploding shell is compromised by dozens of isolated outer-surface defects. These defects act as perturbation seeds that grow rapidly at the ablation surface and mix ablator material into the core. The defects that appear on the capsules following the permeation fill process are most likely caused by contaminant gases in the DT fuel supply that freeze on the surface of the capsule as it is being cooled under pressure.

High implosion velocities are achieved with higher-adiabat target designs that stabilize the hydro-instability growth at the ablation surface. At the highest adiabats (4), the measured areal density and primary neutron yield are >80% to 90% and ≥25% of the 1-D prediction, respectively. Comparable performance relative to 1-D at adiabats of 2.0 to 2.5 is needed to demonstrate ignition hydrodynamic similarity.

REFERENCES

1. T. R. Boehly, D. L. Brown, R. S. Craxton, R. L. Keck, J. P. Knauer, J. H. Kelly, T. J. Kessler, S. A. Kumpan, S. J. Loucks, S. A. Letzring, F. J. Marshall, R. L. McCrory, S. F. B. Morse, W. Seka, J. M. Soures, and C. P. Verdon, Opt. Commun. **133**, 495 (1997).

2. W. J. Hogan, E. I. Moses, B. E. Warner, M. S. Sorem, and J. M. Soures, Nucl. Fusion **41**, 567 (2001).

3. V. N. Goncharov, T. C. Sangster, T. R. Boehly, S. X. Hu, I. V. Igumenshchev, F. J. Marshall, R. L. McCrory, D. D. Meyerhofer, P. B. Radha, W. Seka, S. Skupsky, C. Stoeckl, D. T. Casey, J. A. Frenje, and R. D. Petrasso, Phys. Rev. Lett. **104**, 165001 (2010).

4. P. B. Radha, F. J. Marshall, J. A. Marozas, A. Shvydky, I. Gabalski, T. R. Boehly, T. J. B. Collins, R. S. Craxton, D. H. Edgell, R. Epstein, J. A. Frenje, D. H. Froula, V. N. Goncharov, M. Hohenberger, R. L. McCrory, P. W. McKenty, D. D. Meyerhofer, R. D. Petrasso, T. C. Sangster, and S. Skupsky, Phys. Plasmas **20**, 056306 (2013).

5. S. Skupsky, J. A. Marozas, R. S. Craxton, R. Betti, T. J. B. Collins, J. A. Delettrez, V. N. Goncharov, P. W. McKenty, P. B. Radha, T. R. Boehly, J. P. Knauer, F. J. Marshall, D. R. Harding, J. D. Kilkenny, D. D. Meyerhofer, T. C. Sangster, and R. L. McCrory, Phys. Plasmas **11**, 2763 (2004).

6. S. Skupsky, R. S. Craxton, F. J. Marshall, R. Betti, T. J. B. Collins, R. Epstein, V. N. Goncharov, I. V. Igumenshchev, J. A. Marozas, P. W. McKenty, P. B. Radha, J. D. Kilkenny, D. D. Meyerhofer, T. C. Sangster, and R. L. McCrory, J. Phys. IV France **133**, 233 (2006).

7. S. X. Hu, G. Fiksel, V. N. Goncharov, S. Skupsky, D. D. Meyerhofer, and V. A. Smalyuk, Phys. Rev. Lett. **108**, 195003 (2012).

8. I. V. Igumenshchev, W. Seka, D. H. Edgell, D. T. Michel, D. H. Froula, V. N. Goncharov, R. S. Craxton, L. Divol, R. Epstein, R. Follett, J. H. Kelly, T. Z. Kosc, A. V. Maximov, R. L. McCrory, D. D. Meyerhofer, P. Michel, J. F. Myatt, T. C. Sangster, A. Shvydky, S. Skupsky, and C. Stoeckl, Phys. Plasmas **19**, 056314 (2012).

9. S. X. Hu, V. A. Smalyuk, V. N. Goncharov, J. P. Knauer, P. B. Radha, I. V. Igumenshchev, J. A. Marozas, C. Stoeckl, B. Yaakobi, D. Shvarts, T. C. Sangster, P. W. McKenty, D. D. Meyerhofer, S. Skupsky, and R. L. McCrory, Phys. Rev. Lett. **100**, 185003 (2008).

10. P. B. Radha, C. Stoeckl, V. N. Goncharov, J. A. Delettrez, D. H. Edgell, J. A. Frenje, I. V. Igumenshchev, J. P. Knauer, J. A. Marozas, R. L.

McCrory, D. D. Meyerhofer, R. D. Petrasso, S. P. Regan, T. C. Sangster, W. Seka, and S. Skupsky, Phys. Plasmas 18, 012705 (2011).

11. T. R. Boehly, V. N. Goncharov, W. Seka, M. A. Barrios, P. M. Celliers, D. G. Hicks, G. W. Collins, S. X. Hu, J. A. Marozas, and D. D. Meyerhofer, Phys. Rev. Lett. 106, 195005 (2011).

12. V. N. Goncharov, T. C. Sangster, P. B. Radha, R. Betti, T. R. Boehly, T. J. B. Collins, R. S. Craxton, J. A. Delettrez, R. Epstein, V. Yu. Glebov, S. X. Hu, I. V. Igumenshchev, J. P. Knauer, S. J. Loucks, J. A. Marozas, F. J. Marshall, R. L. McCrory, P. W. McKenty, D. D. Meyerhofer, S. P. Regan, W. Seka, S. Skupsky, V. A. Smalyuk, J. M. Soures, C. Stoeckl, D. Shvarts, J. A. Frenje, R. D. Petrasso, C. K. Li, F. Séguin, W. Manheimer, and D. G. Colombant, Phys. Plasmas 15, 056310 (2008).

13. S. X. Hu, V. Smalyuk, V. N. Goncharov, S. Skupsky, T. C. Sangster, D. D. Meyerhofer, and D. Shvarts, Phys. Rev. Lett. 101, 055002 (2008).

14. B. Yaakobi, P.-Y. Chang, A. A. Solodov, C. Stoeckl, D. H. Edgell, R. S. Craxton, S. X. Hu, J. F. Myatt, F. J. Marshall, W. Seka, and D. H. Froula, Phys. Plasmas 19, 012704 (2012).

15. V. N. Goncharov, J. P. Knauer, P. W. McKenty, P. B. Radha, T. C. Sangster, S. Skupsky, R. Betti, R. L. McCrory, and D. D. Meyerhofer, Phys. Plasmas 10, 1906 (2003).

16. P. B. Radha, J. A. Marozas, F. J. Marshall, A. Shvydky, T. J. B. Collins, V. N. Goncharov, R. L. McCrory, P. W. McKenty, D. D. Meyerhofer, T. C. Sangster, and S. Skupsky, Phys. Plasmas 19, 082704 (2012).

17. C. Stoeckl, C. Chiritescu, J. A. Delettrez, R. Epstein, V. Yu. Glebov, D. R. Harding, R. L. Keck, S. J. Loucks, L. D. Lund, R. L. McCrory, P. W. McKenty, F. J. Marshall, D. D. Meyerhofer, S. F. B. Morse, S. P. Regan, P. B. Radha, S. Roberts, T. C. Sangster, W. Seka, S. Skupsky, V. A. Smalyuk, C. Sorce, J. M. Soures, R. P. J. Town, J. A. Frenje, C. K. Li, R. D. Petrasso, F. H. Séguin, K. Fletcher, S. Padalino, C. Freeman, N. Izumi, R. Lerche, and T. W. Phillips, Phys. Plasmas 9, 2195 (2002).

18. T. C. Sangster, R. Betti, R. S. Craxton, J. A. Delettrez, D. H. Edgell, L. M. Elasky, V. Yu. Glebov, V. N. Goncharov, D. R. Harding, D. Jacobs-Perkins, R. Janezic, R. L. Keck, J. P. Knauer, S. J. Loucks, L. D. Lund, F. J. Marshall, R. L. McCrory, P. W. McKenty, D. D. Meyerhofer, P. B. Radha, S. P. Regan, W. Seka, W. T. Shmayda, S. Skupsky, V. A. Smalyuk, J. M. Soures, C. Stoeckl, B. Yaakobi, J. A. Frenje, C. K. Li, R. D. Petrasso, F. H. Séguin, J. D. Moody, J. A. Atherton, B. D. MacGowan, J. D. Kilkenny, T. P. Bernat, and D. S. Montgomery, Phys. Plasmas 14, 058101 (2007).

19. T. C. Sangster, V. N. Goncharov, P. B. Radha, V. A. Smalyuk, R. Betti, R. S. Craxton, J. A. Delettrez, D. H. Edgell, V. Yu. Glebov, D. R. Harding, D. Jacobs-Perkins, J. P. Knauer, F. J. Marshall, R. L. McCrory, P. W. McKenty, D. D. Meyerhofer, S. P. Regan, W. Seka, R. W. Short, S. Skupsky, J. M. Soures, C. Stoeckl, B. Yaakobi, D. Shvarts, J. A. Frenje, C. K. Li, R. D. Petrasso, and F. H. Séguin, Phys. Rev. Lett. 100, 185006 (2008).

20. T. C. Sangster, V. N. Goncharov, R. Betti, T. R. Boehly, D. T. Casey, T. J. B. Collins, R. S. Craxton, J. A. Delettrez, D. H. Edgell, R. Epstein, K. A. Fletcher, J. A. Frenje, V. Yu. Glebov, D. R. Harding, S. X. Hu, I. V. Igumenshchev, J. P. Knauer, S. J. Loucks, C. K. Li, J. A. Marozas, F. J. Marshall, R. L. McCrory, P. W. McKenty, D. D. Meyerhofer, P. M. Nilson, S. P. Padalino, R. D. Petrasso, P. B. Radha, S. P. Regan, F. H.

Seguin, W. Seka, R. W. Short, D. Shvarts, S. Skupsky, V. A. Smalyuk, J. M. Soures, C. Stoeckl, W. Theobald, and B. Yaakobi, Phys. Plasmas 17, 056312 (2010).

21. P. B. Radha, R. Betti, T. R. Boehly, J. A. Delettrez, D. H. Edgell, V. N. Goncharov, I. V. Igumenshchev, J. P. Knauer, J. A. Marozas, F. J. Marshall, R. L. McCrory, D. D. Meyerhofer, S. P. Regan, T. C. Sangster, W. Seka, S. Skupsky, A. A. Solodov, C. Stoeckl, W. Theobald, J. A. Frenje, D. T. Casey, C. K. Li, and R. D. Petrasso, IEEE Trans. Plasma Sci. 39, 1007 (2011).

22. S. W. Haan, J. D. Lindl, D. A. Callahan, D. S. Clark, J. D. Salmonson, B. A. Hammel, L. J. Atherton, R. C. Cook, M. J. Edwards, S. Glenzer, A. V. Hamza, S. P. Hatchett, M. C. Herrmann, D. E. Hinkel, D. D. Ho, H. Huang, O. S. Jones, J. Kline, G. Kyrala, O. L. Landen, B. J. MacGowan, M. M. Marinak, D. D. Meyerhofer, J. L. Milovich, K. A. Moreno, E. I. Moses, D. H. Munro, A. Nikroo, R. E. Olson, K. Peterson, S. M. Pollaine, J. E. Ralph, H. F. Robey, B. K. Spears, P. T. Springer, L. J. Suter, C. A. Thomas, R. P. Town, R. Vesey, S. V. Weber, H. L. Wilkens, and D. C Wilson, Phys. Plasmas 18, 051001 (2011).

23. C. D. Zhou and R. Betti, Phys. Plasmas 15, 102707 (2008).

24. R. Betti, presented at the 24th IAEA Fusion Energy Conference, San Diego, CA, 8–13 October 2012.

25. H. A. Baldis and C. J. Walsh, Phys. Fluids 26, 1364 (1983).

26. J. Delettrez, R. Epstein, M. C. Richardson, P. A. Jaanimagi, and B. L. Henke, Phys. Rev. A 36, 3926 (1987).

27. R. A. Lerche, D. W. Phillion, and G. L. Tietbohl, Rev. Sci. Instrum. 66, 933 (1995).

28. R. Betti, P. Y. Chang, B. K. Spears, K. S. Anderson, J. Edwards, M. Fatenejad, J. D. Lindl, R. L. McCrory, R. Nora, and D. Shvarts, Phys. Plasmas 17, 058102 (2010).

29. P. B. Radha, T. J. B. Collins, J. A. Delettrez, Y. Elbaz, R. Epstein, V. Yu. Glebov, V. N. Goncharov, R. L. Keck, J. P. Knauer, J. A. Marozas, F. J. Marshall, R. L. McCrory, P. W. McKenty, D. D. Meyerhofer, S. P. Regan, T. C. Sangster, W. Seka, D. Shvarts, S. Skupsky, Y. Srebro, and C. Stoeckl, Phys. Plasmas 12, 056307 (2005).

30. J. A. Frenje, K. M. Green, D. G. Hicks, C. K. Li, F. H. Séguin, R. D. Petrasso, T. C. Sangster, T. W. Phillips, V. Yu. Glebov, D. D. Meyerhofer, S. Roberts, J. M. Soures, C. Stoeckl, K. Fletcher, S. Padalino, and R. J. Leeper, Rev. Sci. Instrum. 72, 854 (2001).

31. C. J. Forrest, P. B. Radha, V. Yu. Glebov, V. N. Goncharov, J. P. Knauer, A. Pruyne, M. Romanofsky, T. C. Sangster, M. J. Shoup III, C. Stoeckl, D. T. Casey, M. Gatu-Johnson, and S. Gardner, Rev. Sci. Instrum. 83, 10D919 (2012).

32. J. A. Frenje, C. K. Li, F. H. Séguin, D. T. Casey, R. D. Petrasso, D. P. McNabb, P. Navratil, S. Quaglioni, T. C. Sangster, V. Yu. Glebov, and D. D. Meyerhofer, Phys. Rev. Lett. 107, 122502 (2011).

33. V. A. Smalyuk, V. N. Goncharov, K. S. Anderson, R. Betti, R. S. Craxton, J. A. Delettrez, D. D. Meyerhofer, S. P. Regan, and T. C. Sangster, Phys. Plasmas 14, 032702 (2007).

34. H. Amandusson, L.-G. Ekedahl, and H. Dannetun, J. Membr. Sci. 193, 35 (2001).

35. J. D. Lindl and E. I. Moses, Phys. Plasmas **18**, 050901 (2011).

36. J. A. Frenje, D. T. Casey, C. K. Li, J. R. Rygg, F. H. Séguin, R. D. Petrasso, V. Yu. Glebov, D. D. Meyerhofer, T. C. Sangster, S. Hatchett, S. Haan, C. Cerjan, O. Landen, M. Moran, P. Song, D. C. Wilson, and R. J. Leeper, Rev. Sci. Instrum. **79**, 10E502 (2008).

37. A. J. Mackinnon, J. L. Kline, S. N. Dixit, S. H. Glenzer, M. J. Edwards, D. A. Callahan, N. B. Meezan, S. W. Haan, J. D. Kilkenny, T. Döppner, D. R. Farley, J. D. Moody, J. E. Ralph, B. J. MacGowan, O. L. Landen, H. F. Robey, T. R. Boehly, P. M. Celliers, J. H. Eggert, K. Krauter, G. Frieders, G. F. Ross, D. G. Hicks, R. E. Olson, S. V. Weber, B. K. Spears, J. D. Salmonsen, P. Michel, L. Divol, B. Hammel, C. A. Thomas, D. S. Clark, O. S. Jones, P. T. Springer, C. J. Cerjan, G. W. Collins, V. Y. Glebov, J. P. Knauer, C. Sangster, C. Stoeckl, P. McKenty, J. M. McNaney, R. J. Leeper, C. L. Ruiz, G. W. Cooper, A. G. Nelson, G. G. A. Chandler, K. D. Hahn, M. J. Moran, M. B. Schneider, N. E. Palmer, R. M. Bionta, E. P. Hartouni, S. LePape, P. K. Patel, N. Izumi, R. Tommasini, E. J. Bond, J. A. Caggiano, R. Hatarik, G. P. Grim, F. E. Merrill, D. N. Fittinghoff, N. Guler, O. Drury, D. C. Wilson, H. W. Herrmann, W. Stoeffl, D. T. Casey, M. G. Johnson, J. A. Frenje, R. D. Petrasso, A. Zylestra, H. Rinderknecht, D. H. Kalantar, J. M. Dzenitis, P. Di Nicola, D. C. Eder, W. H. Courdin, G. Gururangan, S. C. Burkhart, S. Friedrich, D. L. Blueuel, L. A. Bernstein, M. J. Eckart, D. H. Munro, S. P. Hatchett, A. G. Macphee, D. H. Edgell, D. K. Bradley, P. M. Bell, S. M. Glenn, N. Simanovskaia, M. A. Barrios, R. Benedetti, G. A. Kyrala, R. P. J. Town, E. L. Dewald, J. L. Milovich, K. Widmann, A. S. Moore, G. LaCaille, S. P. Regan, L. J. Suter, B. Felker, R. C. Ashabranner, M. C. Jackson, R. Prasad, M. J. Richardson, T. R. Kohut, P. S. Datte, G. W. Krauter, J. J. Klingman, R. F. Burr, T. A. Land, M. R. Hermann, D. A. Latray, R. L. Saunders, S. Weaver, S. J. Cohen, L. Berzins, S. G. Brass, E. S. Palma, R. R. Lowe-Webb, G. N. McHalle, P. A. Arnold, L. J. Lagin, C. D. Marshall, G. K. Brunton, D. G. Mathisen, R. D. Wood, J. R. Cox, R. B. Ehrlich, K. M. Knittel, M. W. Bowers, R. A. Zacharias, B. K. Young, J. P. Holder, J. R. Kimbrough, T. Ma, K. N. La Fortune, C. C. Widmayer, M. J. Shaw, G. V. Erbert, K. S. Jancaitis, J. M. DiNicola, C. Orth, G. Heestand, R. Kirkwood, C. Haynam, P. J. Wegner, P. K. Whitman, A. Hamza, E. G. Dzenitis, R. J. Wallace, S. D. Bhandarkar, T. G. Parham, R. Dylla-Spears, E. R. Mapoles, B. J. Kozioziemski, J. D. Sater, C. F. Walters, B. J. Haid, J. Fair, A. Nikroo, E. Giraldez, K. Moreno, B. Vanwonterghem, R. L. Kauffman, S. Batha, D. W. Larson, R. J. Fortner, D. H. Schneider, J. D. Lindl, R. W. Patterson, L. J. Atherton, and E. I. Moses, Phys. Rev. Lett. **108**, 215005 (2012).

Polar-Drive Experiments with Shimmed Targets on OMEGA

The polar-drive (PD) approach to directly driven, inertial confinement fusion[1] is being pursued as a means of demonstrating thermonuclear ignition at the National Ignition Facility[2] (NIF) with the beams of NIF in the indirect-drive configuration. Extensive experiments have been performed on the OMEGA Laser System[3] to evaluate this technique.[4–7] Ignition target designs using cryogenically cooled, DT-filled CH shells have been investigated using two-dimensional (2-D) hydrodynamic simulations.[8,9] These simulations suggest that gains of at least 20 to 30 can be achieved using 1.5 MJ of laser energy to irradiate a DT-ice-layer–bearing cryogenic target. In a recent simulation study by Collins *et al.*,[9] the drive symmetry was optimized by using a combination of beam pointing, beam shaping, pulse shaping, and target-layer shimming. Shimming uses an ideal ice-layer profile that is thinner at the target equator, where the beam illumination is the most oblique, and energy coupling to the target is reduced. The inclusion of an ice-layer shim increased the gain of the ignited plasma. Collins *et al.* also note that a shim applied to the CH capsule could equivalently be used to shape the imploding plasma.[9] This article presents the first results of shimmed PD experiments showing that improved implosion symmetry is obtained. The experiments were performed on the OMEGA Laser System in the PD configuration with D_2-gas–filled, shimmed CH shells.

The unablated shell material in a laser-driven implosion behaves much like the payload of a rocket.[10] The final velocity of the unablated shell depends nonlinearly on the initial shell thickness and the intensity of the laser light being used to accelerate the shell through ablation.[10] For polar drive, the intensity varies as a function of both polar angle and time. Optimizing polar drive is accomplished by picking the beam shapes, beam pointing, pulse shapes, and target-shim profile that result in the most spherically shaped implosion, leading to the highest target gain. This is done experimentally and with simulations using a 2-D hydrodynamics code. If it is assumed that lateral mass flow in the imploding shell can be neglected, then the simulations can be performed with a one-dimensional (1-D) hydrocode, provided that the amount of absorbed energy can be accurately predicted. To apply this to polar drive it is

assumed that the average absorbed intensity is solely a function of polar angle. The capsule thickness as a function of polar angle needed to compensate for the angular variation of the average intensity can therefore be determined from a series of 1-D simulations. This is illustrated in Fig. 135.12, where the calculated trajectories of the fuel–shell interface R_{fs} as a function of time for two D_2-filled CH shells with identical inner shell radii (412 μm) and fill pressure (10 atm), but with differing shell thicknesses of 24 and 27 μm, respectively, are shown. The simulations were performed with the 1-D hydrocode *LILAC*[11] for nominal laser conditions of 27 kJ of UV light in a 1-ns square pulse (~1 × 10^{15} W/cm^2 at a radius of 430 μm). The 27-μm shell implodes more slowly than the 24-μm shell. R_{fs} is also shown for an intensity reduced to 80% of the nominal case. This trajectory (dashed line) is nearly identical to that of the 27-μm-thick shell at the nominal intensity.

A series of such simulations were performed to determine the approximate shell thickness as a function of average intensity needed so that R_{fs} was the same as the nominal intensity case at a time close to shell stagnation. Figure 135.13 shows
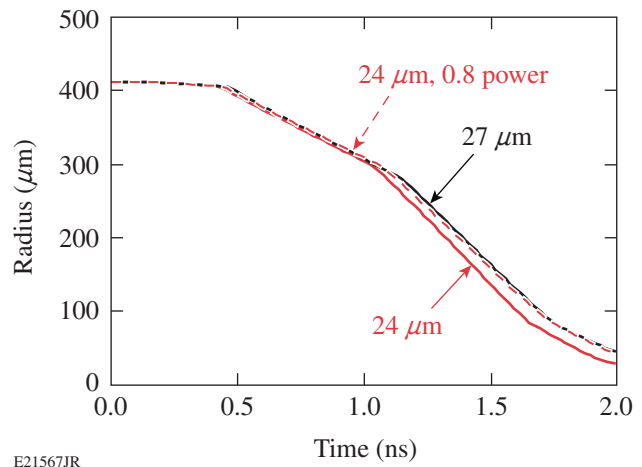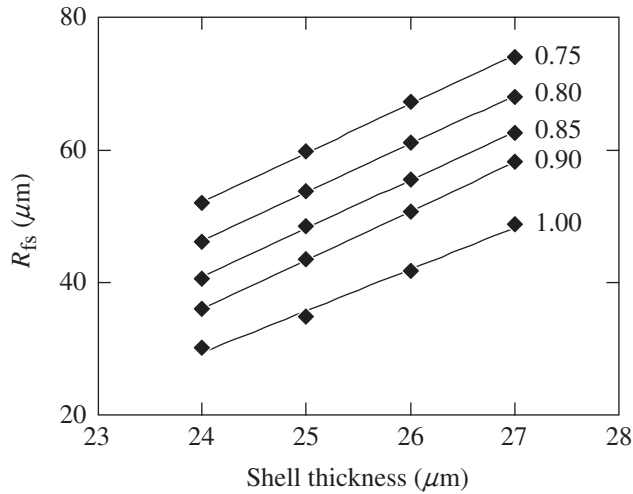

Figure 135.12
Simulated fuel–shell interface R_{fs} trajectory for a 24- and a 27-μm-thick shell at nominal laser conditions of 27 kJ, 1-ns square pulse, and for a 24-μm-thick shell at 0.8 times nominal laser intensity.

E21812JR

Figure 135.13
Simulated values of R_{fs} at $t = 2.0$ ns as a function of shell thickness for cases of 0.75, 0.80, 0.85, 0.90, and 1.0 times nominal laser intensity.

values of R_{fs} at $t = 2.0$ ns, when the fuel–shell interface is close to a minimum, for shell thicknesses Δr from 24 to 27 μm, and intensities I of 0.75 to 1.0 times nominal. A straight line was fit to each set of values of R_{fs} for a given I. The value of shell thickness Δr as a function of intensity that results in an R_{fs} of 49 μm at $t = 2.0$ ns was determined from these fits by linear regression. The resulting equation for Δr in microns as a function of intensity is given by

$$\Delta r = 6.4 + 29.6\,I - 9.0\,I^2, \tag{1}$$

where I is in units of the nominal intensity. The lowest even mode intensity perturbation that could result from PD illumination is the second Legendre mode, i.e. $\ell = 2$. By restricting the perturbation to this first even Legendre mode, the intensity is given by

$$I(\theta) = I_0\left[1 + \frac{i_2}{2}\left(3\cos^2\theta - 1\right)\right]\Big/\left(1 + i_2\right), \tag{2}$$

where I_0 is the intensity at $\theta = 0$ and i_2 is the amplitude of the $\ell = 2$ mode. When Eq. (2) is substituted into Eq. (1), the ideal shell thickness profile is determined for this intensity profile.

The shimmed shells used in the experiments described in this article were manufactured by precision machining at the General Atomics (GA) Target Facility.[12] The ideal target profile was chosen by assuming that the average intensity profile was 10% prolate ($i_2 = +0.1$)—a magnitude and sign likely to result from PD illumination but otherwise an arbitrary choice. To

accomplish this process on a lathe using a single mounting direction, it was decided to avoid machining the shells near the poles (also the rotation axis of the lathe), avoiding errors in alignment introduced by switching the mounting direction of the target from one pole to the other. This leaves a region of constant shell thickness near the poles. Figure 135.14 shows the ideal profile, a modified profile that avoids the need to machine the poles, and an actual measured profile for one GA-machined shell. The modified profile is arrived at from the ideal profile by setting Δr equal to a constant from 0° to 30° and then using $\Delta r = \Delta r(\theta')$, where $\theta' = (\theta - 30°) \times 1.5$ for $30° \leq \theta \leq 90°$. The initial mean shell thickness for this shell was 26.5 μm, so all values of the calculated profiles were shifted by 0.5 μm, and the machining was performed with respect to this thinner profile. The measured profile is close to the modified profile. Machining errors were kept to ~0.5 μm from the desired thickness. Three such targets were used in OMEGA experiments, and the results were compared to targets that were manufactured in an identical fashion at GA but did not undergo machining.
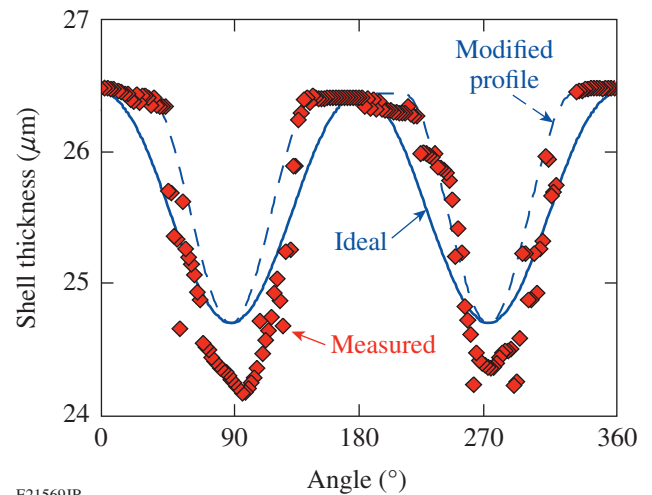
E21569JR

Figure 135.14
Measured shimmed shell thickness as a function of polar angle compared to the ideal profile and modified profile that avoids the need to machine near the poles.

The experiments were performed on OMEGA in the polar-drive configuration, where 40 of the 60 OMEGA beams are used to illuminate the target.[5] The experiments were performed with 14 kJ of UV light (351 nm) using an ~3-ns-duration, triple-picket pulse shape,[7] designed to keep the target on a low adiabat, obtaining a high convergence ratio (CR, the ratio of the initial fuel-shell radius to final fuel-shell radius). CR's of ~19 were calculated for these experiments. The OMEGA laser

beams were smoothed using 0.5-THz–bandwidth smoothing by spectral dispersion (SSD),[13] with polarization smoothing.[14] The beam profiles were shaped using distributed phase plates (DPP's), resulting in a super-Gaussian beam shape given by $I/I_0 = \exp[-(r/r_0)^n]$ with $r_0 = 308$ μm and $n = 3.66$ (Ref. 15). Beam pointing was chosen by using the modified capsule thickness profile as input to a series of *DRACO* 2-D hydrocode simulations[16] with varying beam pointing. Beam offset is used to quantify beam pointing, with the magnitude being the distance from beam center to target center, perpendicular to the beam propagation direction, and with a positive offset meaning toward the equator of the PD axis.[5] The pointing chosen (0-, 120-, and 140-μm offsets for rings 1, 2, and 3, respectively) resulted in the most-symmetric implosion in the simulations. This beam offset case is less than the case previously found for spherically symmetric shells with polar drive described in Marshall *et al.*[6] (90-, 150-, and 150-μm offsets for rings 1, 2, and 3, respectively). The beams were precision pointed to an accuracy of ~8 μm to these ideal offset locations using the method described in Ref. 15.

The time-dependent shapes of the imploding shells were measured with framed x-ray backlighting, using a 6-μm-thick Ti foil illuminated by 8 of the 20 remaining OMEGA beams. The beams were overlapped onto the foil, four on each side, defocussed to a diameter of 0.7 mm. The foil was thin enough (6 μm) to be nearly transparent to the principal Ti-emitting line at 4.75 keV (He$_\alpha$), effectively doubling the backlighter brightness. The backlighter was placed on the opposite side of the target from a high-speed framing camera[17] having four strips, each timed to capture an array of images from 10-μm-diam pinholes, with a magnification of 6, spaced so that the separation in time of each image was 30 ps. The view of the target was 11° from the equator of the polar-drive axis, where the shapes of the observed radiographs were almost the same as at the equator (within ~2% for pure ℓ modes at this angle, see Ref. 5). Absolute frame times were determined from observation of the backlighter onset on the first strip, from the measured strip-to-strip delay, and from the image-to-image time delay on a strip. An absolute time accuracy of ~50 ps was obtained with a frame-to-frame time accuracy of ~15 ps. As described in Ref. 6, the recorded images were corrected for both film sensitivity and backlighter intensity variation as a function of position and are presented as the optical depth of the radiographed plasma as a function of position. Figure 135.15 shows sample radiographs of a spherical shell and two shimmed shells. The two shimmed shell cases are shown to demonstrate repeatability. The times are from the end of the laser pulse (~3.0 ns) to a time just before shell stagnation (~3.5 ns). As can be seen from the images, the
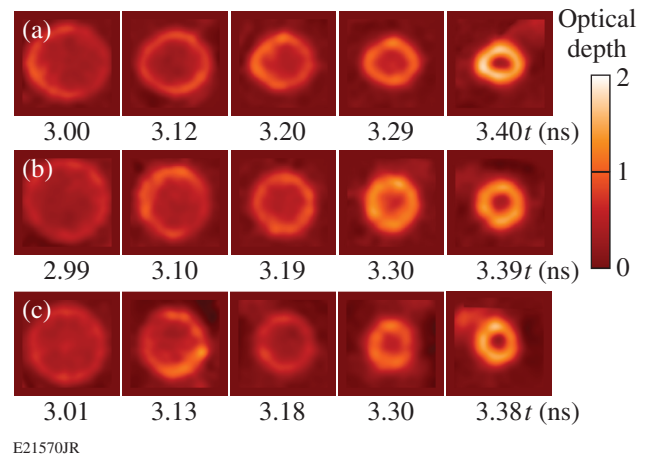

Figure 135.15
Sample radiographs of 500×500-μm regions centered on the imploding plasma shell for (a) a spherical shell and [(b,c)] two shimmed shells, all imploded with the same beam-pointing condition.

shimmed shells implode with a more spherical shape for this beam pointing.

The shapes of the imploding plasmas are quantified by fitting the positions of the observed peak optical depth as a function of angle to the PD axis to a Legendre polynomial. The shape of the plasma is well measured at times corresponding to CR's of ~7 or less. At later times (higher CR's) self-emission obscures the backlighter. Figure 135.16 shows sample fits to both measured and simulated radiographs for a spherical shell [Figs. 135.16(a) and 135.16(b)] and a shimmed shell [Figs. 135.16(c) and 135.16(d)], both at the latest time measured. The simulated radiographs are determined from *DRACO* simulations. The shell shape is included in the shimmed-target simulations by a Legendre-mode decomposition up to mode 10 of the measured shell thickness. The simulations were post-processed by the code *Spect3D*,[18] which takes into account radiation transport, spatial blurring (~15 μm), and integration over the frame time (30 ps). Mode amplitudes (normalized to the average radius) of the fits at all measured times for the two most significant modes $\ell = 2$ and $\ell = 4$ modes (i.e., a_2 and a_4) are shown for both the spherical shell [Fig. 135.16(e)] and the shimmed shell [Fig. 135.16(f)]. The spherical shell develops a significant negative a_2 (~ –15%) late in time indicative of an oblate shape. The $\ell = 4$ mode is significant and positive (~ +5%). The shimmed shell target obtains a more nearly spherical shape with a_2 and a_4 being $\lesssim$2% to 3% for all times measured. The amplitudes determined from the simulations are close to those observed. For the spherical target case [Fig. 135.16(e)], both the sign and magnitude of a_2 from the simulation match the observations, whereas the magnitude of a_4 is overpredicted

compared to observations. This is also true for the shimmed target [Fig. 135.16(f)], where both observations and simulations show a small a_2 but the simulation predicts a positive a_4 of ~5% to 10%. This may indicate a difference in the actual and predicted distribution of material in the plasma at that time. Nevertheless, the shimmed target obtains the most symmetric shape in both experiment and simulation for these cases.
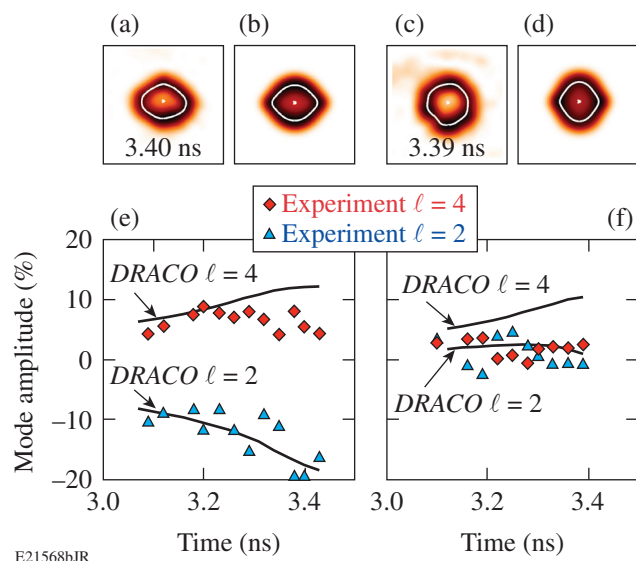

Figure 135.16
Fits to (a) measured and (b) simulated radiographs for a spherical shell, and fits to (c) measured and (d) simulated radiographs for a shimmed shell, at the indicated times. All regions are $500 \times 500\ \mu$m. The $\ell = 2$ and $\ell = 4$ components of the fits to the measured radiographs are shown in (e) and (f) along with values determined from the simulations.

These results show that a shimmed target can improve the symmetry of a polar-driven imploding shell but taken alone do not demonstrate the benefit of using shimmed shells over just beam repointing to control this shape. The combined benefit is more aptly demonstrated by comparing the symmetry of spherical targets imploded by polar-drive beam pointing, chosen to give the best low-mode symmetry ($a_2 \approx 0$), with the shimmed target result of Fig. 135.16. Figure 135.17 shows the modal fit to a radiograph of a spherical shell imploded with a beam repointing of 90-, 133-, and 133-μm offsets for Rings 1, 2, and 3, respectively, (all other conditions the same) compared to the shimmed shell with the beam pointing given above at ~100 ps before stagnation (3.4 ns) and with nearly equal average radii (~70 μm). Note that for the spherical target $a_2 \approx 0$, while $a_4 \approx +16\%$. The plasma exhibits a "diamond-like" shape from this significant positive $\ell = 4$ mode. In contrast, a_2 and a_4 are both small (≲2%) for the shimmed target, demonstrating the
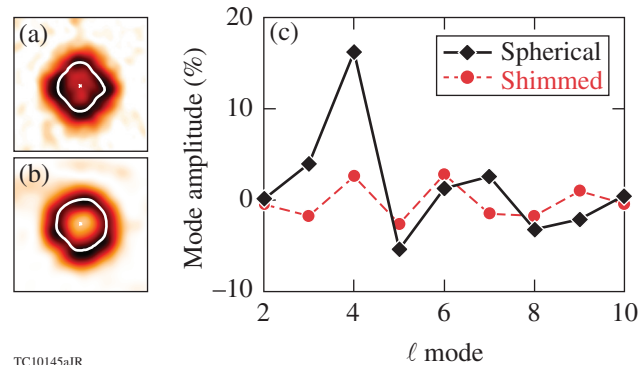
Figure 135.17
Fits to radiographs of (a) a spherical target with optimum pointing for the spherical target (see text), and (b) a shimmed target with the pointing used for the shimmed target experiments (see text). Both radiographs are of 400×400-μm regions just before stagnation of the shell. (c) Mode amplitudes from Legendre polynomial fits to these shapes

combined benefit of beam repointing and target shimming in controlling the shape of the polar-driven implosion.

As demonstrated by these experiments, target shimming can increase the low-mode symmetry over beam repointing alone. Given the need to control the shape of PD implosions on the NIF, and the anticipated benefit of shimming to increase the ignition margin, these results indicate that further research into methods to shape the DT encapsulating shell, and/or the DT layer itself should be undertaken. Indirectly driven implosions may also benefit from using a shimmed target, emphasizing the importance of this method.

ACKNOWLEDGMENT

REFERENCES
1. S. Skupsky, J. A. Marozas, R. S. Craxton, R. Betti, T. J. B. Collins, J. A. Delettrez, V. N. Goncharov, P. W. McKenty, P. B. Radha, T. R. Boehly, J. P. Knauer, F. J. Marshall, D. R. Harding, J. D. Kilkenny, D. D. Meyerhofer, T. C. Sangster, and R. L. McCrory, Phys. Plasmas **11**, 2763 (2004).

2. G. H. Miller, E. I. Moses, and C. R. Wuest, Opt. Eng. **43**, 2841 (2004).

3. T. R. Boehly, D. L. Brown, R. S. Craxton, R. L. Keck, J. P. Knauer, J. H. Kelly, T. J. Kessler, S. A. Kumpan, S. J. Loucks, S. A. Letzring, F. J. Marshall, R. L. McCrory, S. F. B. Morse, W. Seka, J. M. Soures, and C. P. Verdon, Opt. Commun. **133**, 495 (1997).

4. R. S. Craxton, F. J. Marshall, M. J. Bonino, R. Epstein, P. W. McKenty, S. Skupsky, J. A. Delettrez, I. V. Igumenshchev, D. W. Jacobs-Perkins, J. P. Knauer, J. A. Marozas, P. B. Radha, and W. Seka, Phys. Plasmas **12**, 056304 (2005).

5. F. J. Marshall, R. S. Craxton, M. J. Bonino, R. Epstein, V. Yu. Glebov, D. Jacobs-Perkins, J. P. Knauer, J. A. Marozas, P. W. McKenty, S. G. Noyes, P. B. Radha, W. Seka, S. Skupsky, and V. A. Smalyuk, J. Phys. IV France **133**, 153 (2006).

6. F. J. Marshall, P. W. McKenty, J. A. Delettrez, R. Epstein, J. P. Knauer, V. A. Smalyuk, J. A. Frenje, C. K. Li, R. D. Petrasso, F. H. Séguin, and R. C. Mancini, Phys. Rev. Lett. **102**, 185004 (2009).

7. P. B. Radha, J. A. Marozas, F. J. Marshall, A. Shvydky, T. J. B. Collins, V. N. Goncharov, R. L. McCrory, P. W. McKenty, D. D. Meyerhofer, T. C. Sangster, and S. Skupsky, Phys. Plasmas **19**, 082704 (2012).

8. J. A. Marozas, F. J. Marshall, R. S. Craxton, I. V. Igumenshchev, S. Skupsky, M. J. Bonino, T. J. B. Collins, R. Epstein, V. Yu. Glebov, D. Jacobs-Perkins, J. P. Knauer, R. L. McCrory, P. W. McKenty, D. D. Meyerhofer, S. G. Noyes, P. B. Radha, T. C. Sangster, W. Seka, and V. A. Smalyuk, Phys. Plasmas **13**, 056311 (2006).

9. T. J. B. Collins, J. A. Marozas, K. S. Anderson, R. Betti, R. S. Craxton, J. A. Delettrez, V. N. Goncharov, D. R. Harding, F. J. Marshall, R. L. McCrory, D. D. Meyerhofer, P. W. McKenty, P. B. Radha, A. Shvydky, S. Skupsky, and J. D. Zuegel, Phys. Plasmas **19**, 056308 (2012).

10. J. D. Lindl *et al.*, Phys. Plasmas **11**, 339 (2004).

11. J. Delettrez, R. Epstein, M. C. Richardson, P. A. Jaanimagi, and B. L. Henke, Phys. Rev. A **36**, 3926 (1987).

12. General Atomics, San Diego, CA 92121-1122.

13. S. Skupsky, R. W. Short, T. Kessler, R. S. Craxton, S. Letzring, and J. M. Soures, J. Appl. Phys. **66**, 3456 (1989).

14. T. R. Boehly, V. A. Smalyuk, D. D. Meyerhofer, J. P. Knauer, D. K. Bradley, R. S. Craxton, M. J. Guardalben, S. Skupsky, and T. J. Kessler, J. Appl. Phys. **85**, 3444 (1999).

15. R. A. Forties and F. J. Marshall, Rev. Sci. Instrum. **76**, 073505 (2005).

16. P. B. Radha, V. N. Goncharov, T. J. B. Collins, J. A. Delettrez, Y. Elbaz, V. Yu. Glebov, R. L. Keck, D. E. Keller, J. P. Knauer, J. A. Marozas, F. J. Marshall, P. W. McKenty, D. D. Meyerhofer, S. P. Regan, T. C. Sangster, D. Shvarts, S. Skupsky, Y. Srebro, R. P. J. Town, and C. Stoeckl, Phys. Plasmas **12**, 032702 (2005).

17. D. K. Bradley *et al.*, Rev. Sci. Instrum. **66**, 716 (1995).

18. J. J. MacFarlane *et al.*, High Energy Density Phys. **3**, 181 (2007).

Localized Time-Resolved Electron-Temperature Measurements Indicate Nonuniformly Driven Two-Plasmon–Decay Instability in Direct-Drive Implosions

The two-plasmon–decay (TPD) instability is the decay of an incident laser photon into two plasmons[1,2] that can generate energetic electrons, thereby preheating direct-drive inertial confinement fusion (ICF)[3,4] implosions and degrading their performance. The phase-matching conditions for this instability restrict it to electron densities of $n_e \leq n_c/4$, where n_c is the critical density at which the plasma frequency equals the laser frequency. This instability is generally accompanied by optical emission near $\omega_0/2$ and $3\omega_0/2$, where ω_0 is the laser frequency. Above the TPD threshold, energetic electron production is frequently observed as evidenced by hard x-ray emission.

Various aspects of the half-harmonic emission from laser-produced plasmas were analyzed in 1985 (Ref. 5). In particular, a sharp red-shifted spectral feature was identified as a result of the absolute TPD instability[6] in inhomogeneous plasmas[6–9] that occurs very close to the $n_c/4$ density. This feature is most likely caused by inverse resonance absorption that can efficiently convert the low-frequency TPD plasmons to photons. Since the frequencies of these plasmons depend only on the local electron temperature, this spectral feature also provides a powerful electron-temperature diagnostic[5] in close proximity of the $n_c/4$ surface. Absorption of this feature on the way out of the plasma is significant (80% to 90%), but its intensity is generally sufficient to make it readily observable.

The TPD instability was originally thought to involve only a single laser beam. In 2003, planar-interaction experiments and spherical implosion experiments[10] at LLE demonstrated that the TPD instability was a multibeam instability.[11] At that time there was no theory to explain the multibeam interaction, energetic electron generation, or different onsets for the half-integer harmonics and hard x-ray emission. The spectral extent of the $\omega/2$ and $3\omega/2$ emission indicated that this instability extended well into the convective TPD regime[12–14] to densities limited by Landau damping near $n_e \leq n_c/5$ (Ref. 11), where $k_p \lambda_{De} \sim 0.25$ (k_p and λ_{De} are the longer of the two TPD plasmon $\underline{k}$-vectors and the Debye length). Over the past decade, significant progress has been made on multibeam TPD theories and simulations using kinetic particle-in-cell (PIC),[14–16] reduced PIC (RPIC),[17–20] and fluid-type Zakharov simulations.[20–23] These simulations have shown that both absolute and convective TPD instabilities can be driven by multiple beams and that beam configurations (number of beams, angles of incidence, and polarization) determine the outcome. They also showed that within ~10 ps or less, the TPD instability is dominated by nonlinear effects and saturation. This implies that the linear regime of this instability is not observable experimentally.

Recent work at LLE showed the effect of beam configurations, polarization, threshold, and intensity scaling of hot-electron production resulting from TPD[24,25] based on experiments and linear gain calculations.

In this article we present the first precision (~5%), time-resolved electron-temperature measurements in different areas of an imploding target and located in density space between $0.24 < n_e/n_c < 0.25$. These measurements indicate that close to the TPD threshold, the measured temperatures agree well with those predicted by hydrodynamic simulations, while above the threshold, they typically exceed the simulations by up to 20%. The exact amount of the excess temperature depends on the number of overlapping beams that drive the instability in any particular area.

Experiments were carried out on LLE's 60-beam OMEGA Laser System[26] using spherical targets. Each beam illuminates the entire hemisphere of the target using distributed phase plates (DPP's)[27] and smoothing by spectral dispersion (SSD).[28] Time-resolved $\omega/2$ spectra were recorded in three locations: one through one of the beam ports (backscattering) and two centered within a hex or pent port (see Fig. 135.18). The signals from beam and hex ports were collected near the target chamber and fiber optically relayed to a time-multiplexed, 1/3-m spectrometer. The signal from the pent port was optically relayed to a similar spectrometer. Both spectrometers were proximity coupled to ROSS streak cameras.[29] Typical spectral and temporal resolutions were ~1 nm and ~100 ps, respectively. All streak records were routinely corrected for geometric and sweep-speed nonlinearities to near 1% residual
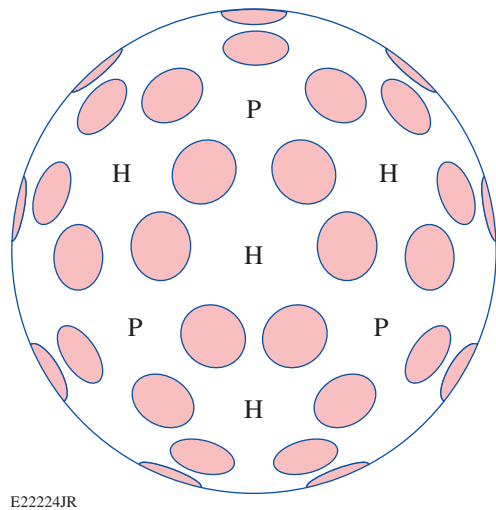
Figure 135.18
Schematic of the OMEGA target chamber with beam ports (shaded) and the locations of hex (H) and pent (P) ports. $\omega/2$ spectra were recorded through one of the beam ports and centered on one of the H and P ports.

nonlinearity. The two multiplexed spectra viewed the entire target sphere, while the spectra recorded in the pent location viewed an ~50-μm × 50-μm area on the target sphere.

Half-harmonic images were recorded on a charge-coupled–device (CCD) camera at the center of another hex port. Colored glass and an interference filter at the camera input integrated over either the entire $\omega/2$ spectrum (680 nm and 720 nm) or

only the blue part of the spectrum (680 nm to 700 nm). (The central $\omega_0/2$ wavelength lies at 702 nm.)

Representative $\omega/2$ spectra recorded at the center of the pent port are shown in Fig. 135.19 for two viewing directions: one viewing an imploding target along the target normal [Fig. 135.19(a)]; the other one displaced by ~100 μm and inclined by ~10° relative to the target normal [Fig. 135.19(d)]. The sharp red-shifted spectral feature [Fig. 135.19(a)] is the same as that previously identified with the absolute TPD insta-bility.[5,6] This spectral feature results from plasmon-to-photon conversion[30] via inverse resonance absorption of the lower-frequency TPD plasmons whose $\underline{k}$-vectors nearly vanish. The multibeam nature of the instability is inferred from threshold calculations. The absolute TPD threshold[6,23] can be defined as $\eta = 1$, where $\eta = I_{14} L_{n,\mu m} / (233 \, T_{e,keV})$ and I_{14}, L_n, and T_e are the intensity, density scale length, and electron temperature at $n_c/4$ in units of 10^{14} W/cm^2, μm, and keV, respectively. For the multibeam geometries prevalent on OMEGA, I_{14} represents the sum of all the beam intensities that can contribute to the absolute TPD instability at the point of interest.[23] For the shots shown in Fig. 135.19, the single-beam peak intensity toward the end of the laser pulse was $I_{14} \sim 2.35$, $L_n \sim 100$ μm, and $T_e \sim 1.8$ keV, resulting in $\eta \sim 0.2$, i.e., far below the absolute TPD threshold. Using hydrodynamic predictions for these quantities where I_{14} is the total intensity at quarter critical summed over all angles of incidence, we note that η shown in Fig. 135.19(c) is close to 1, i.e., the threshold. In fact, this average intensity
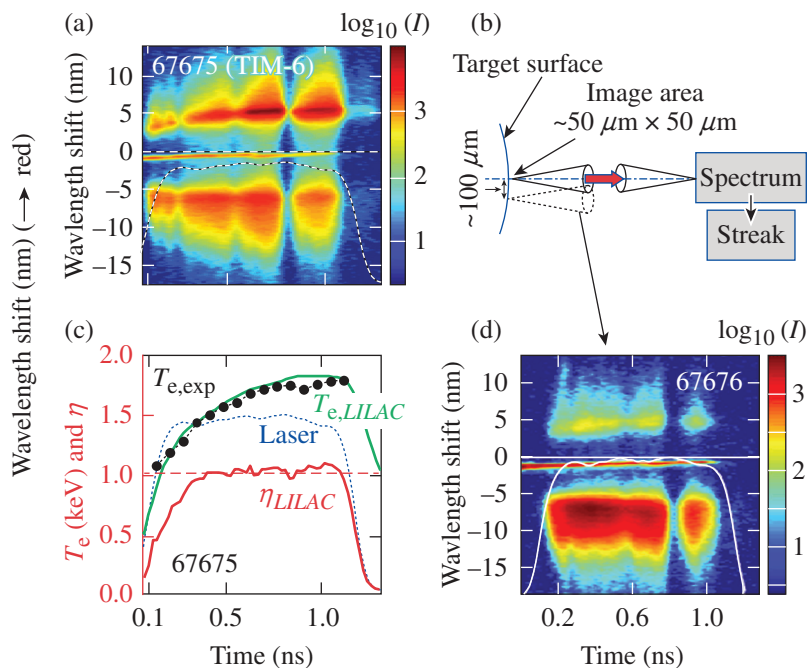
Figure 135.19
Time-resolved $\omega/2$ spectra viewing a small area on the target surface. (a) Spectrum taken along the target normal; (b) schematic setup for time-resolved $\omega/2$ spectroscopy; (c) measured electron temperatures (black dots), LILAC predictions (green line), laser power (blue dashed line), and threshold parameter η obtained from LILAC (red line); (d) equivalent $\omega/2$ spectrum taken ~10° off the target normal.

E22225JR

is an overestimate of the relevant overlapped intensity that can drive the TPD instability, particularly if polarization smoothing is included, which presumably halves the TPD drive intensity. The discrepancy may be related to the speckle nature of the focal spot for which peak intensities can easily be 3× to 5× larger. The influence of speckles on driving the TPD instability is presently being investigated using the Zakharov simulations.

Figure 135.19(d) shows the off-axis $\omega/2$ spectrum, which is dominated by the broad blue-shifted spectral feature corresponding to TPD decays well below $n_c/4$. These features cannot be generated by mode conversion but require Thomson scattering using one of the irradiation beams as the Thomson probe. For the OMEGA geometry, the phase-matching conditions for generating $\omega/2$ radiation via Thomson scattering are not satisfied for Thomson scattering off primary TPD plasmons using any of the OMEGA beams as the Thomson probe. These conditions can be satisfied, however, if the TPD plasma waves roughly fill k space up to the Landau cutoff density as predicted in the nonlinear evolution of the instability by PIC,[16] RPIC,[18,31] and Zakharov[20,32,33] simulations. In principle, inverse parametric decay could generate some of these spectral features. This process is not very likely since it is a higher-order process involving TPD plasmons and ion waves with appropriate $\underline{k}$-vectors.

The broad $\omega/2$ spectral features do not reveal the generation processes but indicate the range of densities involved in the TPD instability. The two TPD plasmons have frequencies $\omega_{1,2} = \omega_0/2 \pm \Delta\omega$. Along the maximum TPD growth-rate curve[5,6,11] $\Delta\omega/\omega_0 = 4.4 \times 10^{-3} \kappa T_{e,keV}$, where $\kappa = \mathbf{k}_1 \cdot \mathbf{k}_0 / k_0^2 - 1/2$ (Ref. 5), and k_0 and k_1 are the $\underline{k}$-vectors of the incident photons and the larger-k plasmon of the two TPD waves. The absolute TPD instability near $n_c/4$ has the lowest single and multibeam thresholds,[6,23,33] corresponding to $\kappa \approx 0.5$ and $T_{e,keV} \approx \Delta\lambda_{nm}/3.1$ for $\lambda_L = 351$ nm. The wavelength shift $\Delta\lambda_{nm}$ of the sharp red-shifted spectra in Fig. 135.19, therefore, indicates an electron temperature at $n_c/4$ of $T_e \approx 1.66$ keV, in good agreement with 1-D hydrodynamic *LILAC*[34] predictions [green line in Fig. 135.19(c)]. Near the Landau cutoff, the frequency shifts are 2× to 3× larger but are of limited diagnostic value since they depend sensitively on the wave vectors probed.

Images of the $\omega/2$ emission provide significant information regarding localization of the TPD instability (Fig. 135.20). Figure 135.20(a) was filtered for the entire $\omega/2$ spectrum (680 nm to 740 nm) for an imploding target at $I_{max} \sim 10^{15}$ W/cm^2, while in Fig. 135.20(b) only the blue $\omega/2$ component was recorded.
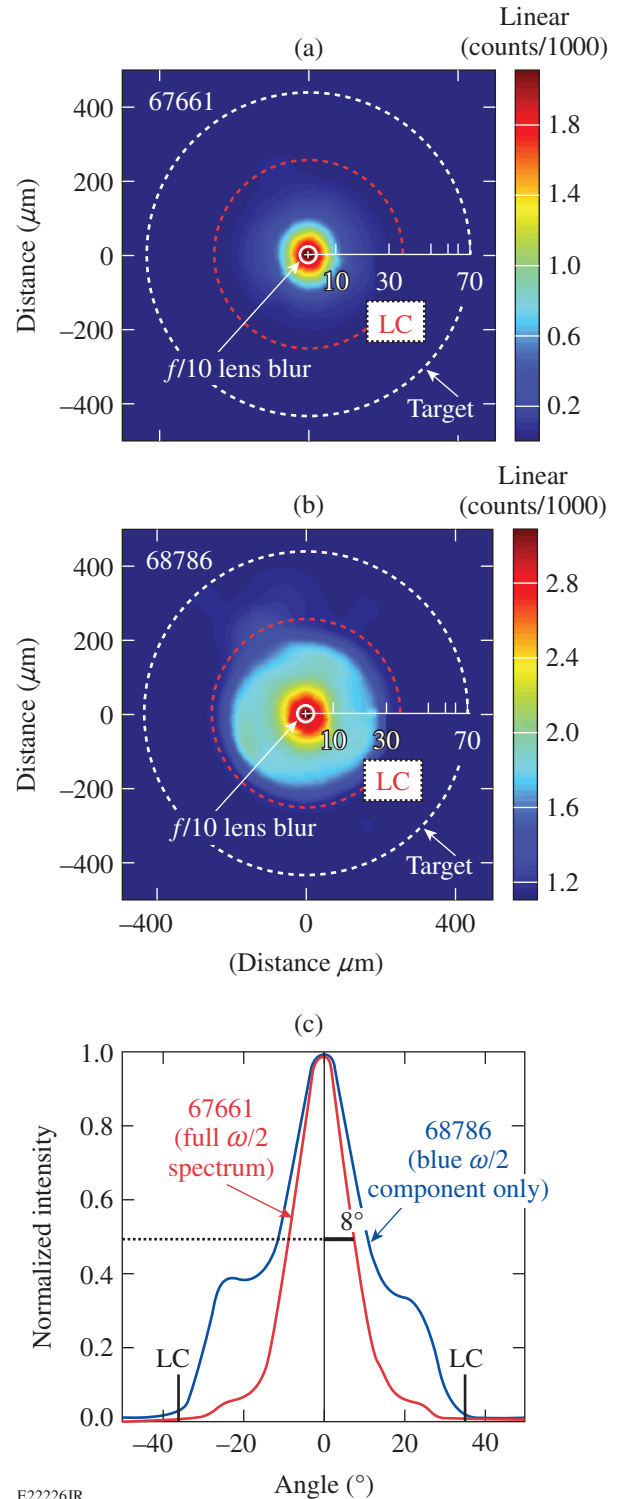

Figure 135.20
The $\omega/2$ images taken through a hex port (surrounded by six beams). (a) Image of an imploding target for 680 nm $< \lambda <$ 740 nm; (b) same as in (a) but 680 nm $< \lambda <$ 700 nm; (c) cross-sectional lineouts through the center of the target for (a) and (b). LC: Landau cutoff.

E22226JR

A scale is superposed in Figs. 135.20(a) and 135.20(b) translating the spatial information in the images into emission angles in degrees. Figure 135.20(c) shows two lineouts through the centers of Figs. 135.20(a) and 135.20(b). Figure 135.20(a) is dominated by the sharp red feature that originates very near its critical density. This emission is guided along the density gradient because of the conservation of the wave vector perpendicular to the density gradient in the near-planar density profile. This also explains the narrow emission cone angle in Fig. 135.20(c), which is ~6° after correction for the $f/10$ imaging optics. Assuming planar geometry (valid considering the dimensions and angles involved relative to the curvature of the $n_c/4$ surface), this narrow cone angle can be used to estimate the maximum density from which the sharp red feature may be emitted. This maximum density is $n_e/n_c \approx 0.247$ and includes the density region for the absolute instability,[6] $0.247 < n_e/n_c \leq 0.25$, depending on T_e.

The $\omega/2$ image in Fig. 135.20(b) is consistent with the spectra shown in Fig. 135.19. Since the sharp red feature is not recorded, this image sees only emission from lower densities (larger $\Delta\lambda$) corresponding to larger emission angles. If this source were isotropic over the entire quarter-critical surface, this image intensity would drop off at the polar angle $\theta_{LC} \sim$ 37°, determined by refraction of $\omega/2$ light generated at the Landau cutoff. The location of the Landau cutoff is indicated in Fig. 135.20 by LC and the red dashed circles. There is only scant emission at or beyond the Landau cutoff consistent with past Thomson-scattering results.[11] A halo of blue $\omega/2$ emission extends to the Landau cutoff with three areas of increased emission near the 12, 5, and 7 o'clock positions. The former is likely caused by the six beams surrounding the hex port, while the

latter correspond to the positions of the three neighboring pent ports (Fig. 135.18) located at $\theta \sim 37.5°$ or right at the Landau cutoff. (The three neighboring hex ports are located 4° farther out and emission from these port locations is not identifiable in these images.) The angular resolution of these images is severely limited by refraction and the large angle emission of the broad $\omega/2$ features. It is therefore impossible to resolve individual beams separated by ~23°.

The relatively narrow central spike in Fig. 135.20(b) (~11° half-cone angle) is consistent with a small TPD interaction area centered on the hex ports. Analogous arguments hold for the pent ports where the thresholds are ~20% higher than in the hex ports (five versus six beams as primary contributors to the instability). In the 60 beam-port locations, four beams can effectively drive the absolute TPD instability, albeit at another 20% increased threshold intensity. The interaction area estimates are very rough since they depend on the nonlinear TPD plasma wave spectrum and the possible experimental Thomson-scattering scenarios on OMEGA.

The onset of $\omega/2$ emission in Fig. 135.21 is consistent with the TPD thresholds[6] if the intensity includes the total number of overlapping beams that can drive the absolute instability at a particular location. At the center of a hex port, six beams overlap but their intensities are reduced by absorption (~10%) on the way to $n_c/4$ and the intensity profile (~10%) for a total intensity of ~4.8× the single-beam peak intensity. Near the center of each beam, four beams can drive the TPD instability (Fig. 135.18). After accounting for absorption and beam profile, the total intensity is ~3.4× the single-beam intensity at this location. (Higher-angle beams contribute insignificantly

(a) $\log_{10}(I)$ (b) $\log_{10}(I)$
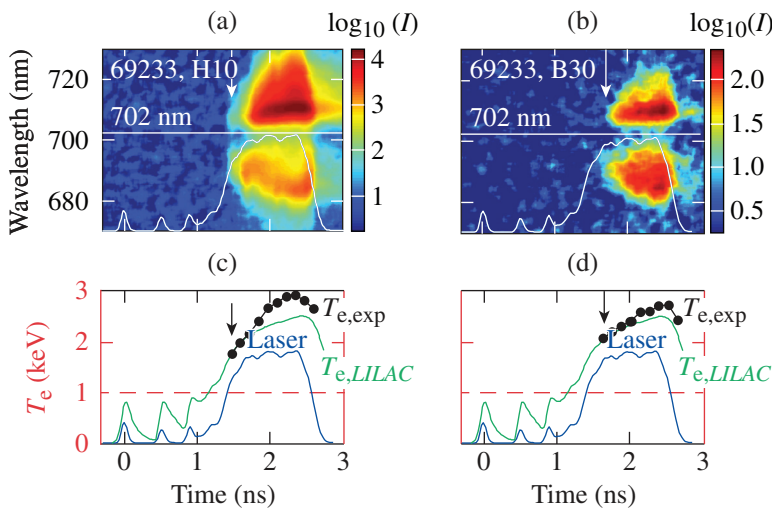
Figure 135.21
The $\omega/2$ spectra taken for an imploding room-temperature target at 9.3×10^{14} W/cm^2 through (a) a beam port and (b) a hex port. The laser pulse shape is shown in each panel. The sharp red-shifted features in (a) and (b) were used to measure T_e in (c) and (d). Random error bars are equal to the symbol sizes. Hydrodynamic predictions for T_e are shown in green. Arrows indicate the onset of $\omega/2$ emission and estimated TPD thresholds.

E22227JR

because of the intensity profiles.) Different onset times for the TPD instability (white and black arrows in Fig. 135.21) are evident in the spectra taken at the beam port and hex port locations. The onsets the T_e increase and corresponding maximum electron temperatures [Fig. 135.21(c)] in the two locations reflect the different absolute TPD thresholds $I_{th} \sim IL_n/T_e$, where I is the overlapped intensity and L_n is density gradient length. Both I and L_n increase with time past $t = 1.5$ ns in Fig. 135.21. The maximum temperatures vary over the quarter-critical surface and locally exceed the average temperatures predicted by hydrodynamic simulations by 10% to 20%. (At the onset of the spectra, the measured temperatures agree well with the hydrodynamic simulations.) The measured temperature excursions beyond the hydrodynamic predictions entail $n_c/4$ surface perturbations caused by pressure uniformity in the corona. Such perturbations have been reproduced in two-dimensional (2-D) hydrodynamic simulations.

In conclusion, spatially and temporally resolved half-harmonic spectra and images of laser-driven implosions show clear evidence for the multibeam nature of the TPD instability, its rapid nonlinear evolution, and its spatially limited extent. The thresholds correspond to the multibeam-driven absolute instability and are identified via a sharp red-shifted spectral feature. These thresholds agree with published absolute thresholds after adjusting the intensity for multibeam effects. The broad $\omega/2$ spectral features that develop essentially simultaneously with the sharp red-shifted feature are identified as the nonlinear phase of the TPD instability that extends rapidly all the way to the Landau cutoff covering the conventionally called convective regime. There is no experimental evidence for a linear convective regime. These results are in good agreement with recent fluid and kinetic TPD simulations. Localized T_e measurements and $\omega/2$ images point toward localized temperature islands near $n_c/4$, where temperatures exceed the average by 10% to 20% and entail localized surface perturbations.

REFERENCES

1. M. V. Goldman, Ann. Phys. **38**, 95 (1966).

2. M. V. Goldman, Ann. Phys. **38**, 117 (1966).

3. J. D. Lindl, *Inertial Confinement Fusion: The Quest for Ignition and Energy Gain Using Indirect Drive* (Springer-Verlag, New York, 1998).

4. D. W. Phillion *et al.*, Phys. Rev. Lett. **49**, 1405 (1982).

5. W. Seka, B. B. Afeyan, R. Boni, L. M. Goldman, R. W. Short, K. Tanaka, and T. W. Johnston, Phys. Fluids **28**, 2570 (1985).

6. A. Simon, R. W. Short, E. A. Williams, and T. Dewandre, Phys. Fluids **26**, 3107 (1983).

7. C. S. Liu, M. N. Rosenbluth, and R. B. White, Phys. Rev. Lett. **31**, 697 (1973).

8. M. N. Rosenbluth, R. B. White, and C. S. Liu, Phys. Rev. Lett. **31**, 1190 (1973).

9. B. B. Afeyan and E. A. Williams, Phys. Rev. Lett. **75**, 4218 (1995).

10. C. Stoeckl, R. E. Bahr, B. Yaakobi, W. Seka, S. P. Regan, R. S. Craxton, J. A. Delettrez, R. W. Short, J. Myatt, A. V. Maximov, and H. Baldis, Phys. Rev. Lett. **90**, 235002 (2003).

11. W. Seka, D. H. Edgell, J. F. Myatt, A. V. Maximov, R. W. Short, V. N. Goncharov, and H. A. Baldis, Phys. Plasmas **16**, 052701 (2009).

12. M. N. Rosenbluth, Phys. Rev. Lett. **29**, 565 (1972).

13. L. V. Powers and R. L. Berger, Phys. Fluids **28**, 2419 (1985).

14. R. Yan, A. V. Maximov, and C. Ren, Phys. Plasmas **17**, 052701 (2010).

15. R. Yan, A. V. Maximov, C. Ren, and F. S. Tsung, Phys. Rev. Lett. **103**, 175002 (2009).

16. R. Yan, C. Ren, J. Li, A. V. Maximov, W. B. Mori, Z. M. Sheng, and F. S. Tsung, Phys. Rev. Lett. **108**, 175002 (2012).

17. H. X. Vu, D. F. DuBois, D. A. Russell, and J. F. Myatt, Phys. Plasmas **17**, 072701 (2010).

18. H. X. Vu, D. F. DuBois, J. F. Myatt, and D. A. Russell, Phys. Plasmas **19**, 102703 (2012).

19. H. X. Vu, D. F. DuBois, D. A. Russell, and J. F. Myatt, Phys. Plasmas **19**, 102708 (2012).

20. J. F. Myatt, J. Zhang, J. A. Delettrez, A. V. Maximov, R. W. Short, W. Seka, D. H. Edgell, D. F. DuBois, D. A. Russell, and H. X. Vu, Phys. Plasmas **19**, 022707 (2012).

21. D. A. Russell and D. F. DuBois, Phys. Rev. Lett. **86**, 428 (2001).

22. J. F. Myatt, H. X. Vu, D. F. DuBois, D. A. Russell, J. Zhang, R. W. Short, and A. V. Maximov, Phys. Plasmas **20**, 052705 (2013).

23. J. Zhang, J. F. Myatt, R. W. Short, A. V. Maximov, H. X. Vu, D. F. DuBois, and D. A. Russell, "Multibeam Two-Plasmon Decay from Linear Threshold to Nonlinear Saturations," to be submitted to Physical Review Letters.

24. D. T. Michel, A. V. Maximov, R. W. Short, J. A. Delettrez, D. Edgell, S. X. Hu, I. V. Igumenshchev, J. F. Myatt, A. A. Solodov, C. Stoeckl, B. Yaakobi, and D. H. Froula, Phys. Plasmas **20**, 055703 (2013).

25. D. T. Michel, A. V. Maximov, R. W. Short, S. X. Hu, J. F. Myatt, W. Seka, A. A. Solodov, B. Yaakobi, and D. H. Froula, Phys. Rev. Lett. **109**, 155007 (2012).

26. T. R. Boehly, D. L. Brown, R. S. Craxton, R. L. Keck, J. P. Knauer, J. H. Kelly, T. J. Kessler, S. A. Kumpan, S. J. Loucks, S. A. Letzring, F. J. Marshall, R. L. McCrory, S. F. B. Morse, W. Seka, J. M. Soures, and C. P. Verdon, Opt. Commun. **133**, 495 (1997).

27. Y. Lin, T. J. Kessler, and G. N. Lawrence, Opt. Lett. **20**, 764 (1995).

28. S. Skupsky, R. W. Short, T. Kessler, R. S. Craxton, S. Letzring, and J. M. Soures, J. Appl. Phys. **66**, 3456 (1989).

29. W. R. Donaldson, R. Boni, R. L. Keck, and P. A. Jaanimagi, Rev. Sci. Instrum. **73**, 2606 (2002).

30. R. E. Turner *et al.*, Phys. Fluids **27**, 511 (1984).

31. H. X. Vu, D. F. DuBois, J. F. Myatt, and D. A. Russell, presented at the 41st Annual Anomalous Absorption Conference, San Diego, CA, 19–24 June 2011.

32. J. F. Myatt, J. Zhang, A. V. Maximov, R. W. Short, D. F. DuBois, D. A. Russell, and H. X. Vu, Bull. Am. Phys. Soc. **56**, 328 (2011).

33. J. Zhang, J. F. Myatt, A. V. Maximov, R. W. Short, D. F. DuBois, D. A. Russell, and H. X. Vu, Bull. Am. Phys. Soc. **57**, 299 (2012).

34. J. Delettrez, R. Epstein, M. C. Richardson, P. A. Jaanimagi, and B. L. Henke, Phys. Rev. A **36**, 3926 (1987).

Measurements of the Divergence of Fast Electrons in Laser-Irradiated Spherical Targets

Fast electrons produced by the two-plasmon–decay (TPD) instability[1–4] in direct-drive fusion can deposit their energy into the nuclear fuel (preheat), leading to a reduction in the maximum compression and target performance.[5–8] Typical direct-drive–ignition designs can withstand of the order of ~0.1% of the laser energy converted to preheat[6] before significant degradation occurs. In recent experiments (both planar[9,10] and spherical[11,12]), a Mo layer was used to determine the energy in fast electrons as a fraction of laser energy, using the Mo–K_α line. The energy in fast electrons was found to increase rapidly with laser intensity. At the maximum laser irradiance for spherical targets of ~1.1×10^{15} W/cm^2, the energy in fast electrons was ~1% of the laser energy. This is about 10× higher than the maximum that can be tolerated for ignition, and if effectively coupled to the fuel, the effects would be prohibitive. The fast-electron divergence established in this experiment, however, limits the fraction of fast electrons that contribute to preheat. The electrons in the recent experiments were nearly completely absorbed by the Mo layer, providing a measure of the total energy in fast electrons. However, in typical cryogenic direct-drive experiments,[13] the fraction of the fast-electron energy deposited as preheat can be significantly less; only preheat of the compressed fuel shell can be detrimental to target performance. Fast electrons are generated near the end of the laser pulse[4] when the density scale length reaches a maximum. At that time the compressed fuel shell has converged to about half the original target size.[13] Fast electrons produced by TPD are generated near the quarter-critical density layer, and if they have a wide angular divergence, only ~1/4 of the fast electrons will be intercepted by the compressed fuel.

Knowledge of the fast-electron divergence is crucial in assessing their effect on direct-drive experiments and ignition designs. The total energy in fast electrons (as well as the fast-electron temperature) in fusion target implosions is studied using the emitted hard x rays (HXR's).[7,14–16] Without a knowledge of the divergence, the preheat in the compressed fuel cannot readily be determined. This is because the relationship between the measured HXR and the number of fast electrons depends on the atomic number Z; therefore (in D$_2$- or DT-filled CH shells) this relationship depends on the partition of the HXR produced by the nuclear fuel and by the outer CH layer. This partition depends on the divergence of fast electrons: the higher the divergence, the larger the fraction of the HXR coming from the CH (since more electrons miss the central fuel shell and travel within the CH). Therefore, an understanding of the fast-electron divergence in laser-fusion experiments is critical for (a) determining the total number of fast electrons, and (b) determining the fraction of the total that is absorbed in the compressed fuel shell.

The fraction 1/4 stated above stems from the fact[13] that at the time of peak fast-electron production, most of HXR-emitting CH mass is comprised within the original target volume. Therefore the relevant fraction of fast electrons is stated with respect to the total number of fast electrons intercepted by the area of the original target surface. Electrons outside this solid angle are not detected and are of no interest.

The divergence of fast electrons was studied with targets [Fig. 135.22(a)] in which Mo-coated solid glass spheres were placed at the center of nitrogen-filled CH shells. A series of targets were irradiated with a 1-ns square pulse while varying the Mo outer diameter D (~200 to 600 μm). The Mo–K_α line as well as the HXR were measured; both are signatures of fast electrons.[9] To extend the measurements to larger-diameter Mo shells (~800 μm), a Mo-coated CH shell target overcoated with CH was used [Fig. 135.22(b)]. Figure 135.22(c) is a photograph of the target type illustrated in Fig. 135.22(a), before being shot.

To ensure the same production of fast electrons in all the shots, the outer target diameter was the same (860±1% μm), as was the laser energy (26 kJ, to within ±1%). To minimize target motion, the outer CH thickness was 50 μm. This maintained similar underdense hydrodynamic conditions by ensuring a reproducible hot-electron source and limiting instabilities that could result from the acceleration of the shell, therefore decoupling the fast-electron transport from the hydrodynamics. The Mo layer in all targets was ~30 μm thick, which absorbed most of the fast electrons. This prevented refluxing (the re-entry
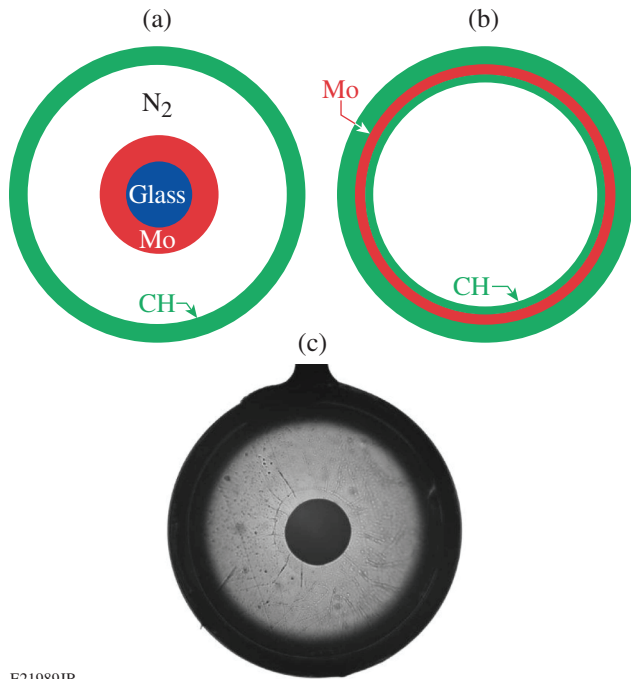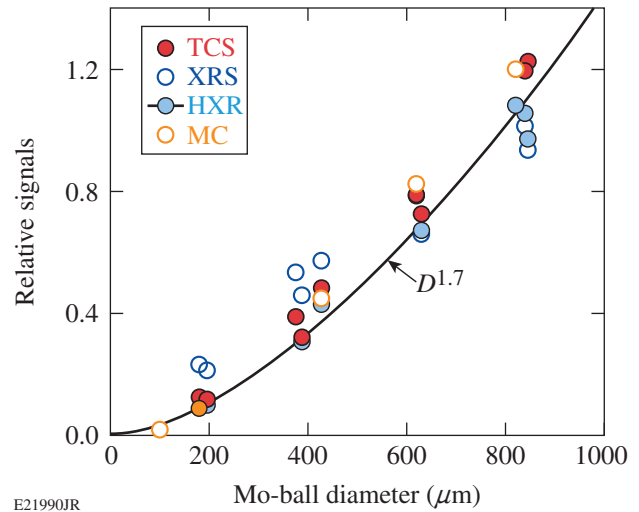
Figure 135.22
Target geometries: (a) Mo-coated solid glass sphere was placed at the center of a nitrogen-filled CH shell. A series of targets with varying Mo outer diameters was used to study the divergence. (b) To extend the divergence measurements to a larger-diameter Mo shell, a Mo-coated CH shell target was used (over-coated with CH). (c) A photograph of a target of type (a) before being shot.

of fast electrons after reflection from the electrostatic sheath around the target) and isolated the effect of divergence. The space between the CH shell and the Mo ball was filled with N_2 at ~1 atm to minimize electric-field effects. The 60-beam OMEGA Laser System[17] was used for these experiments and was smoothed by distributed phase plates,[18] 2-D spectral dispersion,[19] and polarization rotators.[20]

The Mo–K_α line was measured by two identical planar LiF crystal spectrometers (XRS's), as well as a Cauchois-type quartz crystal spectrometer (TCS).[21] The high-energy continuum spectrum (HXR) was measured by the four-channel hard x-ray detector (HXRD) spectrometer[22] from which the fast-electron temperature was determined. The relative energy in x rays above ~50 keV, measured by one of these channels, is reported in this article.

Figure 135.23 shows the intensity of the Mo–K_α line measured by the XRS and TCS, as well as the HXR radiation measured by the HXRD spectrometer. The *EGSnrc* Monte Carlo (MC) code[23] was used to simulate the transport of fast electrons and the emission of the Mo K_α and the HXR; these results, assuming a wide divergence of the fast electrons, are

Figure 135.23
The intensity of the Mo–K_α line measured by the XRS and TCS, as well as the hard x-ray radiation measured by HXRD. The Monte Carlo (MC) simulation results for a divergent fast-electron beam are also shown. The curve is the best fit to the HXR data. The increase of the signals with the Mo-shell diameter indicates a wide-angle divergence of fast electrons.

shown in Fig. 135.23. The incident fast electrons in the simulations are assumed to start from a point on the outer surface of the target and move isotropically within a half space. Unlike the Mo–K_α line, hard x rays are also emitted by the outer CH shell (not just the Mo layer), but the emission from the CH is independent of the Mo diameter (see Fig. 135.24); therefore, it
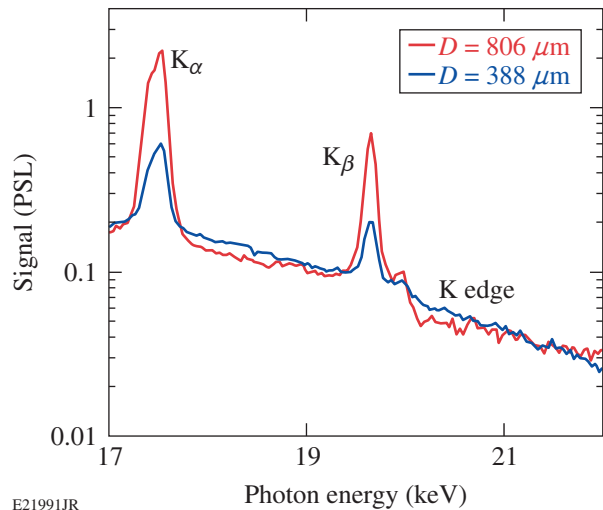
Figure 135.24
The measured x-ray spectrum for two Mo-shell diameters, used to assess the pumping of the Mo–K_α line by continuum radiation (above the Mo K edge). The continuum is emitted mostly by the outer CH shell; therefore it is about the same for all Mo diameters. PSL: photostimulated luminescence.[24]

must be a fraction of the total HXR emission for the smallest-diameter Mo target. That fraction was determined by running the MC code for an empty CH shell and was then subtracted from the HXR signals of all targets. The spread of the points can be related to the high sensitivity of fast-electron production to the laser intensity. A ±1% variation in both the laser energy and the outer target diameter (±3% in the overlapped intensity) corresponds to about ±10% variation in the K_α and the HXR signals.[11] The curve is the best fit to the HXR data.

The results of Fig. 135.23 show that fast electrons have a divergence extending at least to the original target diameter. As explained above, this is the relevant measure in assessing fast-electron preheat in cryogenic direct-drive implosions. The x-ray signals are not exactly proportional to the area of the Mo ball. MC simulations show that for the largest-diameter Mo ball, electrons are significantly slowed down because they traverse the CH shell diagonally and are significantly scattered out of the Mo layer because of the large angle of incidence on that layer. Without these effects the signals for $D \sim 800$ μm would align closer to a D^2 scaling. The most-obvious explanation for the close to ~D^2 rise in Fig. 135.23 is the wide-angle divergence of the fast electrons. The exact shape of the rise is unimportant; the very fact that the curve rises is an indication of divergence since a radially directed electron beam would result in constant signals, independent of D. The indicated minimum fast-electron divergence is given by the solid angle of the largest Mo ball at a point on the quarter-critical layer. Three alternative explanations to the rise in signals were investigated: electron scattering in the outer CH shell, radiation excitation of the Mo–K_α line, and a radial electric field related to the return current within the ionized N_2 fill gas.

Electron scattering in the CH was shown to be relatively unimportant by MC simulations using a narrow (<1-μm) radial electron beam for various Mo diameters. For a non-scattered beam, the energy in the Mo–K_α line should be independent of D. Instead, the MC simulations showed that the energy rises with D and reaches a plateau below $D \sim 300$ μm. Scattering broadens the electron beam to an extent consistent with the early rise in Fig. 135.23 but not with the rest of the curve.

The K_α line is excited by fast electrons but could also be pumped by the plasma radiation from the laser absorption region in the CH. Unless this contribution is small, the rise of K_α yield with D may not reflect fast-electron divergence (particularly since the radiation is isotropic). To examine this contribution to the measured K_α energy, the spectra for targets of two Mo diameters, ~400 and ~800 μm, are shown

in Fig. 135.24. The ratio of the K_α line intensities for the two shots is, as expected, about equal to the ratio in areas of the Mo balls. The continuum, which is emitted by the outer CH shell, is about the same for the two targets. The radiation contribution to the K_α line can be calculated through the integral $E_R = \int I_c(E)\,\omega_K\left[(K_\alpha)/E\right]dE$, where $I_c(E)$ is the continuum spectrum, $\omega_K = 0.76$ is the K_α fluorescence yield of Mo, and the integral extends upward from the K edge (at ~20 keV). Only the relative intensity of the spectrum is required for calculating E_R. For the larger diameter, E_R is less than ~10% of the total energy of the K_α line. For the smaller diameter, the relevant continuum intensity is smaller than that shown in Fig. 135.24 because the Mo shell intercepts only a fraction (~1/4) of the CH continuum. The relative contribution of the radiation is the same for all Mo diameters (but can best be determined from the larger diameter). Therefore, radiation pumping of the Mo–K_α line is unimportant. Additionally, it should be emphasized that the HXR measurements, shown to track the K_α measurements in Fig. 135.23, are related only to the fast electrons, thereby confirming the conclusions on fast-electron divergence.

The rise in the signals with D shown in Fig. 135.23 could be related to a retarding radial electric field caused by a return current that will reduce the values of the measured signals. For a radially directed fast-electron beam, the effect would increase with decreasing D^2 because of the increase in the fast-electron current density at decreasing radii. This possibility was addressed in two ways: First, the experiment was repeated using a lower laser energy (18 kJ instead of 26 kJ). This reduced the energy in fast electrons and consequently the electric field by a factor of ~80 (Ref. 11). Figure 135.25 shows the HXR signals for the two cases (the radiation contribution to the Mo–K_α line is larger for the low-power shots; therefore, the K_α data were omitted in Fig. 135.25). The shape of the two curves is approximately the same. If the rise in Fig. 135.23 resulted from electric-field effects, rather than fast-electron divergence, we would expect the lower-power curve to tend toward a constant value with increasing D.

Additionally, the electric field resulting from a return current in the N_2 gas between the Mo and CH shells has been estimated (no space charges can build up because they will lead to extremely high retarding fields). The total fast-electron current density at the quarter-critical surface was calculated as $J_{hot}(r_{1/4}) = f_{hot}eI_L/E_{hot}$, where f_{hot} is the fraction of instantaneous laser power that is converted to fast-electron power, I_L is the laser irradiance, and E_{hot} is a typical fast-electron energy. For the shots reported in Fig. 135.23, $I_L = 1.1 \times 10^{15}$ W/cm^2 and the HXRD-measured hot-electron temperature is ~50 keV;
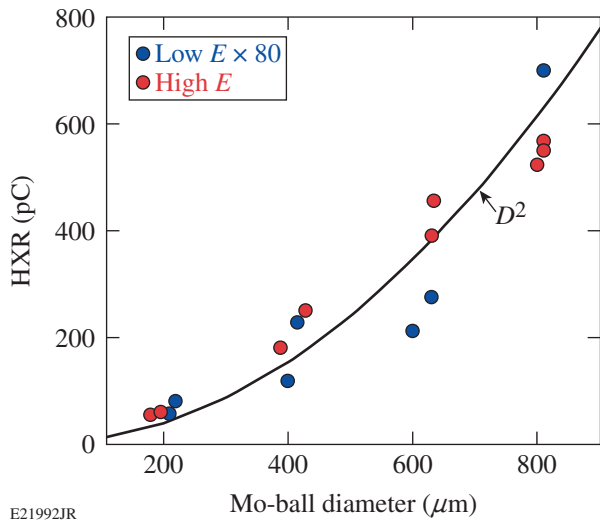
E21992JR

Figure 135.25
The hard x-ray measurements for 18- and 26-kJ laser energies, indicating a reduction by a factor ~80 in the production of fast electrons, consequently in the electric field. The D^2 curve serves merely to guide the eye. The similarity of the two sets of data sharply reduces the likelihood of electric-field effect on the results shown in Fig. 135.23.

(Refs. 11 and 12). Using Fig. 135.26(a), the instantaneous f_{hot} was determined and used to calculate the time history of $J_{hot}(r_{1/4})$. The calculated total current is of the order of a few megaamperes, which is much above the Alfvén limiting current,[25] forcing a return current density equal to $J_{hot}(r)$. The return current gives rise to a resistive radial electric field given by $E(r) = J_{hot}(r)/\sigma(r)$, where $\sigma(r)$ is the parallel Braginskii conductivity:[26] $\sigma = 1.96\,Ne^2\tau_e/m_e$ in terms of the electron collision time τ_e. We estimate $\sigma(r)$ using the temperature and ionization of the N_2 gas (no density dependence), simulated by the hydrodynamic code $LILAC$[27] for the case of a 200-μm-diam Mo ball. The fill gas was ionized by shock and radiation heating. Figure 135.26(b) shows the estimated electric potential drop across the N_2 gas for several times during the laser pulse. The time history of the field follows that of the HXR curve; the outer surface of the Mo layer is seen to expand in time as a result of heating by absorbed radiation; this is an additional source of ionization of the fill gas. The maximum electric potential is much smaller than typical fast-electron energy (~75 keV); therefore, the generated electric field has a negligible effect on the fast-electron current and the results shown in Fig. 135.23.

In conclusion, we have described a new technique for studying the divergence of fast electrons in laser fusion using Mo-coated balls embedded within CH shell targets. We have shown that the fast electrons generated on the OMEGA laser at an irradiance of ~1.1 × 10^{15} W/cm^2 are widely divergent. This result greatly improves the outlook for direct-drive

therefore, for a three-dimensional Maxwellian distribution, $E_{hot} \sim 75$ keV. Figure 135.26(a) shows the time histories of the laser power and the HXR for one of the shots shown in Fig. 135.23. Note that most of the fast electrons are produced in the latter part of the laser pulse. For a laser irradiance of 1.1 × 10^{15} W/cm^2, the time-integrated value of f_{hot} is ~0.01
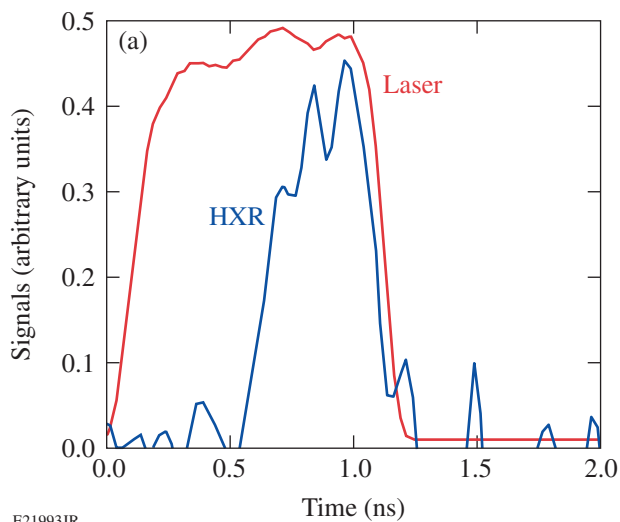
E21993JR

Figure 135.26
(a) The measured pulse shapes of the laser and hard x-ray (HXR) radiation. (b) The electric potential across the N_2 fill gas resulting from the return current produced by the radial fast-electron current is estimated at several times. The electric potential drop is much smaller than a typical fast-electron energy (~75 keV), thereby eliminating electric fields as a possible cause for the signal's rise shown in Fig. 135.23.

laser fusion by reducing the expected preheat. It also enables one to precisely determine the preheat in any given direct-drive laser-fusion experiment by using an electron-transport calculation in conjunction with a hydrodynamic code and a single observable: the emitted HXR. For imploding cryogenic targets on OMEGA, the maximum laser irradiance is $\sim 8 \times 10^{14}$ W/cm^2 and the total energy in fast electrons is $\sim 0.2\%$ of the laser energy,[11] but the results reported here show that only $\sim 1/4$ of the fast electrons will intersect the cold fuel and potentially preheat it. This reduces the fraction of fast-electron energy converted to preheat to less than $\sim 0.05\%$, well below the maximum tolerated. Therefore, preheat by fast electrons in current OMEGA cryogenic experiments is negligible. Polar-drive–ignition designs[28] for the National Ignition Facility (NIF)[29] with peak intensities of 1.1×10^{15} W/cm^2 show[28] that the cold fuel shell has converged by about a factor 2 around the time of maximum density scale length; therefore, the same reduction in preheat caused by fast-electron divergence is expected for polar-drive–ignition experiments on the NIF.

ACKNOWLEDGMENT

REFERENCES

1. M. N. Rosenbluth, R. B. White, and C. S. Liu, Phys. Rev. Lett. **31**, 1190 (1973).

2. H. A. Baldis and C. J. Walsh, Phys. Fluids **26**, 1364 (1983).

3. B. B. Afeyan and E. A. Williams, Phys. Plasmas **4**, 3827 (1997).

4. C. Stoeckl, R. E. Bahr, B. Yaakobi, W. Seka, S. P. Regan, R. S. Craxton, J. A. Delettrez, R. W. Short, J. Myatt, A. V. Maximov, and H. Baldis, Phys. Rev. Lett. **90**, 235002 (2003).

5. J. D. Lindl, *Inertial Confinement Fusion: The Quest for Ignition and Energy Gain Using Indirect Drive* (Springer-Verlag, New York, 1998), Chap. 11.

6. *LLE Review Quarterly Report* **79**, 121, Laboratory for Laser Energetics, University of Rochester, Rochester, NY, LLE Document No. DOE/SF/19460-317, NTIS Order No. DE2002762802 (1999). Copies may be obtained from the National Technical Information Service, Springfield, VA 22161.

7. R. L. McCrory, D. D. Meyerhofer, R. Betti, R. S. Craxton, J. A. Delettrez, D. H. Edgell, V. Yu Glebov, V. N. Goncharov, D. R. Harding, D. W. Jacobs-Perkins, J. P. Knauer, F. J. Marshall, P. W. McKenty, P. B. Radha, S. P. Regan, T. C. Sangster, W. Seka, R. W. Short, S. Skupsky,

V. A. Smalyuk, J. M. Soures, C. Stoeckl, B. Yaakobi, D. Shvarts, J. A. Frenje, C. K. Li, R. D. Petrasso, and F. H. Séguin, Phys. Plasmas **15**, 055503 (2008).

8. V. A. Smalyuk, D. Shvarts, R. Betti, J. A. Delettrez, D. H. Edgell, V. Yu. Glebov, V. N. Goncharov, R. L. McCrory, D. D. Meyerhofer, P. B. Radha, S. P. Regan, T. C. Sangster, W. Seka, S. Skupsky, C. Stoeckl, B. Yaakobi, J. A. Frenje, C. K. Li, R. D. Petrasso, and F. H. Séguin, Phys. Rev. Lett. **100**, 185005 (2008).

9. B. Yaakobi, P.-Y. Chang, A. A. Solodov, C. Stoeckl, D. H. Edgell, R. S. Craxton, S. X. Hu, J. F. Myatt, F. J. Marshall, W. Seka, and D. H. Froula, Phys. Plasmas **19**, 012704 (2012).

10. D. H. Froula, B. Yaakobi, S. X. Hu, P.-Y. Chang, R. S. Craxton, D. H. Edgell, R. Follett, D. T. Michel, J. F. Myatt, W. Seka, R. W. Short, A. Solodov, and C. Stoeckl, Phys. Rev. Lett. **108**, 165003 (2012).

11. D. H. Froula, D. T. Michel, I. V. Igumenshchev, S. X. Hu, B. Yaakobi, J. F. Myatt, D. H. Edgell, R. Follett, V. Yu. Glebov, V. N. Goncharov, T. J. Kessler, A. V. Maximov, P. B. Radha, T. C. Sangster, W. Seka, R. W. Short, A. A. Solodov, C. Sorce, and C. Stoeckl, Plasma Phys. Control. Fusion **54**, 124016 (2012).

12. D. T. Michel, A. V. Maximov, R. W. Short, J. A. Delettrez, D. Edgell, S. X. Hu, I. V. Igumenshchev, J. F. Myatt, A. A. Solodov, C. Stoeckl, B. Yaakobi, and D. H. Froula, Phys. Plasmas **20**, 055703 (2013).

13. V. N. Goncharov, T. C. Sangster, T. R. Boehly, S. X. Hu, I. V. Igumenshchev, F. J. Marshall, R. L. McCrory, D. D. Meyerhofer, P. B. Radha, W. Seka, S. Skupsky, C. Stoeckl, D. T. Casey, J. A. Frenje, and R. D. Petrasso, Phys. Rev. Lett. **104**, 165001 (2010).

14. S. P. Regan, N. B. Meezan, L. J. Suter, D. J. Strozzi, W. L. Kruer, D. Meeker, S. H. Glenzer, W. Seka, C. Stoeckl, V. Yu. Glebov, T. C. Sangster, D. D. Meyerhofer, R. L. McCrory, E. A. Williams, O. S. Jones, D. A. Callahan, M. D. Rosen, O. L. Landen, C. Sorce, and B. J. MacGowan, Phys. Plasmas **17**, 020703 (2010).

15. B. Yaakobi, T. R. Boehly, T. C. Sangster, D. D. Meyerhofer, B. A. Remington, P. G. Allen, S. M. Pollaine, H. E. Lorenzana, K. T. Lorenz, and J. A. Hawreliak, Phys. Plasmas **15**, 062703 (2008).

16. T. Döppner *et al.*, Phys. Rev. Lett. **108**, 135006 (2012).

17. T. R. Boehly, D. L. Brown, R. S. Craxton, R. L. Keck, J. P. Knauer, J. H. Kelly, T. J. Kessler, S. A. Kumpan, S. J. Loucks, S. A. Letzring, F. J. Marshall, R. L. McCrory, S. F. B. Morse, W. Seka, J. M. Soures, and C. P. Verdon, Opt. Commun. **133**, 495 (1997).

18. Y. Lin, T. J. Kessler, and G. N. Lawrence, Opt. Lett. **20**, 764 (1995).

19. S. Skupsky, R. W. Short, T. Kessler, R. S. Craxton, S. Letzring, and J. M. Soures, J. Appl. Phys. **66**, 3456 (1989).

20. T. R. Boehly, V. A. Smalyuk, D. D. Meyerhofer, J. P. Knauer, D. K. Bradley, R. S. Craxton, M. J. Guardalben, S. Skupsky, and T. J. Kessler, J. Appl. Phys. **85**, 3444 (1999).

21. J. F. Seely *et al.*, Rev. Sci. Instrum. **81**, 10E301 (2010).

22. C. Stoeckl, V. Yu. Glebov, D. D. Meyerhofer, W. Seka, B. Yaakobi, R. P. J. Town, and J. D. Zuegel, Rev. Sci. Instrum. **72**, 1197 (2001).

23. I. Kawrakow *et al.*, NRC, Ottawa, Canada, NRCC Report PIRS-701 (May 2011); I. Kawrakow, Med. Phys. **27**, 485 (2000).

24. A. L. Meadowcroft, C. D. Bentley, and E. N. Stott, Rev. Sci. Instrum. **79**, 113102 (2008).

25. S. Atzeni and J. Meyer-ter-Vehn, *The Physics of Inertial Fusion: Beam Plasma Interaction, Hydrodynamics, Hot Dense Matter*, International Series of Monographs on Physics (Clarendon Press, Oxford, 2004), p. 423.

26. S. I. Braginskii, in *Reviews of Plasma Physics*, edited by Acad. M. A. Leontovich (Consultants Bureau, New York, 1965), Vol. 1, p. 205.

27. R. Epstein, S. Skupsky, and J. Delettrez, J. Quant. Spectrosc. Radiat. Transf. **35**, 131 (1986).

28. T. J. B. Collins, J. A. Marozas, K. S. Anderson, R. Betti, R. S. Craxton, J. A. Delettrez, V. N. Goncharov, D. R. Harding, F. J. Marshall, R. L. McCrory, D. D. Meyerhofer, P. W. McKenty, P. B. Radha, A. Shvydky, S. Skupsky, and J. D. Zuegel, Phys. Plasmas **19**, 056308 (2012).

29. G. H. Miller, E. I. Moses, and C. R. Wuest, Opt. Eng. **43**, 2841 (2004).

Copper K-Shell Emission Cross Sections for Laser–Solid Experiments

Introduction

Fast-electron generation in laser–plasma interactions has long been of interest for a variety of reasons, such as avoiding preheat during compression in inertial confinement fusion (ICF), heating the compressed core of an ICF target for fast ignition,[1] generating a shock in an ICF target for shock ignition,[2] and as a means to produce energetic secondary particles,[3] such as protons[4] and gamma rays.[5,6]

K-shell emission[7,8] is a widely used fast-electron diagnostic in laser–solid experiments; it has also been used to provide a source of x rays at a specific energy. The most commonly used emitter in these experiments is copper. K-shell emission is produced when a fast electron knocks out a K-shell electron from an atom in the solid target, which is then replaced by an electron from an outer shell—a transition that leads to the emission of a photon with a characteristic energy in the x-ray band. If the outer shell involved is the L shell, the emission is called K_α; if it is the M shell, it is called K_β. K_α emission is more probable than K_β emission, so the majority of K-shell diagnostics used in laser–solid experiments rely entirely on K_α emission. It is assumed that the fraction of atoms with missing K-shell electrons, as a result of fast electrons or target heating, is always negligible. A fundamental parameter required when analyzing such measurements is the cross section for K-shell emission by fast electrons. The objective of this article is to identify a simple and accurate published expression for the K-shell emission cross section of copper. The principal motivation for this study was the analysis of K_α-emission diagnostics in laser–solid experiments at peak intensities above 10^{18} W/cm^2, where the fast-electron energy range of interest is roughly 0.1 to 10 MeV.

This work began with an analysis of time-resolved measurements of total K_α emission in laser–solid experiments;[7] 20-μm-thick copper foils were irradiated at normal incidence by ~1-ps laser pulses at intensities from 10^{18} to 10^{19} W/cm^2, and the x-ray emission was recorded using a streaked spectrometer. While looking for a simple expression for the K-shell emission cross section, a confusingly large selection of expressions was found, some of which differed significantly from one another.

A number of nonrelativistic expressions that use $1/E$ in place of $2/m_e v^2$, where E is the kinetic energy, m_e is the electron mass, and v is the velocity, could be immediately discarded as inaccurate at all energies of interest. Closer analysis of the remaining expressions showed that a number of these differences were caused by typing errors, which were identified by comparing the curves given with those in the respective papers, by comparing similar terms used in multiple papers, and by simple physical arguments. The only significant difference that remained was whether the cross section varied as $\ln E$ or $\ln(p^2/2m_e)$, where p is the momentum, which made a difference at relativistic energies. Comparison with the standard expression for electron stopping power suggested a third form, not used in any of the expressions. Furthermore, it suggested a reduction in the cross section at strongly relativistic energies, known as the density-effect correction, which had not been adequately considered. We then turned to measurements of K-shell emission from copper made with electron beams to select the most-accurate expression. Very few measurements in the 0.1- to 10-MeV region were found, so it was not possible to significantly narrow the number of apparently adequate expressions. Too few measurements were found with differences between them that were too large to clearly determine the correct limiting form at relativistic energies. Fortunately, for analyzing our measurements to determine a mean fast-electron energy, where only the relative K_α-emission rate as a function of electron energy was important, these differences were found to be irrelevant. They would be significant if absolute K_α yields were important, for example, to determine the number of fast electrons. To complete our study of K-shell emission, attention was turned to other possible sources of emission in laser–solid experiments, namely keV photons and MeV protons. A brief analysis of K-shell yields for photons and protons showed that the contribution from these sources may not always be entirely negligible, as originally assumed.

Although this work concentrates on copper, which is the most widely used in high-intensity laser–solid experiments and in electron-beam experiments, the basic considerations apply to any material and most of the expressions considered apply

to any material. We have also included some discussion on the variation with atomic number (Z).

In the following sections, the measurements and expressions are presented, followed by a brief discussion of the divergence in the expressions at relativistic energies. Next, the implications of the results for the interpretation of laser–solid experiments are considered, calculating emission rates and yields per electron as a function of electron energy. K-shell yields from other sources in laser–solid experiments that could be confounding factors for fast-electron diagnostics are then considered, namely photons and protons. Finally, our conclusions are presented, followed by the full expressions for the K-shell ionization cross sections in the appendix, with a number of typing errors corrected, and a simple fit for the K-shell emission cross section of copper is proposed.

Electron K-Shell Emission Cross Sections for Copper

K-shell emission cross sections σ_K have been measured using electron beams passing through thin copper films, down to a few nanometers in thickness, to a typical quoted accuracy of better than ±10%. The results, however, are always expressed in terms of K-shell *ionization* cross section σ_{ion}, given by

$$\sigma_K = f_K \sigma_{ion}, \qquad (1)$$

where f_K is fluorescence yield, for which different values have been used; it represents the fact that not all ionization events lead to emission of a photon. To obtain the K-shell emission cross section, it is important to correctly undo this step. Liu et al.[9] give a table of values from papers published before 2000, all modified to a fluorescence yield of 0.441, which simplifies the task. Since then, Llovet et al.[10] have published measurements, also using a fluorescence yield of 0.441, and Zhou et al.[11] have published measurements with an unstated fluorescence yield, but since this publication is from the same group as Liu et al.,[9] it seems reasonable to assume that they also used 0.441. We are unaware of any other measurements published before 2013. These values, plotted in Fig. 135.27, are multiplied by the atomic number density of solid copper n_a (8.49 × 10^{28} m^{-3}; copper will always refer to solid-density, un-ionized copper), giving what is known as the macroscopic cross section: the mean number of photons emitted per fast electron per meter.

Clearly the differences between various sets of measurements (individual experiments) are far greater than the quoted errors. Llovet et al.[10] give a clear explanation of the difference
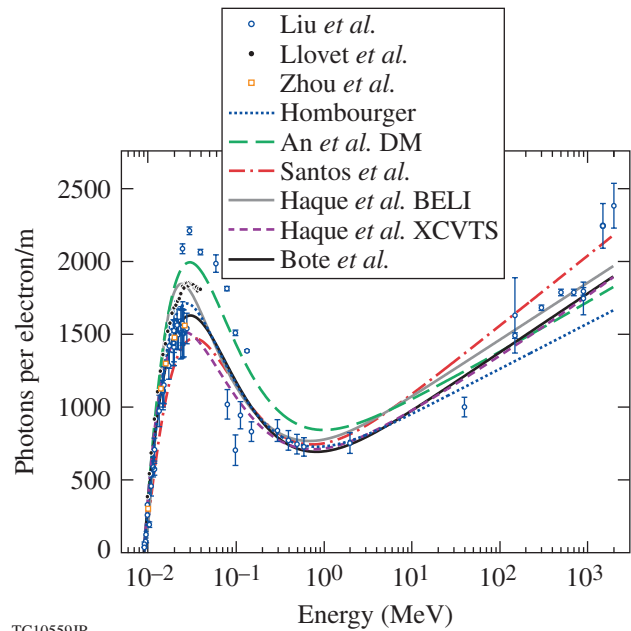
Figure 135.27
Macroscopic K-shell emission cross sections for solid copper. Points are from measurements given by Liu et al.,[9] Llovet et al.,[10] and Zhou et al.[11] Curves are from expressions given by Hombourger,[17] An et al.,[22] Santos et al.,[25] Haque et al.'s BELI model,[19] Haque et al.'s XCVTS model,[24] and Bote et al.[14] using a fluorescence yield of 0.45. DM: Deutsch–Märk.

between relative and absolute errors in such experiments and estimate theirs to be 2% and 10%, respectively (error bars not shown). We therefore conclude that the quoted errors are, in most cases, representative of the relative errors in the experiments. The uncertainty in the absolute values in Fig. 135.27 would have to be ~20% to make all but a few outlying points consistent with one another, but some of the measurements may have significant systematic errors.

The remainder of this section briefly discusses the general features of these measurements and how they vary with atomic number.

The threshold for K-shell emission is the K-shell binding energy B, or K edge, which is known from measurements and numerical calculations to be 8.98 keV for copper to a precision far greater than any of the other results considered here. K-shell binding energy scales approximately as $Z^{2.17}$. Above this threshold, the cross section rises sharply, peaks at ~3× the binding energy, then starts to fall. The large number of measurements in this region is in good agreement on the position and shape of the peak, if not on the absolute values. Above ~1 MeV, the cross section starts to increase continually from a minimum

that is roughly a factor of 2 below the initial peak for copper. The position of this minimum does not vary significantly with atomic number, and its depth decreases with increasing atomic number as the peak moves up toward it. Eventually it vanishes; for example, gold shows no clear local maximum or minimum in the cross section, showing what could be better described as a point of inflexion. Unfortunately, there are very few measurements in this region, which is the region of particular interest for high-intensity laser–solid experiments; there is only one point between 0.6 and 40 MeV. Therefore, all of the measurements, up to 2 GeV, have been included to see how well expressions interpolate over this region; however, a rigorous analysis of the correlation of the expressions with the measurements has not been carried out since it would be almost meaningless for our purposes.

The expressions—numerical, theoretical, and empirical—all consider the ionization cross section, so a fluorescence yield is required to give the emission cross section. Kahoul *et al.*[12] give a convenient compilation of measurements published before 2011. From these we chose to use 0.45 for three reasons: (1) it is the value from the most-recent measurement given (0.452±0.036); (2) it is the value from the measurement given with the smallest quoted error (0.452±0.003); and (3) it is the highest value since we noted a general tendency for the expressions to lie below the measurements. It should be noted that expressions with parameters obtained by fitting measurements all used fluorescence yields for copper from 0.4 to just under 0.45, so we may slightly overestimate the original fit in some cases. Kahoul *et al.* give five different fits for the fluorescence yield, all of which give adequate agreement with the measurements. The simplest is

$$f_K = 0.985 \frac{(Z/30.896)^{3.847}}{1+(Z/30.896)^{3.847}}, \qquad (2)$$

which gives 0.433 for copper.

K-shell ionization cross sections have been calculated numerically (for example, see Bote *et al.*[13]), but all of these calculations are approximate since an exact model for copper would require solving the full Dirac equation for 30 electrons (one incident electron and 29 electrons in the atom) and this would still neglect collective effects from many atoms. Therefore, these results are not necessarily a better reference than measured values. Also, we have not found a convenient set of tabulated numerical results. We will show Bote *et al.*'s[14] fit to

their numerical results, which has ten fitting parameters determined individually for every element, giving a stated accuracy better than 1% up to the maximum energy considered of 1 GeV.

A plethora of theoretical and empirical expressions exists for the K-shell ionization cross section. To limit the universe of expressions, we did not consider the many nonrelativistic ones that write a factor of $2/m_e v^2$ as $1/E$, leading to a cross section that falls continually with energy above the peak. Such expressions have been used in modeling laser–solid experiments, which would have led to significant errors; $2E/m_e v^2$ exceeds 1.1 at only 34 keV and exceeds 2 at 0.32 MeV. We then considered 12 relativistic expressions,[14–25] and there are almost certainly more out there. Since this time, a minor modification of Santos *et al.*'s expression[25] has been published by Guerra *et al.*[26] Only four expressions clearly failed to reproduce the measurements: Jakoby *et al.*'s[16] expression, Tang *et al.*'s[18] expression, Haque *et al.*'s Kolbenstvedt model,[20] and Haque *et al.*'s modified Deutsch–Märk model.[23] In the case of Jakoby *et al.*'s expression and Haque *et al.*'s Kolbenstvedt model, this failure appears to be caused, at least in part, by typing errors that we could not resolve. We identified and corrected typing errors in Grysinski's relativistic factor[27] in Casnati *et al.*'s,[15] Hombourger's,[17] and Gstir *et al.*'s[21] expressions. Eight models are too many to show conveniently in Fig. 135.27, so we have chosen to plot only six that envelope the range of values given by all eight expressions. The highest values are given by An *et al.*'s[22] version of the Deutsch–Märk model,[21] up to just beyond the dip, and by Santos *et al.*'s[25] expression at higher energies. The lowest values are given by Haque *et al.*'s BELI model[19] just above threshold, by Santos *et al.*'s[25] expression from there up to the peak, by Haque *et al.*'s XCVTS model[24] just beyond the peak, by Bote *et al.*'s[14] expression around the dip, and by Hombourger's[17] expression at higher energies.

The expression of Santos *et al.*[25] was used to model our experiments[7] because it was the first relativistic result we found and they had compared it to measurements for copper, showing adequate agreement; in hindsight we cannot give a rigorous justification for the choice of this expression.

The measurements of Llovet *et al.*[10] represent the most-extensive and accurate single set of measurements of emission cross section from just beyond threshold up to the peak (32 points, roughly a third of all the measurements, from 9.5 keV to 40 keV with a quoted relative error of ±2%), so it seems reasonable to use them to determine the most-accurate

expression for ionization cross section in this region, which may be of interest to others. To determine which expression was the most accurate without assuming a value for the fluorescence yield and without being influenced by possible systematic errors in the absolute values of the measurements, we used the gradient of a linear fit to expression versus measurement, the gradient closest to one indicating the most accurate. The expression of Hombourger was the most accurate, with that of Casnati *et al.* coming close. We then found the value of fluorescence yield for these two expressions that gave the best fit to the measurements, obtaining $f_K = 0.488$ for Hombourger and $f_K = 0.455$ for Casnati *et al.*, with Hombourger giving the best fit, as expected. This means that Casnati *et al.* gave the best fit using the fluorescence yield we chose of 0.45. A fluorescence yield of 0.488 is clearly higher than any measured value,[12] indicating that either Hombourger's expression is too low by a factor of 0.488/0.45 = 1.084, at least for copper, or that Llovet *et al.*'s[10] measurements are systematically high, which would be within their absolute error estimate of ±10%. Llovet *et al.*'s measurements are systematically higher than the measurements of Zhou *et al.*,[11] but it is not possible to tell whose measurements are more precise. On the other hand, such an increase in Hombourger's expression gives a result at relativistic energies that is closer to all of the other expressions.

Because of the large number and length of the expressions, we have placed them in an appendix, including our corrections to what appear to be typing errors. It is possible, however, to give a simple expression that summarizes them for electron energies E somewhat greater than threshold B (for nonrelativistic B), introducing only three dimensionless parameters f, g, and n that have a limited range of values:

$$\sigma_{ion} \sim \frac{N_K\,100\,(1+f)}{\beta^2 B_{keV}^{1+g}} \ln\left[\left(\frac{\gamma+1}{2}\right)^n \frac{E}{B}\right] \text{barns}, \qquad (3)$$

where N_K is the number of K-shell electrons; β is v/c, where v is the average relative velocity of the fast and K-shell electrons and c is the speed of light; γ is the Lorentz factor of the fast electron; f is between 0 and 1; g is typically 0 or close to 0; and n is 0 or 1. Most models use $n = 0$, while Santos *et al.*,[25] Guerra *et al.*[26] (not shown), and Bote *et al.*[14] [all based on the results of Scofield[28] (not considered)] along with Kolbenstvedt[29] (not considered) use $n = 1$. Scofield's expression was not considered because he gave no fitting parameters for copper; Kolbenstvedt's two expressions [his Eq. (11) and the sum of his Eqs. (14) and (15)] were not considered because

they are valid only well above threshold. [Haque *et al.*'s Kolbenstvedt model[20] does not have this form, which appears to be a typing error; $T(T + 2)$ should replace $(T + 2)$ in the log term.] The limited number of measurements above 1 MeV and the significant variations between them mean that a value of n cannot be determined with meaningful accuracy.

In most laser–solid experiments, only the K_α emission is considered, not the K_β emission, so if absolute numbers are required, the K-shell emission cross section must be multiplied by the fraction of K_α emission. Published measurements and numerical calculations of this fraction agree to within a few percent,[30] giving 0.880 for copper. Values can also be obtained from the code *FLYCHK*.[31] This fraction is roughly constant for atomic numbers from 20 to 30, then decreases slowly with atomic number, reaching 0.784 for gold. The copper K_α imagers used in laser–solid experiments image only the $K_{\alpha 1}$ line.[8] The fraction of K-shell emission in this line has not been as widely considered but can be obtained from *FLYCHK*, which gives 0.591 for copper. It should be noted that these ratios could be higher for many cases of interest as a result of ionization of outer shells caused by target heating.

Before moving on to consider the implication of these results for the interpretation of laser–solid experiments, we will briefly consider the bifurcation in the expressions at relativistic energies ($n = 0$ or 1) out of academic interest.

K-Shell Ionization Cross Section in the Relativistic Limit

The origin of $n = 1$ is a relativistic result for energy transfer to excitation of bound electrons caused by the electric field of a charged particle moving at constant velocity, often called the Bethe term. The origin for $n = 0$ could be the use of the nonrelativistic result $E = p^2/2m_e$ in the Bethe term or the use of the binary collision cross section. Surprisingly, both of these choices differ from the standard expression for fast-electron stopping power[32,33]

$$\frac{dE}{ds} = -\frac{Zn_a e^4}{4\pi\varepsilon_0^2 m_e v^2}$$

$$\times \left[\ln\left(\sqrt{\frac{\gamma+1}{2}}\frac{E}{I_{ex}}\right) - \frac{\delta}{2} + \frac{0.909}{\gamma^2} - \frac{0.818}{\gamma} - 0.284\right], \qquad (4)$$

where s is the path length, n_a is the atom number density, e is the electron charge, ε_0 is the permittivity of free space, I_{ex} is the mean excitation potential (322 eV for copper), which is usually

determined by fitting measurements, and δ is the density-effect correction, which we will return to later. Bremsstrahlung is not included in this expression. It applies to fast electrons with energy much greater than the binding energy of the electrons contributing to the stopping because they are assumed to be stationary. The connection to K-shell ionization cross section is more obvious if we consider the magnitude of the stopping power caused by only K-shell electrons:

$$
\left| \frac{dE}{ds} \right| = -\frac{N_K n_a e^4}{4\pi\varepsilon_0^2 m_e v^2}
$$

$$
\times \left[\ln\left(\sqrt{\frac{\gamma+1}{2}} \frac{E}{I_K} \right) - \frac{\delta}{2} + \frac{0.909}{\gamma^2} - \frac{0.818}{\gamma} - 0.284 \right]
$$

$$
> n_a B \sigma_{ion}, \tag{5}
$$

where I_K is the mean excitation potential for K-shell electrons, which exceeds their binding energy;[32] for example, for hydrogen the mean excitation potential is 19.2 eV, whereas the binding energy is 13.6 eV. The magnitude of the stopping power must be greater than $n_a B \sigma_{ion}$ because B is the minimum energy exchange in a K-shell ionization event and energy can be lost to K-shell electrons without ionizing them. This indicates that n should be 1/2, not 0 or 1—a value that has not been used in any expression we have encountered. The origin of this $n = 1/2$ is a combination of binary collisions for large energy transfers and the Bethe term for small energy transfers.

The density-effect correction represents a reduction in stopping power caused by shielding of the fast electron's charge by surrounding electrons, which is not considered in the Bethe term. It increases with density of the surrounding electrons and with fast-electron energy, occurring only above a threshold energy in insulators. It has not been included in any of the expressions considered here, although Santos *et al.* state that it should be included at energies greater than a GeV and Scofield,[28] who did not consider copper, did include it. In copper, the reduction in total stopping power exceeds 10% above roughly 10 MeV (Refs. 32 and 33), indicating that the density effect should be considered at energies considerably less than a GeV, and this energy will decrease with increasing atomic number. The general expression is complex, but it has a simple limiting form for strongly relativistic electrons:

$$
\frac{\delta}{2} \longrightarrow \ln\left(\frac{\gamma\hbar\omega_p}{I_{ex}} \right) - \frac{\beta^2}{2}, \qquad \beta \longrightarrow 1, \tag{6}
$$

where $\hbar\omega_p$ is the plasmon energy calculated from total electron density (58.3 eV for copper). Equation (6) is within 10% of a more-accurate calculation for copper[32,33] above roughly 30 MeV; at lower energies it is an underestimate.

This implies that the rate of increase in the K-shell ionization cross section with energy should noticeably decrease at strongly relativistic energies. If the density-effect correction is not included in the expressions of Santos *et al.*[25] and Guerra *et al.*,[26] the inequality in Eq. (5) will not hold in the strongly relativistic limit (to this extent they are correct to state that the density effect should be included above 1 GeV). For expressions using $n = 0$, including the density effect will give a cross section that becomes independent of energy at strongly relativistic values, indicating that $n = 0$ is not a physically correct choice. Scofield[28] did find that the density effect led to the cross section becoming independent of energy, but this appears to be a mistake in using δ in place of $\delta/2$ combined with his use of $n = 1$. The maximum cross section he gives is lower than values that have been measured at high energies and no saturation in any K_α cross section has yet been reported.

Calculations and fitting formulas of the density-effect correction are readily available.[32–34] We found that the total stopping power of copper[32,33] was reproduced to within 1% by using

$$
\frac{\delta}{2} = \ln\left[1 + (\gamma-1) \frac{\hbar\omega_p}{I_{ex}} \exp(-0.5) \right], \tag{7}
$$

which is zero at zero energy and tends to Eq. (6) in the relativistic limit, but does not fit at intermediate energies; however, here the density-effect correction makes a negligible contribution to the stopping power and the same would be expected for the K-shell ionization cross section. This will also work well for higher-Z metals; we have found that it works better for molybdenum, but not insulators, where there is a threshold energy for the density effect to occur.

There is a potential complication when considering the inclusion of the density effect: the nanometer-thick films used in many of the measurements could suppress it because it is a collective effect that requires a minimum amount of material. For a strongly relativistic electron, the relevant length scale should be c/ω_p, which is 3.4 nm for copper, so this is a concern. Evaluating the density effect in this case will require numerical calculations. We therefore conclude that the correct value of n

appears to be 1/2 and that the density-effect correction should be included for copper at fast-electron energies above 10 MeV and at lower energies for higher atomic numbers.

Finally, it should be noted that these considerations as to which value of n is physically correct and the need to include the density-effect correction strictly apply only to physics-based expressions, such as those of Santos et al.[25] and Guerra et al.[26] Expressions with free parameters used to fit measurements could still give adequate fits over any energy range of interest, whatever value of n is assumed and without including the density effect, although a better physical basis for a fitting function should allow one to obtain a better fit. If an expression with free parameters is modified, the free parameters should be redetermined.

K-Shell Emission as a Fast-Electron Diagnostic in Laser–Solid Experiments

Some of the implications of these results for K-shell emission diagnostics in laser–solid experiments will now be considered, the first being the choice of a K-shell emitter based on K-shell yield.

Using $\sigma_{ion} \propto Z^{-2.17}$ and Eq. (2) for the fluorescence yield, we find that there is a maximum in the K-shell emission cross section at an atomic number close to 21, which is scandium. Considering the atomic number density of solids in this region, the maximum macroscopic cross section should belong to titanium (22), which has been used in high-intensity laser–solid experiments almost as frequently as copper. Considering that the K-shell emission self-absorption depth is roughly proportional to the atomic number, increasing the thickness of the layer from which emission can be obtained and consequently total yield, we find that maximum yield occurs near 29, which is copper. This provides a further motivation for concentrating on copper, although, given the approximations made, nickel or zinc could give a higher yield. The available measurements do not allow one to more precisely determine the maximum emission cross section and maximum yield.

For time-resolved measurements, the key parameter is an emission rate of $n_a \sigma v$; the results given in Fig. 135.27 multiplied by velocity are shown in Fig. 135.28. The emission rate has no initial peak and is almost independent of energy over the range of interest. This means that the K_α-emission rate is, to a good approximation, proportional to the number of fast electrons, provided that the mean energy is much greater than the binding energy. Our results,[7] which did not depend on
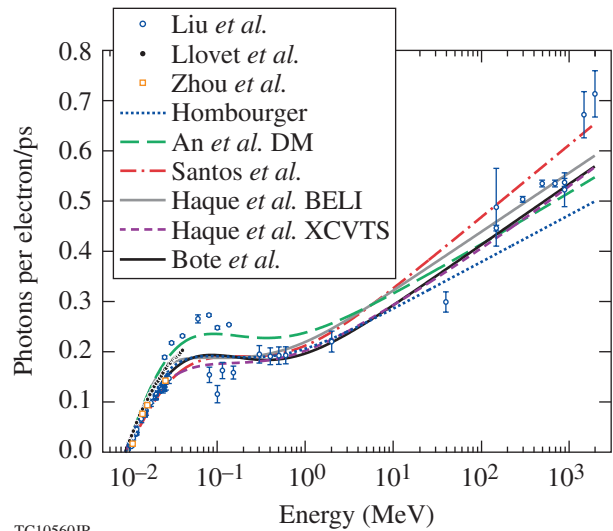

Figure 135.28

Same as Fig. 135.27 but multiplied by the electron velocity to give the emission rate in copper.

absolute values, were found to be insensitive to the expression used and to some accidental variations of individual terms in the expression of Santos et al.[25] by a factor of 2 because all of these expressions give an approximately constant emission rate at the relevant energies. This would not have been the case if the mean fast-electron energy was not much greater than the binding energy; just above the binding energy, the emission rate increases significantly with energy and the different expressions would give noticeably different results.

The most important parameter in determining the sensitivity of K-shell emission diagnostics to electron energy is the yield per electron Y, so we will now calculate this for two cases of particular interest to laser–solid experiments.

For an isolated copper foil, the vast majority of the electrons will be confined to the foil by the electrostatic field they generate, so K-shell emission yield will be determined by the emission rate times the stopping time. Considering only stopping resulting from collisions given by Eq. (4), the yield is

$$Y = \int_B^E \frac{n_a \sigma_K}{|dE/ds|} \, dE. \tag{8}$$

To illustrate this result for copper, we used only the BELI model of Haque et al.[19] since it lies roughly in the middle of the others over the energy range of interest. This yield is given by the

upper line in Fig. 135.29; it increases continually with energy, tending to a linear increase at high energies. Bremsstrahlung would lead to the yield flattening out by about 60 MeV, when it becomes the dominate energy-loss mechanism in copper.[32]
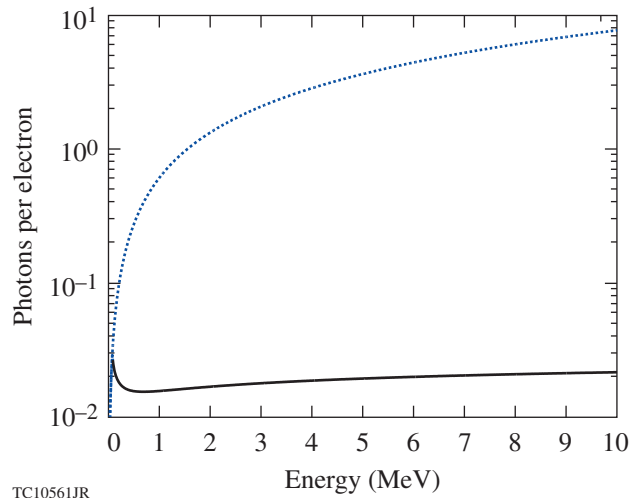

TC10561JR

Figure 135.29
K-shell yield per electron including collisional stopping in solid, un-ionized copper for electrons that stop in the copper (dotted blue line) and electrons that travel a maximum distance of 20 μm (solid black line).

Equations (3) and (8) indicate that ZBY/f_K as a function of E/B should be weakly dependent on material, while bremsstrahlung is negligible, so this result can be readily scaled to any material of interest. Bremsstrahlung will lead to the yield flattening out at lower energies for higher atomic numbers.

Most K-shell emission experiments use a thin layer buried within a thick target. For electrons that maintain a constant velocity and travel a distance s, the yield is simply $n_a\sigma_K s$; therefore, its variation with energy is the same as that for the macroscopic cross section given in Fig. 135.27. The lower line in Fig. 135.29 gives the yield for electrons traveling a maximum distance of 20 μm, a typical upper value for the thickness of a copper fluor layer since it is roughly the attenuation depth of the K-shell emission. This gives a yield that is practically independent of energy from 0.7 to 10 MeV. Below this there is a narrow peak, where the yield increases by a factor of 1.9; then below 60 keV, the yield rapidly becomes negligible. In practice, the yield per electron from a 20-μm copper layer would lie between the two curves in Fig. 135.29 because the distance traveled by an electron going through the layer at an angle θ to the normal will be 20/cosθ μm and angular scattering will increase the average path length,[35] more so for lower-energy electrons. Therefore, to a first approximation, copper K-shell emission from a thin layer in a thick target is proportional to the number of electrons above roughly 60 keV that reach it, provided that the majority of electrons reaching it exceed this energy.

An important general feature to note from Fig. 135.29 is that collisions significantly suppress the K-shell emission yield of electrons with an energy up to roughly 6× the threshold energy; therefore, the effective detection threshold is significantly higher than might be expected. The physical reason for this is that electrons just above threshold are far more likely to lose their energy colliding with one of the other electrons in the material than to cause K-shell emission. Another important feature is that the local maximum in the K-shell emission cross section does not lead to the emission being particularly sensitive to a narrow range of fast-electron energies, as is often assumed. For mean energies well above the effective threshold, K-shell emission, either time resolved from an isolated thin foil or time integrated from a thin foil buried in a thick target, is most sensitive to the number of fast electrons and not sensitive to their energy. The energy distribution can be inferred from the variation in signal with time or depth, provided the energy dependence of stopping time or distance is known. The only significant difference between the expressions we have considered will be in determining the absolute number of fast electrons. For mean energies that are not much greater than threshold, K-shell emission will be dominated by the higher-energy electrons in the distribution and interpretation of the results will be sensitive to the shape of the cross section near threshold, where the expressions we have considered are noticeably different.

Another important factor when evaluating absolute yields in experiments is the opacity of the target, which can change significantly as it ionizes, but this will not be considered here.

We will next examine how accurate it is to assume that K-shell emission measurements in laser–solid experiments are due entirely to fast electrons.

Other Sources of K-Shell Emission
An essential requirement when using K-shell emission as a fast-electron diagnostic is that fast electrons be the primary source of the emission, but photons and ions can also cause K-shell emission and are also produced in laser–solid interactions, so we will briefly consider the yields from these other potential sources of K-shell emission.

1. Photons

To estimate the yield from photons, we considered only photons below the threshold for pair production (1.022 MeV) where absorption is caused only by photoionization. For the fraction of K-shell photoionizations in copper, we used 0.8796, as used in the EGS Monte Carlo code;[36] therefore, we need to calculate only 0.8796× the number of photons absorbed in the copper. To do this, we assumed an isotropic photon source and averaged exponential attenuation over all straight-line trajectories through a sheet of thickness s, obtaining

$$Y = 0.396 \left[1 - \exp\left(-\frac{s}{l_{ph}}\right) + \frac{s}{l_{ph}} E_1\left(\frac{s}{l_{ph}}\right) \right], \qquad (9)$$

where E_1 is the exponential integral and l_{ph} is photon attenuation depth, obtained from XCOM,[37] excluding photon scattering, which makes only a small contribution to photon attenuation. This result for a 20-μm copper layer is plotted in Fig. 135.30 along with the previous results for electron yields.
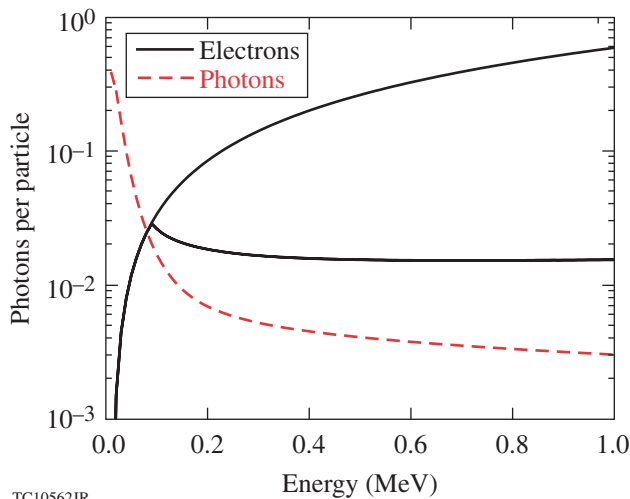
TC10562JR

Figure 135.30
K-shell yield per photon for an isotropic distribution of photons incident on a 20-μm copper layer and the yields per electron from Fig. 135.29.

The yield for photons has a maximum at threshold and decays continually with energy, whereas the yield for electrons is zero at threshold and increases continually with energy. This indicates that, for copper, photons less than 70 keV are of particular concern because they could cause more K-shell emission than electrons with only a fraction of the energy of the electrons. This justifies the neglect of photons above 1 MeV, although the pairs produced by higher-energy photons would contribute to K-shell emission (not considered here).

Three principle sources of photons in laser–solid experiments could cause K-shell emission: bremsstrahlung from fast electrons in the target, emission from the laser-heated plasma on the front surface, and line emission from higher-Z elements, if present.

Bremsstrahlung will turn a fraction of the fast-electron energy into photons with a comparable energy distribution. This fraction, the radiation yield, increases with electron energy and the atomic number of the target.[32] Radiation yield becomes significant only for electron energies greater than 1 MeV, where electrons always have a far greater K-shell yield than photons, so in most cases bremsstrahlung will not make a significant contribution to the total yield, with the possible exception of very high-Z targets. Even though the *total* yield from bremsstrahlung photons should be negligible, the K-shell emission from a layer at a large-enough depth may be dominated by bremsstrahlung photons because the attenuation depth of photons is larger than the mean free path of electrons at the same energy. In other words, the fraction of the fast-electron energy distribution converted into photons would be expected to propagate farther into a target than the fast electrons.

The laser-driven plasma could emit a significant number of photons just above the K edge. Unfortunately, it is not straightforward to estimate this emission since the systems of interest are usually far from equilibrium; therefore we cannot, in general, easily rule out a significant contribution to K-shell emission from this source. A good means of quantifying this in experiments would be to measure the x-ray emission in the relevant range from the front of the target.

If elements with a higher Z than the K-shell emitting layer are used in targets (for example, to give two emitters in one target), the line emission must be carefully considered; a non-negligible fraction of the emission from the higher-Z layer could cause emission from the lower-Z layer. This must be considered for each individual target design.

2. Protons

For ions we will consider only protons since they are always present; because of impurities, protons are the ions that are most efficiently accelerated in laser–plasma interactions and they have, by far, the lowest stopping power of all ions.

To estimate the yield from protons in copper, we used the K-shell ionization cross section from Kahoul *et al.*[38] (given in the appendix), who fitted a compilation of experimental results between 80 keV and 13 MeV, and we used the proton-stopping
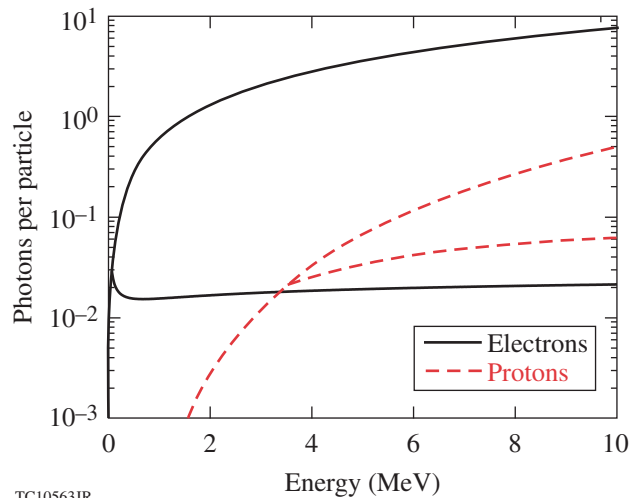
Figure 135.31
Same as Fig. 135.29 but for protons as well as electrons.

power given by PSTAR.[39] The result, seen in Fig. 135.31, is combined with our previous results for the yield from electrons.

Proton and electron energies have been found to be strongly correlated to one another in laser–solid interactions,[3] so it is reasonable to compare the yields at the same energies. For a thin, isolated target where the majority of the electrons are expected to recirculate and any protons are expected to go through the target, K-shell emission yield per proton will always be lower than that per electron. For a thin layer in a thick target, the yield per proton can exceed the yield per electron; for a 20-μm copper layer this occurs above 3.4 MeV because the cross section for protons then exceeds that for electrons. Despite this, the total yield from protons would be expected to be lower than that from electrons because the fraction of laser energy transferred to protons entering the target has been found to be lower than that for electrons, for parameters of interest. Emission from protons accelerated into the target may not be entirely negligible, however, particularly at the higher intensities used, and there could be regions in the target where the number of protons equals or exceeds the number of electrons, so it would be worth considering in a more-detailed analysis.

Conclusions

Nine expressions for K-shell ionization cross sections[14,15,17,19,21,22,24–26] have been identified that, based on published measurements for copper,[9–11] appear to be adequate for modeling copper K-shell emission diagnostics used in high-intensity laser–solid experiments. For the fluorescence yield required to convert the K-shell ionization cross section to the K-shell emission cross section, a useful summary of measure-

ments and fitting formulas has been given by Kahoul *et al.*[12] For copper we chose 0.45 and, if required, we would consider the uncertainty in this value to be ±0.01. For the fraction of K-shell emission in the K_α line, published measurements and numerical calculations[30,31] are in good agreement, giving 0.880; a reasonable estimate of the uncertainty in this value would be ±0.01. We were unable to narrow down the field because very little attention has been paid to energies from 0.1 to 10 MeV. Instead, past attention has concentrated on the behavior of ionization cross sections near threshold. In this region, the expression given by Hombourger[18] with a fluorescence yield of 0.488 gave the best fit to measurements. The only models that are clearly inadequate are the nonrelativistic ones that use a factor of $1/E$ in place of $2/m_e v^2$.

Should an estimate of the uncertainty in the K-shell emission cross section be required, we suggest a conservative value of ±20%. Alternatively, a number of these expressions that give upper and lower bounds on the cross section could be used. We found that six expressions were required to give upper and lower bounds over the full range of energies, at least for copper, but for most applications four expressions should be sufficient: Santos *et al.*[25] (or Guerra *et al.*[26]), An *et al.*,[22] Hombourger,[18] and Bote *et al.*[14]

In examining these models we identified an unresolved issue regarding the energy dependence of the ionization cross section at relativistic energies: the factor *n* in Eq. (3), where either 0 or 1 is used. By comparison with the standard result for fast-electron stopping power,[32] we found that $n = 1/2$ appears to be the correct choice. Furthermore, we found for copper that the density-effect correction should be considered above 10 MeV, and this energy will decrease with an increasing atomic number. The available measurements at strongly relativistic energies are insufficient to indicate which form is correct and how the density-effect correction should be included. In order to provide an adequate fit to cross sections for energies of current interest, these are not important issues but are interesting physics issues for future work in this area.

Using these results and the standard expression for electron stopping power, it was found that the effective detection threshold of K-shell emission diagnostics is roughly 6× higher than the threshold energy for causing K-shell emission. Both the K_α-emission rate, as used in our experiments,[7] and the total K_α emission from typical buried layer experiments are approximately proportional to the number of electrons above this threshold and are not sensitive to the electron energy, provided that the majority of fast electrons are above the

effective detection threshold. Near the detection threshold, K_α emission is far more sensitive to electrons with higher energies, and current uncertainties in the cross section will lead to significant uncertainties in interpreting measurements. The local maximum in the K_α-emission cross section does not lead to K_α emission being particularly sensitive to a narrow range of electron energies, as is often assumed.

K-shell emission caused by photons and protons was briefly considered. Photons from the laser-heated plasma and higher-Z layers could make a significant contribution in some experiments and deserves careful consideration. Protons accelerated into the target should not make a significant contribution because of their smaller number, but if significant numbers of protons above 3 MeV are accelerated into the target, they should be considered in a more-detailed modeling.

Appendix A: Expressions for K-Shell Ionization Cross Sections

For the incident electron we use E for kinetic energy, v for velocity, β for v/c, where c is the speed of light, and γ for the Lorentz factor $(1 + E/m_e c^2)$, where m_e is the electron mass. For the K-shell electrons we use B for binding energy, B_{keV} when it is expressed in keV (SI units are used unless specified), and N_K for number (2 for all cases of interest). The material is indicated by its atomic number Z. Three expressions use Rydberg energy R (13.606 eV). Two dimensionless parameters are used in most expressions:

$$U = \frac{E}{B}, \qquad (A1)$$

often called the overpotential, and

$$J = \frac{m_e c^2}{B} \qquad (A2)$$

(56.9 for copper), which appears naturally when writing relativistic expressions in terms of U. A number of the expressions use Grysinski's relativistic factor[27] written as

$$G = \frac{1+2J}{U+2J}\left(\frac{U+J}{1+J}\right)^2$$

$$\times \left[\frac{(1+U)(U+2J)(1+J)^2}{J^2(1+2J)+U(U+2J)(1+J)^2}\right]^{1.5}, \qquad (A3)$$

which is intended to convert a nonrelativistic expression for energy exchange in a binary collision between electrons with kinetic energies E and B to a relativistically correct expression. This always appears as G/E, so we introduce the parameter

$$G' = \frac{G}{2(\gamma-1)} = \frac{JG}{2U}. \qquad (A4)$$

The reason for this choice, and the effect of this complex-looking term, can be easily illustrated by considering a non-relativistic binding energy $J \gg 1$, valid for most cases of interest,

$$G' \approx \frac{1}{\beta^2}, \qquad B \ll m_e c^2, \qquad (A5)$$

so Grysinski's relativistic factor essentially replaces the $1/E$ in nonrelativistic expressions with $2/m_e v^2$. We believe that a number of the expressions have typing errors in this factor.[15,17,21]

Casnati et al.'s[15] expression for any element is

$$\sigma_0 = \frac{N_K \, 187}{B_{keV}^{1.0318}} \text{ barns},$$

$$f = -\frac{0.316}{U} + \frac{0.1135}{U^2},$$

$$\sigma_{ion} = \sigma_0 G'\left(\frac{R}{B}\right)^f \exp\left(-\frac{1.736}{U} + \frac{0.317}{U^2}\right)\ln U. \qquad (A6)$$

Tang et al.[18] used this expression and obtained different fitting parameters: 137 and 1.0514 in σ_0, –0.4935 and 0.3529 in f, and –1.227 and –0.2791 in the exponential. Note that a_0 in their expression should be a_0^2 and that their coefficients C_{1-3} have the wrong sign, or, equivalently, it should be $-C_u$ or $\left(E_k/R_y\right)$ in place of $\left(R_y/E_k\right)$.

Jakoby et al.'s[16] expression and Haque et al.'s[20] Kolbenstvedt expression, as printed, do not reproduce the published figures. Even after correcting a number of obvious typing errors and experimenting with likely looking variants, we could not obtain sensible results; therefore we have not reproduced them here.

Hombourger's[17] expression for any element is

$$\sigma_0 = \frac{N_K\,175}{B_{keV}^{1.0305}} \text{ barns,}$$

$$f = -\frac{0.316}{U} + \frac{0.1545}{U^2}, \tag{A7}$$

$$\sigma_{ion} = \sigma_0 G' \left(\frac{R}{B}\right)^f \left(1 - \frac{1.335}{U} + \frac{0.6006}{U^2}\right) \ln U.$$

We suggest using $N_K\,190 \big/ B_{keV}^{1.0305}$ for σ_0 based on fitting this expression to the measurements of Llovet *et al.*[10] and measurements of the fluorescence yield for copper[12] that indicate a value of 0.45.

Haque *et al.*'s[19] BELI expression for any element is

$$\sigma_0 = \frac{N_K\,205}{B_{keV}} \text{ barns,} \tag{A8}$$

$$\sigma_{ion} = \sigma_0 G' \left[1 + 3\left(\frac{1 - N_K/Z}{U}\right)^{1.27}\right]$$

$$\times \left[\ln(U) + \sum_{n=1}^{5} b_n\left(1 - \frac{1}{U}\right)^n\right],$$

where b_n is –0.971, 0.381, 0.0952, –0.0476, and –0.190. The term in brackets following Grysinski's relativistic factor represents shielding of the K-shell electrons by the remaining electrons in the atom.

A number of expressions have been based on the Deutsch–Märk model. For these we use

$$\sigma_0 = 1.72 \times 10^{-3} f_H r_K^2, \tag{A9}$$

where $f_H = 0.553$ for hydrogen and = 1 otherwise and r_K is the radius of maximum areal density, tabulated (in units of the Bohr radius 5.2918×10^{-11} m) by Desclaux,[40] which is 1.807×10^{-12} m for copper. The most-recent version we found from the originators of the model is Gstir *et al.*:[21]

$$\sigma_{ion} = \sigma_0 \left(1 + \frac{2U^{0.25}}{J^2}\right) G' \left(\frac{U-1}{U+1}\right)^{1.06}$$

$$\times \left(1.353 - \frac{0.55}{U}\right) \ln\left(2.7 + \sqrt{U-1}\right). \tag{A10}$$

The first term in parentheses is a modification to Grysinski's relativistic factor. An *et al.*[22] have since determined the fitting parameters including subsequent measurements:

$$\sigma_{ion} = \sigma_0 \left(1 + \frac{2U^{0.25}}{J^2}\right) G' \left(\frac{U-1}{U+1}\right)^{0.95}$$

$$\times \left(1.4 - \frac{0.475}{U}\right) \ln\left(2.7 + \sqrt{U-1}\right). \tag{A11}$$

Haque *et al.*[23] give a significantly modified version

$$\sigma_{ion} = \sigma_0 \frac{1 + 1.5J}{1.2J} \left(1 + \frac{1.5U^{0.055}}{J}\right)$$

$$\times G' \left(1 + 6.75\,\frac{1 - N_K/Z}{Z^{0.5}\,U}\right)^{0.85} \tag{A12}$$

$$\times \left[0.86 - \frac{0.63}{1 + (U/3.76)^{2.08}}\right] \ln(1.01U).$$

The first two terms are modifications to Grysinski's relativistic factor, and the term following it represents shielding of the K-shell electrons by the remaining electrons in the atom. We believe there may be typing errors in this expression.

Haque *et al.*'s[24] XCVTS expression is

$$\sigma_0 = \frac{N_K\,4.5 \times 10^6\,B_{keV}}{Z^{4.35}} \text{ barns,}$$

$$\sigma_{ion} = \sigma_0 \left(\frac{U+J}{1+J}\right)^{0.02} \left(1 - \frac{0.22U^{0.27}}{J^2}\right) \tag{A13}$$

$$\times G' \left(1 + 0.01\frac{Z - N_K}{U}\right) \ln U.$$

The first term is a modification to Grysinski's relativistic factor. The next term in parentheses, introduced to prevent the expression from increasing without limit, cannot be correct for strongly relativistic energies since it will eventually lead to a negative cross section; there is also nothing to indicate that the cross section does not increase continually with energy. The term after Grysinski's relativistic factor represents shielding of the K-shell electrons by the remaining electrons in the atom.

Bote et al.'s[14] fit to their numerical results for copper is

$U \leq 16$,

$\sigma_0 = 351.9$ barns,

$$\sigma_{ion} = \sigma_0 \frac{U-1}{U^2}$$

$$\times \left[3 + 0.05003 U - \frac{3.48}{1+U} + \frac{3.339}{(1+U)^3} - \frac{3.683}{(1+U)^5} \right]^2,$$
(A14)

$U > 16$,

$$\sigma_0 = \frac{22.84 U}{U + 0.765} \frac{1}{\beta^2} \text{ barns},$$

$$x = \sqrt{\gamma^2 - 1},$$

$$\sigma_{ion} = \sigma_0 \left\{ \left[\ln(x^2) - \beta^2 \right] \left(1 + \frac{0.3024}{x} \right) \right.$$

$$\left. + 6.261 - \frac{1.024}{\sqrt{\gamma}} + \frac{0.4543}{x} \right\}.$$

The fitting parameters for other elements can be found in Bote et al.'s paper. Note that they calculate the binding energy of copper to be 8.95 keV, not 8.98 keV.

For Santos et al.[25] and Guerra et al.'s[26] expressions, we use

$$\sigma_0 = \frac{N_K}{B_{keV}} 255 \text{ barns},$$
(A15)

$$\sigma_B = \sigma_0 \left\{ \frac{1}{2} \left[\ln\left(\frac{\gamma+1}{2} U \right) - \beta^2 \right] \left(1 - \frac{1}{U^2} \right) + 1 - \frac{1}{U} \right.$$

$$\left. + \left(\frac{2}{\gamma+1} \right)^2 \left[\frac{U-1}{2J^2} - (2\gamma-1) \frac{\ln U}{1+U} \right] \right\}.$$

We believe that the density-effect correction $(-\delta/2)$ should be inserted in the first set of square brackets. This is divided by a term of the form β^2, which could be interpreted as the mean-

squared relative velocity of the incident and K-shell electrons. Santos et al.[25] give

$$\sigma_{ion} = \frac{\sigma_B}{2} \left(\frac{1}{\beta^2} + \frac{1}{\beta^2 + \beta_B^2 + \beta_K^2} \right),$$
(A16)

where

$$\beta_x^2 = 1 - \frac{1}{\left(1 + x/m_e c^2 \right)^2},$$
(A17)

where x is an energy and K is the mean kinetic energy of the K-shell electrons, tabulated in Santo et al.'s paper (11.32 keV for copper). Guerra et al. give

$$\sigma_{ion} = \frac{\sigma_B}{\beta^2 + \left(0.126 - 0.213 Z + 0.195 Z^2 \right) (2R/B) \beta_B^2}.$$
(A18)

Kahoul et al.'s[38] expression for copper K-shell ionization by protons is

$$x = \ln\left(\frac{E_{MeV}}{16.489} \right),$$

$$\sigma_{ion} = \frac{\exp\left(11.292 + 0.192 x - 0.371 x^2 + 0.028 x^3 \right)}{80.6404} \text{ barns}.$$
(A19)

The fitting parameters for other elements can be found in Kahoul et al.'s paper.

Appendix B: A Proposed Fit to the K-Shell Emission Cross Section of Copper

Our objective was never to develop our own expression for the K-shell emission cross section but to find a simple expression that we could plug into our calculations; this is most likely the reader's objective, so it appears to be something of a disservice to end with a long list of complex expressions and no clear recommendation. Therefore, we will propose a simple expression for the K-shell emission cross section of copper that gives the best fit to the measurements and that in the limit of strongly relativistic energies has the form indicated by the fast-electron stopping power. Since 77% of the measurements are in the region from threshold to peak, the best fit to them is largely determined by the form of the expression in this region.

A simple expression that reproduces all of the general features and has the desired limiting form is

$$f_0 = \frac{\sigma_0}{\beta^2}\left\{\ln\left[\left(\frac{\gamma+1}{\gamma_B+1}\right)^{1/2}U\right] - \frac{\delta-\delta_B}{2}\right\}, \quad \text{(B1)}$$

where the subscript B indicates quantities evaluated at the binding energy B, rather than the fast-electron kinetic energy E, to give an expression that is identically zero at threshold. An equally valid approach would be to multiply by a function that is zero at threshold and tends to a constant at large energies.

The density-effect correction δ could be calculated either numerically, from tabulated values, or from a fitting formula. An approach that may provide the best means to fit data would be to use a fitting formula and redetermine its parameters by fitting the data. For a number of applications it could be ignored. For simplicity we used Eq. (7), which is intended to have the right form in the strongly relativistic limit and not to cause significant errors at lower energies; it is not a fitting formula. At energies of the order of 1 MeV, it is an underestimate. It will not work for nonconductors and will not work well for lower Z than copper.

Equation (B1) does not give a good fit to the measurements. Since Hombourger's expression gave the best fit to Llovet *et al.*'s data, we tried multiplying f_0 by

$$f_1 = 1 + \sum_{n=1}^{N}\frac{a_n}{U^n}. \quad \text{(B2)}$$

$N = 1$ gave a good fit to Llovet *et al.*'s data and the fit did not improve significantly until $N = 4$, which gave a value of σ_0 that appeared too low (16.95 barns). We also used $N = 1$ to fit all of the measurements and obtained very similar results. The resulting expression for the K-shell emission cross section of copper is

$$\sigma_K = \left(1 - \frac{0.2824}{U}\right)\frac{20.95}{\beta^2}$$

$$\times \ln\left[\left(\frac{U+113.8}{114.8}\right)^{1/2}\frac{57.0098U}{56.9+0.1098U}\right] \text{barns.} \quad \text{(B3)}$$

The resulting macroscopic cross section is plotted along with the measurements in Fig. 135.32, where we have included the $\pm10\%$ absolute error quoted by Llovet *et al.*,[10] imposed a minimum error of $\pm10\%$ on the measurements given by Liu *et al.*,[9] and plotted our fit at the $\pm10\%$ levels. We have not plotted the other expressions in order to emphasize a comparison with the measurements and avoid too many lines. Our proposed fit is in good agreement with the measurements up to and just beyond the peak but agrees only with subsets of the measurements compiled by Liu *et al.*[9] at higher energies, even considering variations of $\pm10\%$, which is also true of all the other expressions. Compared to the other expressions, it lies roughly in the middle of them up to just above the peak, where it clearly gives the best fit to the measurements, gives the highest values near the dip, lies within their range of values between roughly 50 MeV and 2 GeV, and gives the lowest values at higher energies.
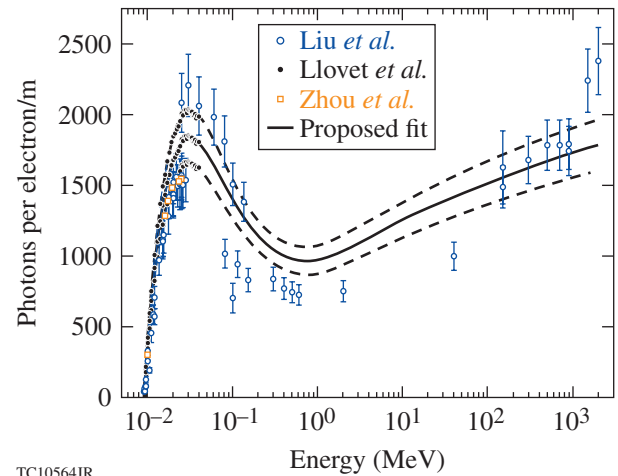

TC10564JR

Figure 135.32
Macroscopic K-shell emission cross sections for solid copper. Circles are measurements compiled by Liu *et al.*[9] with a minimum error of $\pm10\%$ imposed. Dots joined by a solid line are the measurements of Llovet *et al.*;[10] the dots on the dashed lines are these values at $\pm10\%$—their quoted absolute error. Squares are the measurements of Zhou *et al.*[11] The solid line is our proposed fit; dashed lines are the fit at $\pm10\%$.

This approach is good only for fitting data from threshold to peak; f_1 in all the fits was close to one beyond the peak. Further factors should be added that can adjust the depth of the dip and the value of σ_0 in the strongly relativistic limit; it does appear that the dip should be lowered. We have not considered this further because there are only a limited number of measurements with significant differences between them in this region.

REFERENCES

1. M. Tabak *et al.*, Phys. Plasmas **1**, 1626 (1994).

2. S. Gus'kov *et al.*, Phys. Rev. Lett. **109**, 255004 (2012).

3. J. T. Mendonça, J. R. Davies, and M. Eloy, Meas. Sci. Technol. **12**, 1801 (2001).

4. J. R. Davies, Laser Part. Beams **20**, 243 (2002).

5. S. P. Hatchett, C. G. Brown, T. E. Cowan, E. A. Henry, J. S. Johnson, M. H. Key, J. A. Koch, A. B. Langdon, B. F. Lasinski, R. W. Lee, A. J. MacKinnon, D. M. Pennington, M. D. Perry, T. W. Phillips, M. Roth, T. C. Sangster, M. S. Singh, R. A. Snavely, M. A. Stoyer, S. C. Wilks, and K. Yasuike, Phys. Plasmas **7**, 2076 (2000).

6. M. I. K. Santala *et al.*, Phys. Rev. Lett. **84**, 1459 (2000).

7. P. M. Nilson, J. R. Davies, W. Theobald, P. A. Jaanimagi, C. Mileham, R. K. Jungquist, C. Stoeckl, I. A. Begishev, A. A. Solodov, J. F. Myatt, J. D. Zuegel, T. C. Sangster, R. Betti, and D. D. Meyerhofer, Phys. Rev. Lett. **108**, 085002 (2012).

8. K. B. Wharton *et al.*, Phys. Rev. Lett. **81**, 822 (1998); R. B. Stephens *et al.*, Phys. Rev. E **69**, 066414 (2004); K. L. Lancaster, J. S. Green, D. S. Hey, K. U. Akli, J. R. Davies, R. J. Clarke, R. R. Freeman, H. Habara, M. H. Key, R. Kodama, K. Krushelnick, C. D. Murphy, M. Nakatsutsumi, P. Simpson, R. Stephens, C. Stoeckl, T. Yabuuchi, M. Zepf, and P. A. Norreys, Phys. Rev. Lett. **98**, 125002 (2007); J. S. Green *et al.*, Phys. Rev. Lett. **100**, 015003 (2008).

9. M. Liu *et al.*, At. Data Nucl. Data Tables **76**, 213 (2000).

10. X. Llovet, C. Merlet, and F. Salvat, J. Phys. B **33**, 3761 (2000).

11. C.-G. Zhou, Z. An, and Z.-M. Luo, Chin. Phys. Lett. **18**, 759 (2001).

12. A. Kahoul *et al.*, Radiat. Phys. Chem. **80**, 369 (2011).

13. D. Bote and F. Salvat, Phys. Rev. A **77**, 042701 (2008).

14. D. Bote *et al.*, At. Data Nucl. Data Tables **95**, 871 (2009); D. Bote *et al.*, At. Data Nucl. Data Tables **97**, 186 (2011).

15. E. Casnati, A. Tartari, and C. Baraldi, J. Phys. B **15**, 155 (1982).

16. C. Jakoby, H. Genz, and A. Richter, J. Phys. Colloq. **48**, 487 (1987).

17. C. Hombourger, J. Phys. B, At. Mol. Opt. Phys. **31**, 3693 (1998).

18. C.-H. Tang *et al.*, Chin. Phys. Lett. **18**, 1053 (2001).

19. A. K. F. Haque *et al.*, Phys. Rev. A **73**, 012708 (2006).

20. A. K. F. Haque *et al.*, Eur. Phys. J. D **42**, 203 (2007).

21. B. Gstir *et al.*, J. Phys. B **34**, 3377 (2001).

22. Z. An, Z. M. Luo, and C. Tang, Nucl. Instrum. Methods Phys. Res. B **179**, 334 (2001).

23. A. K. F. Haque *et al.*, Int. J. Quantum Chem. **109**, 1442 (2009).

24. A. K. F. Haque *et al.*, J. Phys. B **43**, 115201 (2010).

25. J. P. Santos, F. Parente, and Y.-K. Kim, J. Phys. B: At. Mol. Opt. Phys. **36**, 4211 (2003).

26. M. Guerra *et al.*, Int. J. Mass Spectrom. **313**, 1 (2012).

27. M. Gryziński, Phys. Rev. **138**, A322 (1965).

28. J. H. Scofield, Phys. Rev. A **18**, 963 (1978).

29. H. Kolbenstvedt, J. Appl. Phys. **46**, 2771 (1975).

30. Md. R. Khan and M. Karimi, X-Ray Spectrom. **9**, 32 (1980); M. Ertuğrul *et al.*, J. Phys. B **34**, 909 (2001); J. P. Marques, F. Parente, and P. Indelicato, J. Phys. B **34**, 3487 (2001).

31. H. K. Chung *et al.*, High Energy Density Phys. **1**, 3 (2005).

32. H. O. Wyckoff, *ICRU Report*, International Commission on Radiation Units and Measurements, Inc., Bethesda, MD (1984).

33. ESTAR, accessed 16 May 2013, http://physics.nist.gov/PhysRefData/Star/Text/ESTAR.html.

34. R. M. Sternheimer, M. J. Berger, and S. M. Seltzer, At. Data Nucl. Data Tables **30**, 261 (1984).

35. S. Atzeni, A. Schiavi, and J. R. Davies, Plasma Phys. Control. Fusion **51**, 015016 (2009).

36. EGSnrc Monte Carlo code, accessed 17 May 2013, http://www.nrc-cnrc.gc.ca/eng/rd/mss/index.html.

37. XCOM, accessed 16 May 2013, http://physics.nist.gov/PhysRefData/Xcom/html/xcom1.html.

38. A. Kahoul *et al.*, Radiat. Phys. Chem. **80**, 369 (2011).

39. PSTAR, accessed 16 May 2013, http://physics.nist.gov/PhysRefData/Star/Text/PSTAR.html.

40. J. P. Desclaux, At. Data Nucl. Data Tables **12**, 311 (1973).

Fracture Mechanics of Delamination Defects in Multilayer Dielectric Coatings

Introduction

Multilayer-dielectric (MLD) thin-film coatings are widely used to produce high-quality optical components, having diverse applications ranging from Bragg mirrors to polarizer optics. Hafnia (HfO_2)–silica (SiO_2) multilayers are frequently used to fabricate MLD diffraction gratings for high-intensity laser systems because of the inherently high laser-damage resistance of this material combination.[1,2] The laser-damage thresholds of MLD gratings are typically well below those of the constituent dielectric materials themselves, however, because surface texture, contamination, and microscopic defects can dramatically affect laser-damage resistance.[3–9]

Multilayer-dielectric coatings are susceptible to a variety of unique defects and phenomena arising from fabrication and storage, including nodules,[5,6] pits,[4,7] absorption of volatilized contaminants from vacuum,[10] and optical instabilities resulting from moisture penetration into porous oxide layers from humid air.[11,12] Patterned optical components such as MLD diffraction gratings require aggressive cleaning operations to remove photoresist and other lithographic residues. Unfortunately, some of the most-effective cleaning methods—usually involving high temperatures and strong acids or bases—can themselves induce chemical degradation and thermal stresses in the coating, leading to delamination and defects.[9,13]

Micron-scale delamination defects have been observed on MLD coatings after exposure to a hot acid piranha solution—a mixture of hydrogen peroxide and sulfuric acid that is commonly used to clean MLD gratings.[9,14–16] Delamination defects are distinguished by a characteristic pattern of crescent-shaped fractures in the coating, with the layers uplifted at the defect site. Because these features interrupt the continuity of the MLD surface, they may cause electric-field enhancement and reduced laser-damage thresholds. While we have been able to largely avoid the production of cleaning defects by reducing piranha solution temperatures to 40°C (Ref. 9), a thorough understanding of the causes and formation mechanism of delamination defects will be important in the continued development of cleaning technologies.

We investigate the causes of delamination defects and describe a mechanism for the deformation and failure of the MLD coating in response to hydrogen peroxide in the cleaning solution. In the proposed mechanism, we assume a localized pressure buildup in a small volume of acid piranha trapped in the coating that drives the propagation of an interface crack in the multilayer. The associated fracture mechanics problem is that of a pressure-loaded blister in a multilayer material—an extension of the pressurized circular blister treated by Jensen.[17] The appropriate length scale for the multilayer blister problem is explored. Finally, the predicted path of a crack propagating through the MLD coating layers is compared with the observed cross-sectional geometry of a defect.

Materials and Methodology

The MLD samples used in this study were 3-mm-thick, 100-mm-diam BK7 substrates coated by electron-beam evaporation in a high reflector design (a modified quarter-wave stack of high- and low-index layers) with an extra-thick top layer.[18] The coating comprised 28 layers of alternating hafnia (HfO_2) and silica (SiO_2) with a bottom layer of HfO_2 and top layer of SiO_2. The total coating thickness was 5.0 μm, with typical layer thicknesses of 190 nm for the silica layers and 142 nm for the hafnia layers. Samples were not patterned or etched. For cleaning experiments, each sample was broken into eight wedges.

Defects were generated by submerging the samples in the acid piranha solution. For each test, a 400-mL acid piranha solution was prepared and cooled to room temperature. The ratio of sulfuric acid to hydrogen peroxide was either two parts H_2SO_4 to one part H_2O_2 (2:1 piranha) or five parts H_2SO_4 to one part H_2O_2 (5:1 piranha), depending on the test. After preparation, the piranha solution was used within 24 h to limit degradation. Except as noted, samples were submerged into the piranha solution at room temperature, heated to the prescribed soak temperature over a ramp period of 30 min, held at the soak temperature for the specified duration, and then cooled to room temperature over 30 min using an ice bath. After the MLD samples were removed from the solution, they were rinsed with de-ionized water and dried using a filtered nitrogen

gun. Samples were inspected by a Leica Nomarski microscope after the piranha treatment and evaluated for defect formation.

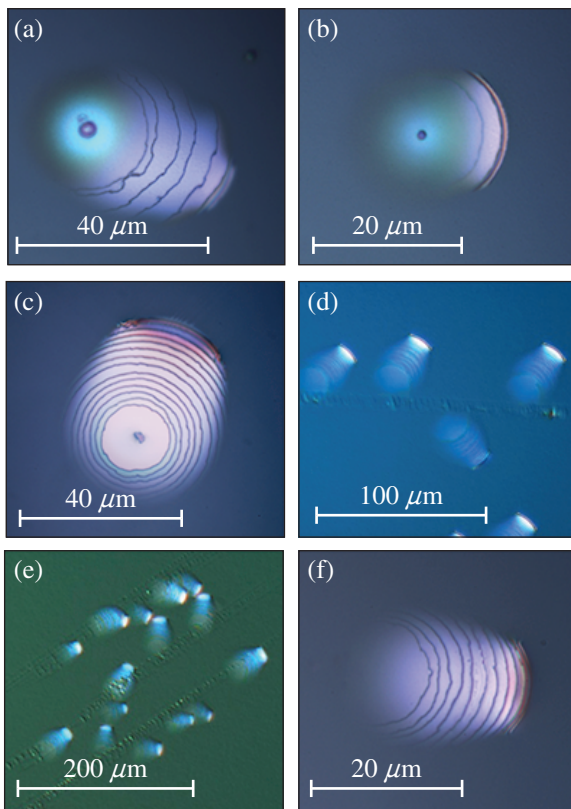## Characterization of the Delamination Defect

1. Microscopy

Nomarski micrographs of representative delamination defects are shown in Fig. 135.33. The piranha treatments for the samples shown are specified in the captions. Delamination defects had typical dimensions of 20 to 50 μm and featured a characteristic array of circular- and crescent-shaped cracks radiating out from an initiating point, typically an existing surface feature. Some defects were associated with nodules, as shown in Figs. 135.33(a) and 135.33(b), while other defects were paired with pieces of debris, as in Fig. 135.33(c), or formed

Figure 135.33
Nomarski micrographs of representative delamination defects: [(a,b)] defects associated with nodules; (c) a defect associated with a piece of surface debris; [(d,e)] defects that formed along scratches; and (f) a defect that was not observed with any apparent surface feature. Defects were generated by submerging the samples in 2:1 piranha, with the following temperature treatments: [(a,b)] 90°C soak for 2 h with 30-min heating and cooling ramps; (c) sample submerged at 70°C and cooled to room temperature over 2 h; [(d,e)] samples submerged at 90°C and cooled over 30 min; and (f) sample submerged at 70°C and cooled over 30 min.

in groups along scratches, as in Figs. 135.33(d) and 135.33(e). Occasionally, delamination defects were identified that seemed not to be linked to any other artifact, as shown in Fig. 135.33(f). Because we have only rarely observed defects in this final category, they may be connected with small features that simply could not be resolved in the light microscope. Defects sometimes involved many coating layers, as in Figs. 135.33(a) and 135.33(c), or just a few coating layers, as in Fig. 135.33(b).

Because the oxide layers of the coating are transparent to white light, cracks in each layer are visible in the optical micrographs of Fig. 135.33. The approximate depths of cracks in the multilayer were determined by recording the z position of best focus and, in all cases, the crack nearest to the "initiating" artifact was located in the deepest coating layer involved in the defect. The crack front farthest from this central artifact was at the surface layer, suggesting that delamination defects nucleate within the coating, not at the surface.

Defects were examined in a scanning electron microscope (SEM) to further probe their geometries. Because the SEM "sees" only the sample's surface, a top-down SEM image [Fig. 135.34(a)] revealed only the arc-shaped crack in the uppermost coating layer. To examine the defect's cross section, focused-ion-beam (FIB) milling was used to cut a trench in the MLD coating, bisecting a delamination defect. A thin layer of platinum was locally deposited immediately prior to milling to enable the beam to cut a clean cross section instead of gradually eroding the multilayer. The resulting cross-sectional view, shown in Fig. 135.34(b), reveals a zigzagging crack in the upper 24 layers of the coating (the bottom two layer pairs were apparently unaffected in this particular case). The uplifting of the coating at the defect site and the separation between crack faces explain the "bright" appearance of delamination defects in the optical microscope images of Fig. 135.33. The uplifting of the coating also explains previous nanoindentation results showing that delamination defects are more compliant than the surrounding coating.[19] The crack path revealed by FIB will be treated in detail in **Fracture Mechanics** (p. 192).

2. Causes of Delamination Defects

A screening experiment was carried out to investigate the factors contributing to defect formation during piranha cleaning. The experiment was designed using JMP® statistical software and design-of-experiments (DOE) methodology to randomize trial order and to choose appropriate factor levels. The effects of five parameters were studied: (1) the age of the MLD coating at the time of cleaning (because the intrinsic coating stress level has been shown to vary with time);[20–23] (2) the
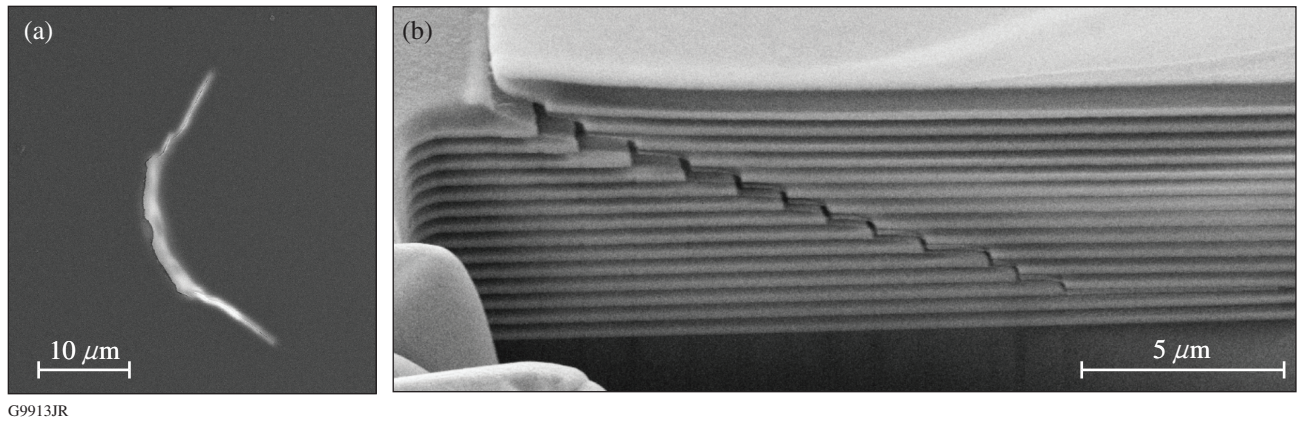
G9913JR

Figure 135.34
Scanning electron microscope (SEM) images showing (a) a delamination defect observed from a bird's eye view, showing its surface structure and (b) a defect bisected by focused-ion-beam (FIB) milling and viewed in cross section.

ratio of sulfuric acid to hydrogen peroxide (piranha ratio) in the acid piranha solution; (3) the solution temperature during the soak period; (4) the soak duration, not including time spent ramping up to the soak temperature or cooling to room temperature; and (5) whether or not the sample was heat shocked by submerging it directly into hot piranha at the soak temperature (rather than slowly heated to the soak temperature over 30 min). Defect density on the MLD sample after cleaning (number of delamination defects per unit surface area) was used as the response for the experiment. Analysis-of-variances (ANOVA) results from the experiment are presented in Table 135.II.

Assigning a confidence limit of 95%, the piranha ratio was the only factor judged statistically significant in this experiment (denoted by asterisks in Table 135.II). The samples treated with 2:1 piranha had defect densities that were, on average, an order-of-magnitude higher than the samples cleaned with 5:1 piranha, indicating that hydrogen peroxide plays an important role in cleaning-induced defect formation. Anecdotally, this result is supported by the fact that we have regularly observed delamination defects on MLD samples exposed to acid piranha (and on samples exposed to 30% hydrogen peroxide) but never on samples exposed to non-peroxide-containing chemicals that

Table 135.II: ANOVA results for the delamination defect screening experiment.

Factor	Level	Mean Defect Density (defects/cm^2)	Sum of Squares (SS)	Mean Square (MS)	Degrees of Freedom (dof)	F Ratio	Prob > F (p value)
Coating age	2 weeks	1.92	9.57	4.78	2	0.96	0.39
	6 weeks	1.47					
	12 weeks	0.95					
Piranha ratio ($H_2SO_4:H_2O_2$)	5:1	0.24	68.57	68.57	1	13.74	0.001***
	2:1	2.76					
Soak temperature	50°C	1.18	2.09	1.05	2	0.21	0.81
	70°C	1.44					
	90°C	1.69					
Soak time	0 min	0.98	13.31	6.66	2	1.33	0.28
	30 min	1.23					
	60 min	2.12					
Heat shock	Shocked	1.06	7.56	7.56	1	1.52	0.23
	Not shocked	1.82					
Error estimate	–	–	154.59	4.99	31	–	–

***Significance at the $p \leq 0.001$ level.

we have tested, including sulfuric acid and a variety of solvents and commercial photoresist strippers. Trends in the data that warrant further investigation also suggest connections between increased defect formation and high piranha temperatures, long soak duration, and freshly deposited MLD coatings.

3. The Process of Defect Formation

Typically, delamination defects are observed immediately after piranha cleaning: by the time a sample can be rinsed, dried, and transferred to the microscope, all cleaning-induced defects have already formed. In one experiment, however, the real-time formation of delamination defects was witnessed firsthand during a routine inspection of an MLD sample approximately 45 min after removal from piranha solution.

Frames captured from a video of defect formation, showing a 75- × 75-μm area as viewed in Nomarski, are shown in Fig. 135.35. The formation process took about 20 s. The defect grew with a round shape at first, shown in Figs. 135.35(a)–135.35(c), then expanded to an oblong shape as it broke through the layers of the MLD [Figs. 135.35(d) and 135.35(e)]. The defect had nearly reached its final size about 3 s after it began to form and reached a stable geometry [Fig. 135.35(h)] after about 20 s. The bright spot in the lower part of Figs. 135.35(a)–135.35(d) is another smaller artifact. At the 3-s mark [Fig. 135.35(e)], the newly formed defect merged with this small artifact.

Figure 135.36 shows the evolution of a 160- × 140-μm area surrounding the defect of Fig. 135.35. Two new defects formed in this region: one appearing in Fig. 135.36(b) and another in Fig. 135.36(c). The just-formed defects "flickered" distinctly and appeared to be liquid filled, with a pulsating effect pos-
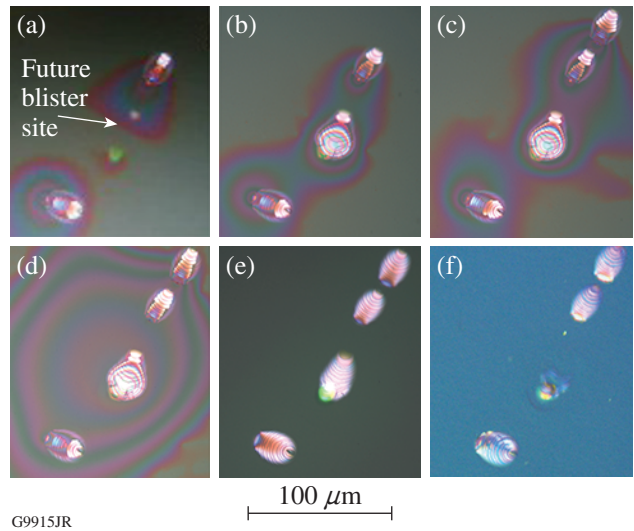

G9915JR

Figure 135.36
Nomarski micrographs of a 160- × 140-μm region containing the defect seen in Fig. 135.35. Images were captured (a) 45 min, (b) 60 min, (c) 61 min, (d) 100 min, (e) 48 h, and (f) 6 months after the sample was removed from the piranha solution.

sibly caused by rapid evaporation. The defects were initially surrounded by regions of trapped fluid, which moved about and agglomerated into larger areas over time [see Figs. 135.36(a)–135.36(d)]. These features may be similar to the "moisture penetration patterns" described by Macleod et al.,[11] involving the incorporation of fluid into the porous structure of oxide layers.

Several hours after piranha cleaning, the trapped liquid had escaped from the MLD coating and the flickering had stopped. A difference in optical thickness remained, leading to the bright appearance of mature delamination defects in Nomarski microscopy [Fig. 135.36(e)]. Interestingly, when the MLD

G9914JR
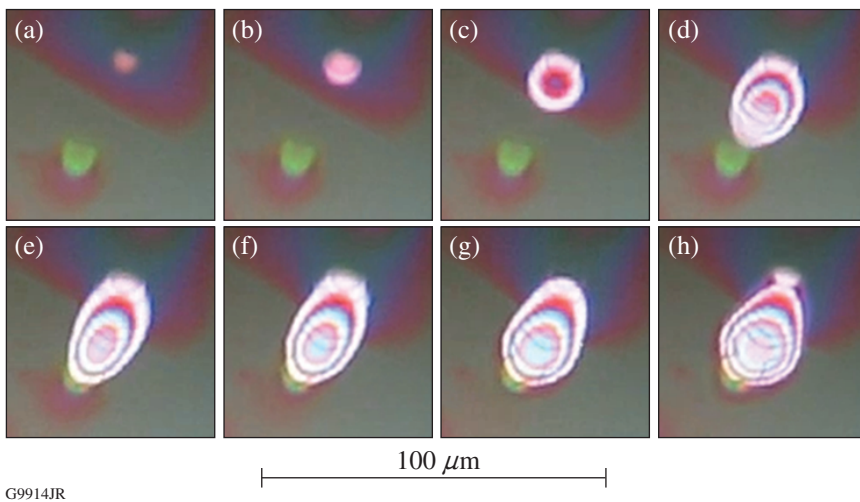
Figure 135.35
A series of 75- × 75-μm frames captured from a Nomarski microscope video of an individual delamination defect's formation approximately 45 min after a 2-h submersion in 2:1 piranha at 90°C. Images of the defect's development were captured (a) 0 s, (b) 2.0 s, (c) 2.6 s, (d) 2.7 s, (e) 3.0 s, (f) 6.0 s, (g) 11.0 s, and (h) 20.0 s after it began to form.

sample was re-inspected several months later [Fig. 135.36(f)], the defect of Fig. 135.35 had nearly disappeared, possibly after collapsing into optical contact. The smaller, overlapping defect was still apparent.

A Mechanism for Delamination Defect Formation

We propose a mechanism to explain the primary features of delamination defects presumed from experimental observations; namely, that (1) hydrogen peroxide is essential to defect formation; (2) delamination defects are typically associated with an existing flaw that interrupts the coating; (3) defects are initially filled with liquid; (4) the crack in the multilayer advances in a zigzagging fashion upward toward the surface; (5) separation of crack faces leads to a permanent uplifting of the coating and a change in optical thickness at the defect site; but (6) delamination defects can "heal" by collapsing into optical contact.

A proposed mechanism for defect formation that satisfies all of the above requirements is shown schematically in Fig. 135.37. First, acid piranha penetrates into the MLD coating [Fig. 135.37(a)] through a large pore, small scratch, or defect (not shown), and a small volume of piranha becomes trapped in the coating at an interface where adhesion has locally failed (between layers or between substrate and coating). Pressure builds up at this location because of the evolution of oxygen

gas from hydrogen peroxide in the trapped piranha, and the MLD layers deform into a circular blister to accommodate the increasing pressure [Fig. 135.37(b)]. Once the critical stress for fracture is reached in the deforming MLD, crack propagation occurs. The crack may initially propagate along the interface (increasing the debond area), but to explain the characteristic fracture pattern, the crack must eventually kink upward into the multilayer [Fig. 135.37(c)]. The crack propagates through the MLD coating to the surface, where accumulated oxygen gas escapes, relieving built-up pressure and collapsing the inflated blister structure. The final defect geometry includes a gap between crack faces [Fig. 135.37(d)], but if the layers later collapse into contact, eliminating air gaps, the defect may appear to have "healed."

Figure 135.38 shows hypothesized cross-sectional geometries of two observed delamination defects. Twelve arc-shaped cracks, labeled A–L, were counted in the Nomarski micrograph of defect (a). This defect likely initiated between layers 4 (silica) and 5 (hafnia), and each observed arc-shaped crack involved one hafnia/silica layer pair. In defect (b), 14 cracks (A–N) were identified, consistent with a substrate-initiated blister with fracture through all 28 layers. At least five of the 14 cracks (A–E) were circular. Cracks in the upper layer pairs (F–N) were arc shaped with successively shorter arc lengths. The hypothesized geometry in this case is similar to (a), but with complete circular

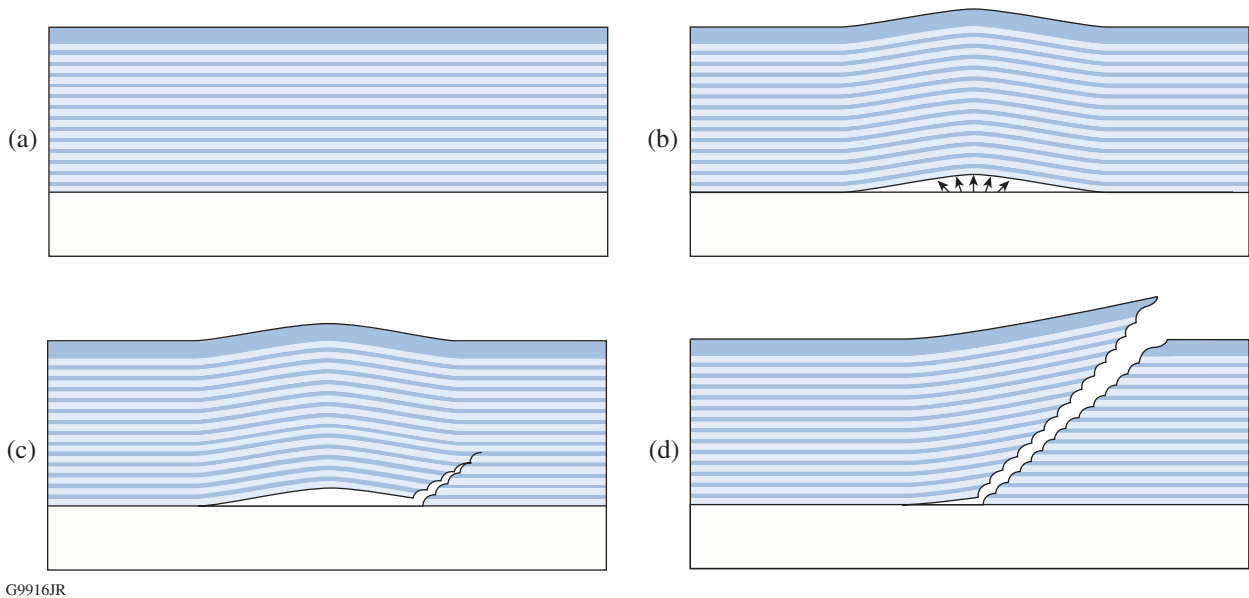
G9916JR

Figure 135.37
Schematic illustrating the hypothesized delamination defect formation mechanism: (a) undisturbed MLD coating, (b) initial pressure development in coating and deformation, (c) kinked fracture at edge of pressurized blister, and finally (d) propagation of the crack to MLD surface. Light bands represent hafnia layers in the coating, while dark bands represent silica layers.
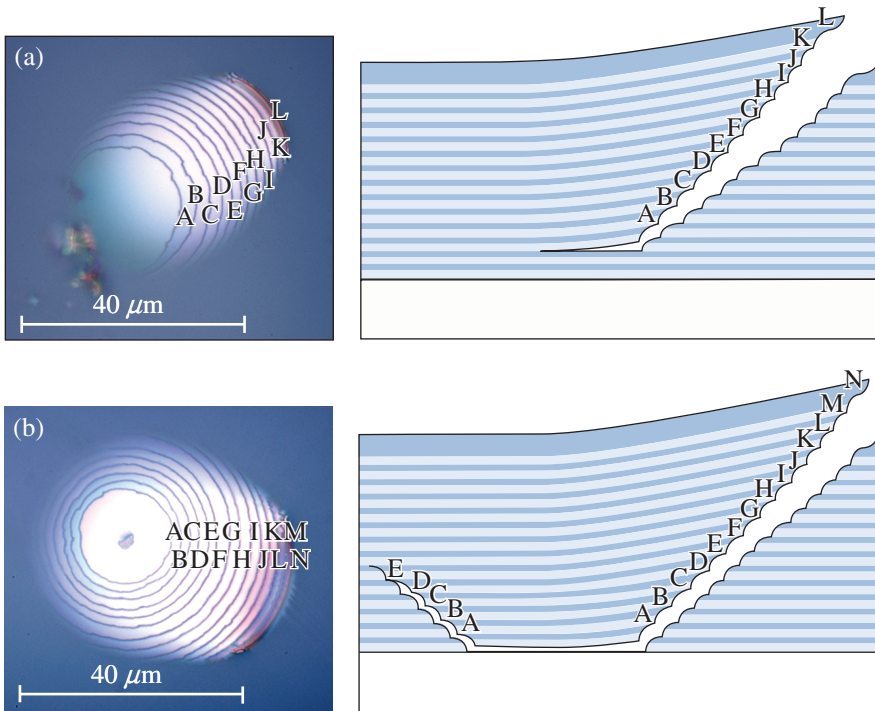
Figure 135.38
Nomarski micrographs of two delamination defects with schematics showing hypothesized cross-sectional geometries: (a) defect initiated between the second and third MLD layer pairs, with arc-shaped cracks; (b) substrate-initiated defect with fracture through all 14 layer pairs. Fracture in the bottom few layers occurred as circular cracks at the blister's perimeter, while cracks in upper layers were arc shaped.

cracks in the initial few layers with an asymmetrical geometry developing as the crack propagated upward.

The proposed mechanism requires that a small volume of liquid becomes trapped between layers of the MLD coating. The original entry path must not be a viable path for the escape of gas or liquid; otherwise, high pressures could not develop in the cavity because the oxygen gas evolved from the decomposition of acid piranha could simply travel out of the volume to relieve pressure. Considering the multilayer structure of the thin-film coating, we suggest the coefficient-of-thermal-expansion mismatch between hafnia and silica layers as an explanation: if the MLD layers deform or shift with respect to each other during elevated temperature cleaning, a path to the surface through adjacent layers could become blocked, and pressure could develop freely in a void containing trapped acid piranha.

Fracture Mechanics

1. Material Properties of Dielectric Layers and MLD Coating

The properties of thin films can be sensitive to the deposition technique,[24,25] and therefore it can be unwise to assume thin-film properties for one coating based on data from a different coating, unless it is known that the deposition method was the same. Nanoindentation of single-layer hafnia and silica films was carried out to accurately estimate the elastic moduli of the

MLD layers. Cross sections of the films tested are shown in Fig. 135.39. The thicknesses of the single-layer films (135 nm for hafnia and 180 nm for silica) were similar to the thicknesses of those layers in the multilayer coating, and the deposition technique was the same as that used for the MLD coating layers. To avoid substrate effects in the nanoindentation measurements, mechanical properties were assessed using data from indenter penetration into only the top 10% to 20% of the total film thickness. The average Young's moduli calculated for the films were $E_{haf} = 128\pm12.5$ GPa (average $\pm$ standard deviation of four measurements) for hafnia and $E_{sil} = 92\pm5$ GPa for silica. These measurements were within ~25% of moduli reported by Thielsch *et al.*[24] for thin-film hafnia (deposited by reac-
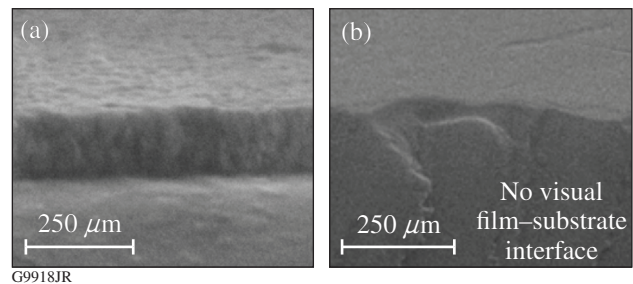
Figure 135.39
SEM images showing cross sections of oxide monolayers used in nanoindentation experiments: (a) a 160-nm layer of hafnia and (b) a 180-nm layer of silica. There was no visible interface between the substrate and the amorphous silica film.

tive evaporation) and silica (deposited by plasma ion–assisted deposition). Poisson ratio ν for the films was estimated from reported values,[26,27] and shear and bulk moduli μ and B were calculated from E and ν using the relations $\mu = E/2(1 + \nu)$ and $B = E/3(1-2\nu)$, respectively.

MLD coating properties were estimated from the single-layer properties determined by nanoindentation experiments. Upper and lower limits on shear modulus and bulk modulus were calculated by the rule of mixtures,

$$\mu_{MLD}^{upper} = \mu_{haf} V_{haf} + \mu_{sil} V_{sil},$$
$$B_{MLD}^{upper} = B_{haf} V_{haf} + B_{sil} V_{sil}, \tag{1}$$

and

$$\frac{1}{\mu_{MLD}^{lower}} = \frac{V_{haf}}{\mu_{haf}} + \frac{V_{sil}}{\mu_{sil}},$$
$$\frac{1}{B_{MLD}^{lower}} = \frac{V_{haf}}{B_{haf}} + \frac{V_{sil}}{B_{sil}}, \tag{2}$$

where V_{haf} and V_{sil} are the volume fractions of hafnia and silica ($V_{haf} = 0.39$ and $V_{sil} = 0.61$ for the MLD used in this work). The calculated lower and upper limits on bulk modulus were 58.4 GPa and 63.4 GPa, respectively, and the limits on shear modulus were 44.5 GPa and 45.2 GPa, respectively. These bounds were averaged to estimate the bulk and shear moduli for the multilayer. Poisson ratio and Young's modulus for the MLD were calculated from these moduli using the relations

$$\nu = \frac{3B-2\mu}{6B+2\mu}, \quad E = 2\mu(1+\nu). \tag{3}$$

Bulk properties for the BK7 substrate came from Schott product literature.[28] Material properties are summarized in Table 135.III.

2. Contributions of Pressure and Intrinsic Stress to Blister Deformation

In **A Mechanism for Delamination Defect Formation** (p. 191), it was hypothesized that the delamination defect is initiated by pressure developed in a small, disk-shaped volume of acid piranha trapped in the coating. We therefore modeled the blister (prior to fracture) as a circular plate of thickness h and radius R, subjected to an internal pressure p_c and an equibiaxial intrinsic stress σ, and fixed to a thick substrate at its edges ($r = R$, where r is the radial coordinate), as shown in Fig. 135.40. The residual stresses in an evaporated MLD coating can be significant, and the pressure p_c evolved from piranha decomposition might not be large, so the effects of both loadings are considered in this analysis. The normal displacements of the plate are given by $w(r)$.
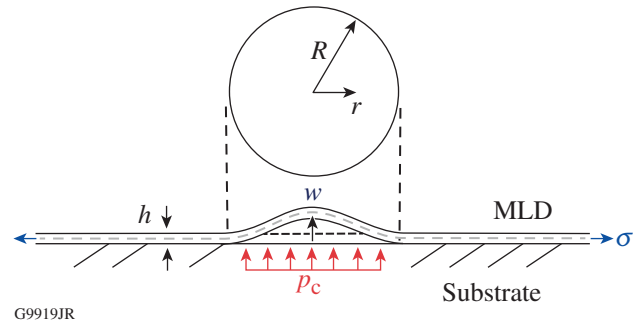

G9919JR

Figure 135.40
Schematic of a pressurized blister in an MLD film with a residual film stress.

Jensen[17] showed that, in nondimensional form, the von Kármán plate equations for the situation shown in Fig. 135.40 can be written as

$$\frac{1}{12(1-\nu^2)} \rho \frac{d}{d\rho}\left[\frac{1}{\rho}\frac{d}{d\rho}(\rho\xi)\right] - \overline{\varphi}\xi + \frac{p_c R^4}{2Eh^4}\rho^2 = \frac{\sigma R^2}{Eh^4}\xi,$$

$$\rho \frac{d}{d\rho}\left[\frac{1}{\rho}\frac{d}{d\rho}(\rho\overline{\varphi})\right] + \frac{1}{2}\xi^2 = 0, \tag{4}$$

$$\xi(\rho) = -\frac{d\overline{w}}{d\rho}, \quad \overline{\varphi}(\rho) = \frac{R\varphi}{Eh^3}, \quad \varphi = \frac{d\Phi}{dr},$$

Table 135.III: Material properties used in the fracture mechanics analysis.

Material	Young's Modulus E (GPa)	Poisson Ratio ν	Shear Modulus μ (GPa)	Bulk Modulus B (GPa)
BK7 (bulk)	82	0.21	33.9	47.1
SiO$_2$ (thin film)	95	0.17	40.6	48.0
HfO$_2$ (thin film)	130	0.25	52.0	86.7
MLD coating	108	0.20	44.7	60.6

where ν and E are the Poisson ratio and Young's modulus of the thin-film coating, Φ is the Airy stress function, and ρ and $\overline{w}$ are nondimensional quantities defined by $\rho = r/R$ and $\overline{w} = w/h$. For plate behavior, the appropriate boundary conditions are zero slope at the center of the blister, no rotations or displacements at the fixed edges, and $\overline{w}$ bounded everywhere.

If the nonlinear $\overline{\varphi}\xi$ term in Eq. (4) can be neglected, the first equation can be uncoupled from the second, and the resulting ordinary differential equation can be written as

$$\rho^2 \xi'' + \rho \xi' - (S\rho + 1)\xi = -P\rho^3, \qquad (5)$$

where prime indicates differentiation with respect to ρ. Two new nondimensional quantities, $S = 12(1-\nu^2)\sigma R^2 / Eh^2$ (residual stress term) and $P = 6(1-\nu^2)p_c R^4 / Eh^4$ (pressure term), were introduced for convenience. In the special case of negligible residual stresses, $S = 0$ and Eq. (5) reduces to an equidimensional Euler–Cauchy equation. Applying the boundary conditions, the solution for the $\sigma = 0$ case is

$$\xi(\rho) = -\frac{P}{8}\left(\rho^3 - \rho\right) \qquad (6)$$

and

$$\overline{w}(\rho) = -\int \xi \, d\rho = \frac{P}{32}\left(\rho^4 - 2\rho^2 + 1\right). \qquad (7)$$

Returning to the general case [Eq. (5)], it can be shown that the solution for $\xi(\rho)$ can be given in terms of modified Bessel functions of the first and second kinds and the Meijer G function. The solution $\xi(\rho)$ could not be readily integrated to find the blister deflections $\overline{w}(\rho)$ in closed form. An approximate solution was found by expanding all products in the expression for $\xi(\rho)$ and integrating term by term. The integrals of all but one term in the expanded form of $\xi(\rho)$ could be expressed in standard mathematical functions, and the remaining term was approximated by a five-term power series and integrated. The resulting approximation for $\overline{w}(\rho)$ agreed with the closed-form solution [Eq. (7)] for $\sigma \longrightarrow 0$. A few specific cases are now considered.

Geometrical and material properties were selected as follows: $E = 108$ GPa and $\nu = 0.20$ (see Table 135.III), $h = 5$ μm (the thickness of the MLD coating), and $R = 20$ μm (estimated by measuring the diameter of the first fracture ring in micrographs of typical delamination defects, as shown in Fig. 135.41).

It was difficult to accurately determine the residual stress σ in the coating because intrinsic stresses vary with deposition parameters, coating age, storage environment, and other factors. Based on measurements of similar coatings,[21–23] the residual stress was expected to be tensile and in the range of $\sigma = 0$ to 150 MPa. We have not considered compressive coatings (typical of energetic-deposition methods). The pressure developed in the blister p_c was also unknown, but we estimated that the upper limit on p_c (for the case of the irreversible decomposition reaction $2H_2O_2 \longrightarrow 2H_2O + O_2$ going to completion in a closed volume) is 254 MPa for a reaction temperature of 60°C, assuming ideal gas behavior for the evolved oxygen gas and incompressibility for water and peroxide; therefore, we consider blister pressures in the range of $p_c = 3$ MPa to 200 MPa.
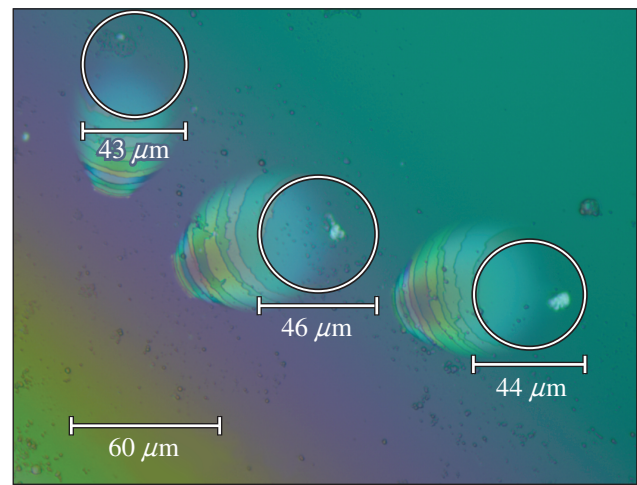
G9920JR

Figure 135.41
Measurement of blister diameter.

Figure 135.42 shows blister deformations resulting from several values of internal pressure p_c. The solid curves show the deformations for an intrinsic stress level of 150 MPa, while the dashed curves show the zero-intrinsic stress case [that is, the simple solution in Eq. (7)]. The inset plot shows the 3-MPa case, which is difficult to resolve in the larger plot, with the axis limits reset to fit the data. Blister pressure had a profound effect on the magnitude of deformations. Blister pressures in the range of 3 to 200 MPa resulted in maximum blister displacements differing by two orders of magnitude: 6-nm maximum displacement for $p_c = 3$ MPa and 400 nm for $p_c = 200$ MPa. In contrast, the effect of residual stress was small, with the difference in displacements for the $\sigma = 0$ and the $\sigma = 150$-MPa cases never more than 4%. This is not surprising given that the stress parameter is $S = 0.26$ for the $\sigma = 150$-MPa case, i.e.,
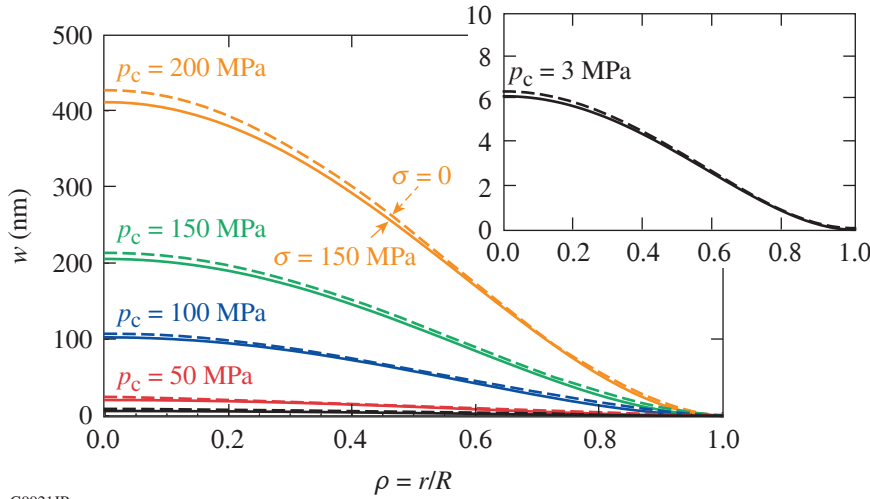
Figure 135.42
Dependence of blister deformations on internal blister pressure for intrinsic coating stresses of zero (dashed curves) and 150 MPa (solid curves). Inset plot shows a larger view of the $p_c = 3$-MPa curves.

small. Note from Eq. (7) that the blister deformation is linear in the pressure p_c.

3. Prediction of Crack Path in Multilayer Coating and Length-Scale Considerations

In the previous section, we considered a pre-existing circular debond (interface crack)—that is, we assumed that the MLD coating was not adhered to the substrate at the blister site, and the coating was free to deflect in response to pressure. To explain the characteristic fracture pattern, the interfacial crack must propagate in response to the pressure loading. If energetically favorable, it is possible for the crack to propagate at first along the interface, growing the blister to a larger diameter, but eventually the interface crack must propagate to the surface by kinking upward into the multilayer.

For an interface crack between two dissimilar materials, the ratio of the energy release rates for the kinked crack $\mathcal{G}$ and the crack advancing in the interface $\mathcal{G}_0$ is given by[30]

$$\frac{\mathcal{G}}{\mathcal{G}_0} = \frac{|c|^2 + |d|^2 + 2\,\mathrm{Re}\left[cd\exp(2i\overline{\psi})\right]}{q^2},$$

$$q = \sqrt{\frac{1-\beta^2}{1+\alpha^2}}, \quad \overline{\psi} = \psi + \varepsilon \ln(a/h),$$

(8)

where $\mathrm{Re}(x)$ gives the real part of x. The mode mixity angle $\psi = \tan^{-1}\left(K_1/K_2\right)$ describes the crack loading, where K_1 and K_2 are the mode-1 (opening) and mode-2 (shearing) stress-intensity factors, respectively. The corrected $\overline{\psi}$ includes a term that depends on the problem length scale a/h and the bimaterial constant ε. The quantities c, d, and q are dimensionless quanti-

ties that depend on the material combination and crack kink angle. The Dundurs material moduli parameters α and β and bimaterial constant ε are defined by[31,32]

$$\alpha = \frac{\mu_1(1-\nu_2) - \mu_2(1-\nu_1)}{\mu_1(1-\nu_2) + \mu_2(1-\nu_1)},$$

$$\beta = \frac{1}{2}\left[\frac{\mu_1(1-2\nu_2) - \mu_2(1-2\nu_1)}{\mu_1(1-\nu_2) - \mu_2(1-\nu_1)}\right],$$

(9)

$$\varepsilon = \frac{1}{2\pi}\ln\left(\frac{1-\beta}{1+\beta}\right),$$

where μ_1, ν_1, and μ_2, ν_2 are the shear moduli and Poisson ratios of materials 1 and 2, respectively. Note that the material mismatch parameters α, β, and ε vanish in the homogeneous case (material 1 = material 2). We take material 1 to be the substrate and material 2 to be the coating, such that the interface crack either continues along the material 1/material 2 interface or kinks upward into material 2 with crack length a at kink angle ω, as illustrated in Fig. 135.43. If the interface crack is located between MLD layers rather than between the substrate and the coating, the layers beneath the crack are grouped with the substrate as a single material, and the partial multilayer
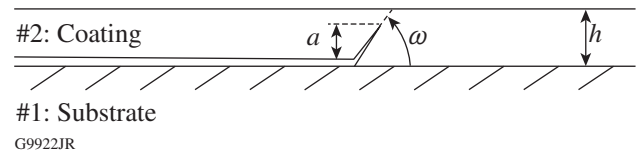

Figure 135.43
Geometry of kinked crack.

above the crack is treated as material 2. Mismatch parameters α, β, and ε for relevant material combinations are shown in Table 135.IV.

Table 135.IV: Values for the Dundurs parameters α and β and bimaterial modulus ε.

Material 1	Material 2	α	β	ε
BK7	MLD coating	−0.13	−0.04	0.01
BK7	HfO_2	−0.23	−0.09	0.03
HfO_2	SiO_2	0.17	0.10	−0.03
SiO_2	HfO_2	−0.17	−0.10	0.03

The ratio of the energy release rates for the kinked crack and crack advancing in the interface $\mathcal{G}/\mathcal{G}_0$ is plotted versus kink angle for several values of $\overline{\psi}$ in Fig. 135.44 for the case of a BK7 substrate with a hafnia/silica MLD coating. Parameters c and d were estimated from the tabulated numerical data of He and Hutchinson[33] using linear interpolation. Note that, excepting the case of $\overline{\psi} = 0$ (corresponding to a pure mode-1 crack), a local maximum of $\mathcal{G}/\mathcal{G}_0$ exists for a nonzero value of ω, interpreted as an energetically preferred kink angle. The preferred kink angle ω_p increases with increasingly negative $\overline{\psi}$, corresponding to a greater mode-2 loading contribution. The specific value of ω_p can be determined if $\overline{\psi}$ is known.

For the case of a pressure-loaded blister with small p_c, the uncorrected mode mixity angle ψ can be expressed as the

Legend:
— $\overline{\psi} = 0°$
– – $\overline{\psi} = -15°$
–·– $\overline{\psi} = -30°$
······ $\overline{\psi} = -60°$
- - - $\overline{\psi} = -80°$
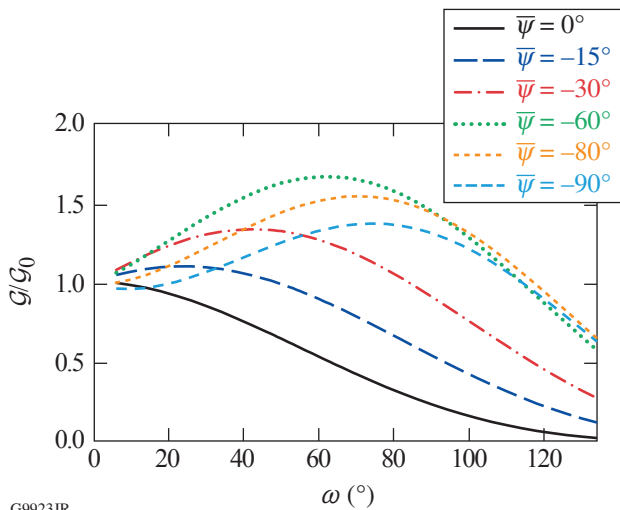– – $\overline{\psi} = -90°$

G9923JR

Figure 135.44
Relationship between energy-release rate ratio $\mathcal{G}/\mathcal{G}_0$ and kink angle for several mode mixity angles for the BK7/MLD coating material combination.

solution to $\tan(\psi) = -\cot(\gamma)$, where $\gamma = \gamma(\alpha, \beta, \eta)$ is a function of the Dundurs parameters and a geometrical parameter $\eta = h/H$ (Ref. 32). When the substrate thickness H is much larger than the coating thickness h (as in the case of an MLD thin-film coating on a thick glass substrate), $\eta \approx 0$ and $\gamma(\alpha, \beta, 0)$ can be drawn from the tabulated numerical data of Suo and Hutchinson[34] to calculate ψ. Small p_c is considered a good assumption when $p_c \ll p_0$, where p_0 is given by[32]

$$p_0 = \frac{16E}{3(1-\nu^2)}\left(\frac{h}{R}\right)^4. \tag{10}$$

For the 40-μm-diam blister considered here, $p_0 = 7.4$ GPa, and the assumption is quite reasonable for a blister pressure of a few megapascals. To determine the corrected mode mixity $\overline{\psi}$, one must know the relevant length scale at which fracture occurs. To analyze the effect of fracture length scale, we write $\psi_B = \psi_A + \varepsilon \ln(\ell_B/\ell_A)$, where the mode mixity ψ_A is associated with fracture at the length scale ℓ_A, and ψ_B with fracture at the length scale ℓ_B. Notice that, since the bimaterial parameter ε is small, this effect will be rather small.

We assume that the mode mixity ψ_A is associated with the length scale ℓ_A comparable to the MLD coating thickness of $h = 5$ μm, and we consider two extreme cases for the effects of the length scale ℓ_B. When fracture processes occur at the length scale ℓ_B comparable to the MLD thickness (i.e., $\ell_B = \ell_A$), the correction term $\varepsilon \ln(\ell_B/\ell_A)$ vanishes, and we use the BK7/MLD mismatch parameters from Table 135.IV to find that $\overline{\psi} = -37.4°$. On the other hand, when fracture processes are at the length scale ℓ_B comparable to the first layer thickness ($t_1 = 131$ nm), we select the BK7/hafnia mismatch parameters because the first layer of the MLD coating adjacent to the BK7 substrate is HfO_2. In this case, $\psi_A = -35.9°$ and $\varepsilon \ln(\ell_B/\ell_A) = -5.8°$, yielding a corrected mode mixity of $\overline{\psi} = -41.7°$. The $\mathcal{G}/\mathcal{G}_0$ curves for these two extreme cases are plotted in Fig. 135.45. Both cases have a broad maximum in the range of $\omega_p = 45°$ to $60°$.

Measurements of the crack propagation angles in the SEM cross-sectional view of a delamination defect are shown in Fig. 135.46(a), and a closer view in Fig. 135.46(b) shows the crack's path through each MLD layer. The crack kinked sharply upward at the first hafnia layer and whenever it reached an interface with a new hafnia/silica layer pair. Within the silica layers (dark bands), the crack curved to a shallower angle, advancing along a trajectory nearly parallel to the layers as it approached the next hafnia layer. The kink angles in the hafnia
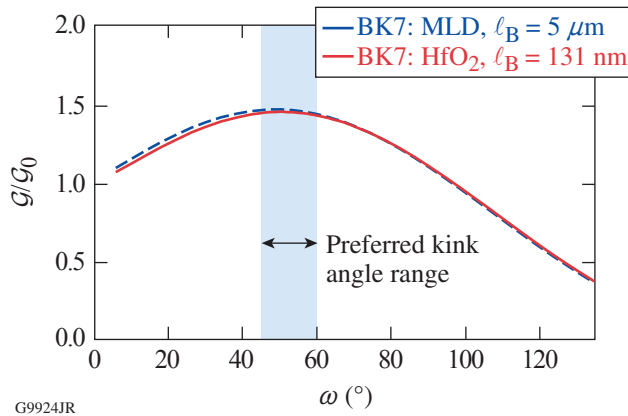
Figure 135.45
Energy-release-rate ratio versus kink angle for two problem length scales: fracture involving the full MLD coating and fracture involving only the first MLD layer. The blue band shows the broad range of energetically preferred kink angles between $\omega = 45°$ and $60°$.

layers (light bands) ranged from $\omega = 52°$ to $66°$: comparable to the preferred angle ω_p calculated in the fracture mechanics analysis, especially considering that measurements could be overestimated if the defect were not perfectly bisected during FIB milling.

Within the multilayer, the jagged crack trajectory can be explained by the relative stiffness of the layers in the MLD coating. When a crack propagating in a stiffer layer approaches an interface with a more-compliant layer, the crack tends to veer toward the interface, shortening its path through the stiff material. When a crack approaches an interface with a stiffer

material, the crack veers away from the interface, assuming an increasingly horizontal trajectory through the compliant layer, as the energy release rate approaches zero near the interface with the stiffer material.[35] Hafnia is significantly stiffer than silica, so the fracture pattern in the defect is consistent with this behavior.

In our fracture mechanics model, we have used the literature on the interfacial or kinking cracks in a single layer bonded to a substrate. Although this analysis gives a fair representation of the kink angle, it does not take into account the full presence of the multilayer in the crack kinking mechanism: the multilayer is viewed as an equivalent single-layer coating with isotropic elastic properties. Of course, the actual multilayer is anisotropic, with different elastic properties parallel to and normal to the interface with the substrate. A full fracture mechanics analysis would include the presence of the individual single layers and, given the pressure in the interfacial crack, determine the traction variation with distance away from the crack tip, and therefore find the mode mixity directly. We are initiating this work.

Conclusion
A mechanism has been proposed for the formation of peroxide-induced delamination defects in multilayer coatings. The mechanism, involving pressure development in a small cavity in the coating, is supported by experimental results and microscopic observation of defects. A fracture mechanics model was developed to explain the deformation and failure of the MLD. The characteristic fracture pattern of the defect
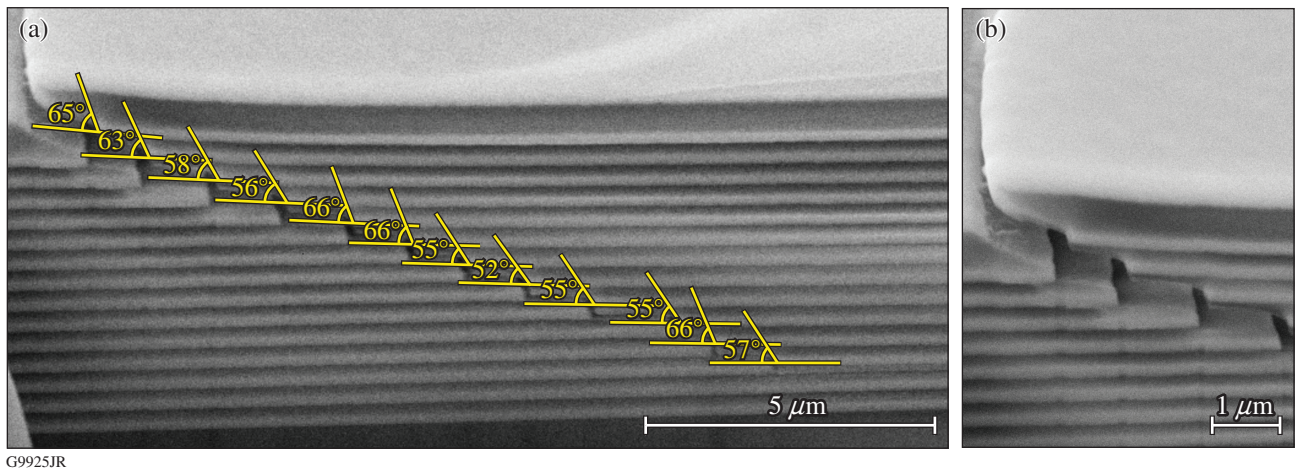
Figure 135.46
(a) Kink angles measured from an observed crack path in a delamination defect; (b) close-up of the defect cross section near the surface, illustrating crack trajectories through the layers of hafnia (light bands) and silica (dark bands).

is found to be consistent with the crack path that maximizes energy release rate.

ACKNOWLEDGMENT

REFERENCES

1. M. Alvisi *et al.*, Thin Solid Films **358**, 250 (2000).

2. X. Cheng *et al.*, Appl. Opt. **50**, C357 (2011).

3. J. Neauport *et al.*, Opt. Express **15**, 12508 (2007).

4. Y. G. Shan *et al.*, Opt. Commun. **284**, 625 (2011).

5. Y. Shan *et al.*, Appl. Opt. **49**, 4290 (2010).

6. J. F. DeFord and M. R. Kozlowski, in *Laser-Induced Damage in Optical Materials: 1992*, edited by H. Bennett *et al.* (SPIE, Bellingham, WA, 1993), Vol. 1848, pp. 455–472.

7. M. D. Feit *et al.*, in *Laser-Induced Damage in Optical Materials: 2000*, edited by G. J. Exarho *et al.* (SPIE, Bellingham, WA, 2001), Vol. 4347, pp. 316–323.

8. W. Kong *et al.*, Microelectron. Eng. **83**, 1426 (2006).

9. H. P. Howard, A. F. Aiello, J. G. Dressler, N. R. Edwards, T. J. Kessler, A. A. Kozlov, I. R. T. Manwaring, K. L. Marshall, J. B. Oliver, S. Papernov, A. L. Rigatti, A. N. Roux, A. W. Schmid, N. P. Slaney, C. C. Smith, B. N. Taylor, and S. D. Jacobs, Appl. Opt. **52**, 1682 (2013).

10. K. L. Marshall, Z. Culakova, B. Ashe, C. Giacofei, A. L. Rigatti, T. J. Kessler, A. W. Schmid, J. B. Oliver, and A. Kozlov, in *Thin-Film Coatings for Optical Applications IV*, edited by M. J. Ellison (SPIE, Bellingham, WA, 2007), Vol. 6674, Paper 667407.

11. H. A. Macleod and D. Richmond, Thin Solid Films **37**, 163 (1976).

12. H. K. Pulker, Appl. Opt. **18**, 1969 (1979).

13. H. Howard, J. C. Lambropoulos, and S. Jacobs, in *Optical Fabrication and Testing*, OSA Technical Digest (online) (Optical Society of America, Washington, DC, 2012), Paper OW3D.3.

14. B. Ashe, K. L. Marshall, C. Giacofei, A. L. Rigatti, T. J. Kessler, A. W. Schmid, J. B. Oliver, J. Keck, and A. Kozlov, in *Laser-Induced Damage in Optical Materials: 2006*, edited by G. J. Exarhos *et al.* (SPIE, Bellingham, WA, 2007), Vol. 6403, Paper 64030O.

15. B. Ashe, C. Giacofei, G. Myhre, and A. W. Schmid, in *Laser-Induced Damage in Optical Materials: 2007*, edited by G. J. Exarhos *et al.* (SPIE, Bellingham, WA, 2007), Vol. 6720, Paper 67200N.

16. S. Chen *et al.*, in *5th International Symposium on Advanced Optical Manufacturing and Testing Technologies: Advanced Optical Manufacturing Technologies*, edited by L. Yang *et al.* (SPIE, Bellingham, WA, 2010), Vol. 7655, Paper 765522.

17. H. M. Jensen, Int. J. Fract. **94**, 79 (1998).

18. J. B. Oliver, T. J. Kessler, H. Huang, J. Keck, A. L. Rigatti, A. W. Schmid, A. Kozlov, and T. Z. Kosc, in *Laser-Induced Damage in Optical Materials: 2005*, edited by G. J. Exarhos *et al.* (SPIE, Bellingham, WA, 2005), Vol. 5991, Paper 59911A.

19. K. Mehrotra, H. P. Howard, S. D. Jacobs, and J. C. Lambropoulos, in *Nanocomposites, Nanostructures and Heterostructures of Correlated Oxide Systems*, edited by T. Endo *et al.*, Mat. Res. Soc. Symp. Proc. Vol. 1454 (Cambridge University Press, Cambridge, England, 2012), pp. 215–220.

20. H. Leplan *et al.*, J. Appl. Phys. **78**, 962 (1995).

21. J. B. Oliver, P. Kupinski, A. L. Rigatti, A. W. Schmid, J. C. Lambropoulos, S. Papernov, A. Kozlov, C. Smith, and R. D. Hand, Opt. Express **20**, 16,596 (2012).

22. J. F. Anzellotti, D. J. Smith, R. J. Sczupak, and Z. R. Chrzan, in *Laser-Induced Damage in Optical Materials: 1996*, edited by H. E. Bennett *et al.* (SPIE, Bellingham, WA, 1997), Vol. 2966, pp. 258–264.

23. J. B. Oliver, P. Kupinski, A. L. Rigatti, A. W. Schmid, J. C. Lambropoulos, S. Papernov, A. Kozlov, and R. D. Hand, in *Optical Interference Coatings*, OSA Technical Digest (Optical Society of America, Washington, DC, 2010), Paper WD6.

24. R. Thielsch, A. Gatto, and N. Kaiser, Appl. Opt. **41**, 3211 (2002).

25. R. Thielsch *et al.*, Thin Solid Films **410**, 86 (2002).

26. S. L. Dole, O. Hunter, and C. J. Wooge, J. Am. Ceram. Soc. **60**, 488 (1977).

27. M. J. Bamber *et al.*, Thin Solid Films **398–399**, 299 (2001).

28. Optical Glass Data Sheets, available online at http://www.schott.com/advanced_optics/us/abbe_datasheets/schott_datasheet_all_us.pdf, Schott North America.

29. L.-K. Wu *et al.*, J. Therm. Anal. Calorim. **93**, 115 (2008).

30. M.-Y. He and J. W. Hutchinson, J. Appl. Mech. **56**, 270 (1989).

31. J. Dundurs, J. Appl. Mech. **36**, 650 (1969).

32. J. W. Hutchinson and Z. Suo, in *Advances in Applied Mechanics*, edited by J. W. Hutchinson and T. Y. Wu (Academic Press, Boston, 1992), Vol. 29, pp. 63–191.

33. M.-Y. He and J. W. Hutchinson, Harvard University, Division of Applied Sciences, Cambridge, MA, Report MECH-113A (February 1989).

34. Z. Suo and J. W. Hutchinson, Int. J. Fract. **43**, 1 (1990).

35. M.-Y. He and J. W. Hutchinson, Int. J. Solids Struct. **25**, 1053 (1989).

Publications and Conference Presentations

Publications

K. S. Anderson, R. Betti, P. W. McKenty, T. J. B. Collins, M. Hohenberger, W. Theobald, R. S. Craxton, J. A. Delettrez, M. Lafon, J. A. Marozas, R. Nora, S. Skupsky, and A. Shvydky, "A Polar-Drive Shock-Ignition Design for the National Ignition Facility," Phys. Plasmas **20**, 056312 (2013).

M. Barczys, S.-W. Bahk, M. Spilatro, D. Coppenbarger, E. Hill, T. H. Hinterman, R. W. Kidder, J. Puth, T. Touris, and J. D. Zuegel, "Deployment of a Spatial Light Modulator–Based Beam-Shaping System on the OMEGA EP Laser," in *High Power Lasers for Fusion Research II*, edited by A. A. S. Awwal (SPIE, Bellingham, WA, 2013), Vol. 8602, Paper 86020F.

C. Dorrer, "Analysis of the Chromaticity of Near-Field Binary Beam Shapers," Appl. Opt. **52**, 3368 (2013).

C. Dorrer, "Analysis of Pulse Replicators for High-Bandwidth, High-Dynamic-Range, Single-Shot Optical Characterization," J. Lightwave Technol. **31**, 1374 (2013).

L. Gao, P. M. Nilson, I. V. Igumenschev, G. Fiksel, R. Yan, J. R. Davies, D. Martinez, V. Smalyuk, M. G. Haines, E. G. Blackman, D. H. Froula, R. Betti, and D. D. Meyerhofer, "Observation of Self-Similarity in the Magnetic Fields Generated by the Ablative Nonlinear Rayleigh-Taylor Instability," Phys. Rev. Lett. **110**, 185003 (2013).

V. N. Goncharov, "Cryogenic Deuterium and Deuterium-Tritium Direct–Drive Implosions on Omega," in *Laser-Plasma Interactions and Applications*, edited by P. McKenna, D. Neely, R. Bingham, and D. A. Jaroszynski, Scottish Graduate Series (Springer, Switzerland, 2013), Chap. 7, pp. 135–183.

I. V. Igumenshchev, D. H. Froula, D. H. Edgell, V. N. Goncharov, T. J. Kessler, F. J. Marshall, R. L. McCrory, P. W. McKenty, D. D. Meyerhofer, D. T. Michel, T. C. Sangster, W. Seka, and S. Skupsky, "Laser-Beam Zooming to Mitigate Crossed-Beam Energy Losses in Direct-Drive Implosions," Phys. Rev. Lett. **110**, 145001 (2013).

J. H. Kelly, A. Shvydky, J. A. Marozas, M. J. Guardalben, B. E. Kruschwitz, L. J. Waxer, C. Dorrer, E. Hill, A. V. Okishev, and J.-M. Di Nicola, "Simulations of the Propagation of Multiple-FM Smoothing by Spectral Dispersion on OMEGA EP," in *High Power Lasers for Fusion Research II*, edited by A. A. S. Awwal (SPIE, Bellingham, WA, 2013), Vol. 8602, Paper 86020D.

B. E. Kruschwitz, J. H. Kelly, C. Dorrer, A. V. Okishev, L. J. Waxer, G. Balonek, I. A. Begishev, W. Bittle, A. Consentino, R. Cuffney, E. Hill, J. A. Marozas, M. Moore, R. G. Roides, and J. D. Zuegel, "Commissioning of a Multiple-Frequency Modulation Smoothing by Spectral Dispersion Demonstration System on OMEGA EP," in *High Power Lasers for Fusion Research II*, edited by A. A. S. Awwal (SPIE, Bellingham, WA, 2013), Vol. 8602, Paper 86020E.

J. Li, J. R. Davies, T. Ma, W. B. Mori, C. Ren, A. A. Solodov, W. Theobald, and J. Tonge, "Hot-Electron Generation from Laser–Pre-Plasma Interactions in Cone-Guided Fast Ignition," Phys. Plasmas **20**, 052706 (2013).

D. T. Michel, A. V. Maximov, R. W. Short, J. A. Delettrez, D. Edgell, S. X. Hu, I. V. Igumenshchev, J. F. Myatt, A. A. Solodov, C. Stoeckl, B. Yaakobi, and D. H. Froula, "Measured Hot-Electron Intensity Thresholds Quantified by a Two-Plasmon-Decay Resonant Common-Wave Gain in Various Experimental Configurations," Phys. Plasmas **20**, 055703 (2013).

J. F. Myatt, H. X. Vu, D. F. DuBois, D. A. Russell, J. Zhang, R. W. Short, and A. V. Maximov, "Mitigation of Two-Plasmon Decay in Direct-Drive Inertial Confinement Fusion Through the Manipulation of Ion-Accoustic and Langmuir Wave Damping," Phys. Plasmas **20**, 052705 (2013).

A. V. Okishev, I. A. Begishev, R. Cuffney, S. Papernov, and J. D. Zuegel, "A Highly Energetic, Multiwavelength, Diode-Pumped Nanosecond Laser System with Flexible Pulse-Shaping Capability," in *Solid State Lasers XXII: Technology and*

Devices, edited by W. A. Clarkson, and R. K. Shori (SPIE, Bellingham, WA, 2013), Vol. 8599, Paper 85990Q.

S. Papernov, "Mechanisms of Near-Ultraviolet, Nanosecond-Pulse-Laser Damage in HfO_2/SiO_2−Based Multilayer Coatings," Chin. Opt. Lett. **11**, S10703 (2013).

L. Parlato, R. Arpaia, C. De Lisio, F. Miletto Granozio, G. P. Pepe, P. Perna, V. Pagliarulo, C. Bonavolontà, M. Radovic, Y. Wang, R. Sobolewski, and U. Scotti di Uccio, "Time-Resolved Optical Response of All-Oxide $YBa_2Cu_3O_7/La_{0.7}Sr_{0.3}MnO_3$ Proximitized Bilayers," Phys. Rev. B **87**, 134514 (2013).

J. Qiao, P. A. Jaanimagi, R. Boni, J. Bromage, and E. Hill, "Measuring 8–250 ps Short Pulses Using a High-Speed Streak Camera on Kilojoule, Petawatt-Class Laser System," Rev. Sci. Instrum. **84**, 073104 (2013).

P. B. Radha, F. J. Marshall, J. A. Marozas, A. Shvydky, I. Gabalski, T. R. Boehly, T. J. B. Collins, R. S. Craxton, D. H. Edgell, R. Epstein, J. A. Frenje, D. H. Froula, V. N. Goncharov, M. Hohenberger, R. L. McCrory, P. W. McKenty, D. D. Meyerhofer, R. D. Petrasso, T. C. Sangster, and S. Skupsky, "Polar-Drive Implosions on OMEGA and the National Ignition Facility," Phys. Plasmas **20**, 056306 (2013).

T. C. Sangster, V. N. Goncharov, R. Betti, P. B. Radha, T. R. Boehly, D. T. Casey, T. J. B. Collins, R. S. Craxton, J. A. Delettrez, D. H. Edgell, R. Epstein, C. J. Forrest, J. A. Frenje, D. H. Froula, M. Gatu-Johnson, V. Yu. Glebov, D. R. Harding, M. Hohenberger, S. X. Hu, I. V. Igumenshchev, R. T. Janezic, J. H. Kelly, T. J. Kessler, C. Kingsley, T. Z. Kosc, J. P. Knauer, S. J. Loucks, J. A. Marozas, F. J. Marshall, A. V. Maximov, R. L. McCrory, P. W. McKenty, D. D. Meyerhofer, D. T. Michel, J. F. Myatt, R. D. Petrasso, S. P. Regan, W. Seka, W. T. Shmayda, R. W. Short, A. Shvydky, S. Skupsky, J. M. Soures, C. Stoeckl, W. Theobald, V. Versteeg, B. Yaakobi, and J. D. Zuegel, "Improving Cryogenic Deuterium–Tritium Implosion Performance on OMEGA," Phys. Plasmas **20**, 056317 (2013).

Forthcoming Publications

J. R. Davies, R. Betti, P. M. Nilson, and A. A. Solodov, "Copper K-Shell Emission Cross Sections for Laser-Solid Experiments," to be published in Physics of Plasmas.

D. H. Froula, T. J. Kessler, I. V. Igumenshchev, R. Betti, V. N. Goncharov, H. Huang, S. X. Hu, E. Hill, J. H. Kelly, D. D. Meyerhofer, A. Shvydky, and J. D. Zuegel, "Mitigation of Cross-Beam Energy Transfer: Implications of Two-State Focal Zooming on OMEGA," to be published in Physics of Plasmas.

I. V. Igumenshchev, V. N. Goncharov, W. T. Shmayda, D. R. Harding, T. C. Sangster, and D. D. Meyerhofer, "Effects of Local Defect Growth in Direct-Drive Cryogenic Implosions on OMEGA," to be published in Physics of Plasmas.

Q. Wang, J. U. Wallace, T. Y.-H. Lee, L. Zeng, J. J. Ou, L. J. Rothberg, and S. H. Chen, "Time-of-Flight Measurement of Charge Carrier Mobility Through Vacuum-Sublimed Glassy Films of *s*-Triazine- and Carbazole-Based Bipolar Hybrid and Unipolar Compounds," to be published in Organics Electronics.

J. Zhang, J. F. Myatt, R. W. Short, A. V. Maximov, H. X. Vu, D. F. DuBois, and D. A. Russell, "Multibeam Two-Plasmon Decay from Linear Threshold to Nonlinear Saturation," to be published in Physical Review Letters.

Conference Presentations

D. D. Meyerhofer, "Observation of Self-Similarity in the Magnetic Fields Generated by the Nonlinear Rayleigh–Taylor Instability," Reconnection Workshop, Princeton, NJ, 4 April 2013.

W. T. Shmayda, "Overview of Tritium Activities of the Laboratory for Laser Energetics," Tritium Focus Group Workshop, Germantown, MD, 23–25 April 2013.

The following presentations were made at the Omega Laser Facility Users Group Workshop, Rochester, NY, 24–26 April 2013:

A. T. Agliata, "How to Ensure Successful Diagnostic Qualification at the OMEGA Laser Facility."

E. F. Armstrong, M. Barczys, B. E. Kruschwitz, and S.-W. Bahk, "Wavefront Measurements of High-Power UV Lasers with a Hartmann Sensor."

M. Barczys, S.-W. Bahk, M. Spilatro, D. Coppenbarger, E. Hill, T. H. Hinterman, R. W. Kidder, J. Puth, T. Touris, and J. D. Zuegel, "Deployment of a Spatial Light Modulator-Based Beam-Shaping System on the OMEGA EP Laser."

C. M. Caggiano, "Fabrication and Characterization of Radial and Azimuthal Polarization Converters with Photoaligned Liquid Crystals."

D. Canning, S. Householder, M. Labuzeta, J. Puth, S. F. B. Morse, B. E. Kruschwitz, M. Barczys, E. Hill, J. Kwiatowski, and R. W. Kidder, "OMEGA EP Shot Performance and Facility Enhancement Status."

J. A. Fooks, M. J. Bonino, A. L. Greenwood, J. S. Jaquez, and M. L. Hoppe, Jr., "Assembly Techniques and Challenges of Two-Plasmon–Decay (TPD) Double-Shell Targets."

V. N. Goncharov, "Recent Progress in Omega Cryogenic Implosions."

D. Haberberger, R. Boni, M. Barczys, J. Brown, R. G. Roides, R. Huff, S. Ivancic, M. Bedzyk, R. S. Craxton, F. Ehrne, E. Hill, R. K. Jungquist, J. Magoon, D. Mastrosimone, J. Puth, W. Seka, M. J. Shoup III, W. Theobald, D. Weiner, C. Stoeckl, J. D. Zuegel, and D. H. Froula, "OMEGA EP 4ω Diagnostic: System Description and Recent Results."

E. Hill and J. Puth, "Omega Laser Facility Timing Management."

R. W. Kidder, M. Miller, C. Kingsley, and A. Zeller, "LLE Resources Are Established to Provide Access to Information for External Users."

R. L. McCrory, "Welcoming Remarks: Omega Laser Users' Group 5th Annual Meeting."

S. F. B. Morse, "Omega Laser Facility Update: 2013 Progress on OLUG Recommendations."

P. M. Nilson, R. Jungquist, C. Stoeckl, C. Mileham, P. A. Jaanimagi, I. A. Begishev, W. Theobald, J. R. Davies, J. F. Myatt, A. A. Solodov, J. D. Zuegel, D. H. Froula, R. Betti, D. D. Meyerhofer, K. Hill, M. Bitter, P. Efthmion, and B. Stratton, "High-Resolving-Power, Ultrafast Streaked X-Ray Spectrometer for OMEGA EP."

G. Pien, "Diagnostic Performance on OMEGA."

P. B. Radha, F. J. Marshall, M. Hohenberger, T. R. Boehly, T. J. B. Collins, R. S. Craxton, D. H. Edgell, D. H. Froula, V. N. Goncharov, J. A. Marozas, R. L. McCrory, P. W. McKenty, D. D. Meyerhofer, D. T. Michel, T. C. Sangster, S. Skupsky, J. A. Frenje, and R. D. Petrasso, "Recent Results from Polar-Drive–Implosions on OMEGA and the NIF."

R. Q. Rivlis, R. Boni, and S. Ivancic, "Optical Modeling and Analysis of a High-Throughput and High-Temporal-Resolution Spectrometer."

C. Sorce and M. Labuzeta, "Exploring the Capabilities of the Omega Laser Facility Web Pages."

S. Stagnitto, M. Labuzeta, and C. Sorce, "Qualifying as an External Instrument Specialist/Technician at LLE."

————————

The following presentations were made at the 9th International Laser Operations Workshop, Livermore, CA, 13–16 May 2013:

D. Canning, G. Balonek, A. Consentino, C. Dorrer, E. Hill, S. Householder, B. E. Kruschwitz, S. F. B. Morse, J. Puth, and J. D. Zuegel, "Multi-FM and NIF PAM Operation on OMEGA EP."

S. F. B. Morse, R. E. Bahr, S. J. Loucks, J. Ulreich, B. Rice, M. J. Shoup III, D. W. Jacobs–Perkins, C. Stoeckl, and C. Mileham, "Cryogenic DT System Improvements for Enhanced ICF Platforms."

J. Puth, S. F. B. Morse, D. Canning, S. Stagnitto, S. Householder, M. Labuzeta, M. Barczys, E. Hill, M. Spilatro, D. Haberberger, J. Kwiatkowski, R. W. Kidder, B. E. Kruschwitz, G. Pien, and G. Fiksel, "Omega Laser Facility Status and Performance."

T. C. Sangster, "Migrating Polar Drive from OMEGA to the NIF."

C. Sorce, R. E. Bahr, J. Katz, D. Mastrosimone, M. McCluskey, C. Mileham, A. Sorce, N. Whiting, and D. H. Froula, "The Experimental Support Group's Role at the OMEGA Facility."

L. J. Waxer, J. H. Kelly, B. E. Kruschwitz, C. Dorrer, M. J. Guardalben, A. V. Okishev, and J. D. Zuegel, "Considerations for Successful Operation of the OMEGA EP Multi-FM SSD System."

———————

P. M. Nilson, "High-Resolving Power, Ultrafast Streaked X-Ray Spectrometer for OMEGA EP," NIF Diagnostic Workshop, Livermore, CA, 21 May 2013.

———————

The following presentations were made at Photonics North, Ottawa, Canada, 3–5 June 2013:

C. Chakraborty, J. Serafini, J. Zhang, R. Sobolewski, L. Q. Zhang, Y. Alimi, A. M. Song, I. Iñiguez-de-la-Torre, J. Mateos, and T. González, "Self-Switching Diodes as Optical Photodectors."

J. Serafini, Y. Wang, and R. Sobolewski, "Time Resolved Carrier Dynamics in Si-on-Glass Absorbers for Photovoltaic Cells."

J. Serafini, J. Zhang, Y. Akbas, R. Sobolewski, M. Mikulics, and R. Adam, "Time-Resolved Relaxation Dynamics of Nonequilibrium Carriers in Free-Standing GaAs Films."

———————

The following presentations were made at CLEO 2013, San Jose, CA, 9–14 June 2013:

K. S. Anderson, R. Betti, P. W. McKenty, T. J. B. Collins, M. Hohenberger, W. Theobald, T. R. Boehly, R. S. Craxton, J. A. Delettrez, D. H. Edgell, S. X. Hu, M. Lafon, J. A. Marozas, D. D. Meyerhofer, R. Nora, T. C. Sangster, W. Seka, S. Skupsky, C. Stoeckl, A. Shvydky, B. Yaakobi, X. Ribeyre,

G. Schurtz, A. Casner, L. J. Perkins, M. R. Terry, and D. E. Fratanduono, "Shock-Ignition OMEGA Experiments and Target Design for the NIF."

S.-W. Bahk, J. Bromage, J. D. Zuegel, and R. K. Jungquist, "An Off-Axis, Single-Pass Radial-Group-Delay Compensator Design Using an Offner Triplet for a Broadband OPCPA Laser."

C. Dorrer, "Characterization of Highly Dispersive Components Using Direct Instantaneous Frequency Measurements."

D. Haberberger, S. Ivancic, M. Barczys, R. Boni, and D. H. Froula, "Plasma Refractometry Using Angular Spectral Filters on OMEGA EP."

T. Z. Kosc, A. Owens, A. L. Rigatti, S. D. Jacobs, and J. H. Kelly, "Long-Term Performance of Liquid Crystal Optics on Large Fusion Lasers."

J. Qiao, J. Papa, and A. Kalb, "Design and Analysis of Meter-Size Deformable Gratings for Compressing Kilojoule, Petawatt Laser Pulses."

T. C. Sangster, "Polar-Direct-Drive Ignition on the NIF."

———————

The following presentations were made at the 25th Symposium on Fusion Engineering, San Francisco, CA, 10–14 June 2013:

D. R. Harding, T. B. Jones, W. Weiqiang, and Z. Bei, "Status and Challenges for Mass Producing Inertial Fusion Energy Targets Using an Automated Electromechanical Microfluidic Process."

S.-J. Scott and D. R. Harding, "Accelerated Evaporative Drying of RF Foam for ICF Target Fabrication."

W. T. Shmayda, "Evaluation of Tritium Capture Systems."

———————

T. C. Sangster, "Polar-Drive ICF," NIF Management Advisory Committee, Livermore, CA, 11–12 June 2013.

———————

J. B. Oliver, J. Bromage, C. Smith, D. Sadowski, C. Dorrer, and A. L. Rigatti, "Plasma-Ion–Assisted Coatings for 15-fs Laser Systems," Optical Interference Coatings 2013, Whistler, Canada, 16–21 June 2013.

———————

S. D. Jacobs, T. Jacobs, D. Saulnier, M. M. Mayton, T. DePorter, J. Sydor, and Z. Hobbs, "Reclamation of Rare-Earth Oxides from Spent Optical Polishing Slurries: Expanding the Technology," Rochester Regional Optics/Photonics/Imaging Business Connections Symposium, Rochester, NY, 20 June 2013.

———————

S.-W. Bahk and C. Dorrer, "Wavefront Sensing Improvements Using a Checkerboard Amplitude Mask," Computational Optical Sensing and Imaging, Arlington, VA, 23–27 June 2013.

———————

R. Nora, W. Theobald, K. S. Anderson, M. Hohenberger, M. Lafon, J. A. Delettrez, A. A. Solodov, P. W. McKenty, W. Seka, T. R. Boehly, S. X. Hu, C. Stoeckl, B. Yaakobi, R. Yan, X. Ribeyre, G. Schurtz, A. Casner, and R. Betti, "Shock Ignition: Past, Present, and Future," 4th International Conference on High Energy Density Physics, Saint-Malo, France, 25–28 June 2013.

———————

J. M. Soures, "The Omega Laser Facility Provides Unique High-Energy-Density Science Capabilities to University, National Laboratory, and Industry Researchers," 2013 User Science Exhibition, Washington, DC, 26 June 2013.